UNIVERSIDADE FEDERAL DE MINAS GERAIS
Instituto de Ciências Exatas
Programa de Pós-graduação em Física

Felipe Menescal Pinto de Medeiros

Mapping defects in vanadium-doped WS_2 monolayers by linear and nonlinear optics

Belo Horizonte
2023

Felipe Menescal Pinto de Medeiros

Mapping defects in vanadium-doped WS_2 monolayers by linear and nonlinear optics

Thesis submitted to the Department of Physics of the Institute of Exact Sciences of the Federal University of Minas Gerais in partial fulfillment of the requirements for obtaining the Master′s degree in Physics.

Supervisor: Professor Dr. Leandro Malard Moreira

Co-supervisor: Professor Dr. Bruno Ricardo de Carvalho

Belo Horizonte
2023

Dados Internacionais de Catalogação na Publicação (CIP)

M488m Medeiros, Felipe Menescal Pinto de.
Mapping defects in vanadium-doped WS2 monolayers by linear and nonlinear optics/ Felipe Menescal Pinto de Medeiros. – 2023.
87 f. : il.

Orientador: Leandro Malard Moreira.
Coorientador: Bruno Ricardo de Carvalho.
Dissertação (mestrado) – Universidade Federal de Minas Gerais, Departamento de Física.
Bibliografia: f. 81-87.

1. Óptica Linear. 2.Óptica não-linear. 3. Matéria condensada. I. Título. II. Moreira, Leandro Malard. III.Carvalho, Bruno Ricardo. IV.Universidade Federal de Minas Gerais, Departamento de Física.

CDU – 530.145 (043)

Ficha catalográfica elaborada por Gislene Rodrigues CRB6/MG-3293/ Biblioteca Professor Manoel Lopes de Siqueira da UFMG.

UNIVERSIDADE FEDERAL DE MINAS GERAIS
INSTITUTO DE CIÊNCIAS EXATAS
PROGRAMA DE PÓS-GRADUAÇÃO EM FÍSICA

FOLHA DE APROVAÇÃO

A presente dissertação, intitulada **"Mapping Defects in Vanadium Doped WS_2 Monolayers by Linear and Non-linear Optics"**, de autoria de **FELIPE MENESCAL PINTO DE MEDEIROS**, submetida à Comissão Examinadora, abaixo-assinada, foi aprovada para obtenção do grau de **MESTRE EM FÍSICA** em quinze de dezembro de 2023.

Belo Horizonte, 15 de dezembro de 2023.

Prof. Leandro Malard Moreira
Orientador do aluno
Departamento de Física/UFMG

Prof. Bruno Ricardo de Carvalho
Coorientador do aluno
Departamento de Física Teórica e Experimental /UFRN

Prof. Paulo Sérgio Soares Guimarães
Departamento de Física/UFMG

Profa. Ana Paula Moreira Barboza
Departamento de Física /UFOP

Prof. Matheus Josué de Souza Matos
Departamento de Física/UFOP

Documento assinado eletronicamente por **Bruno Ricardo de Carvalho**, **Usuário Externo**, em 18/12/2023, às 11:34, conforme horário oficial de Brasília, com fundamento no art. 5º do Decreto nº 10.543, de 13 de novembro de 2020.

Documento assinado eletronicamente por **Leandro Malard Moreira**, **Professor do Magistério Superior**, em 18/12/2023, às 11:42, conforme horário oficial de Brasília, com fundamento no art. 5º do Decreto nº 10.543, de 13 de novembro de 2020.

Documento assinado eletronicamente por **Matheus Josué de Souza Matos**, **Usuário Externo**, em 18/12/2023, às 12:00, conforme horário oficial de Brasília, com fundamento no art. 5º do Decreto nº 10.543, de 13 de novembro de 2020.

Documento assinado eletronicamente por **Ana Paula Moreira Barboza**, **Usuário Externo**, em 18/12/2023, às 12:37, conforme horário oficial de Brasília, com fundamento no art. 5º do Decreto nº 10.543, de 13 de novembro de 2020.

Documento assinado eletronicamente por **Paulo Sergio Soares Guimaraes**, **Professor do Magistério Superior**, em 18/12/2023, às 13:17, conforme horário oficial de Brasília, com fundamento no art. 5º do Decreto nº 10.543, de 13 de novembro de 2020.

In memoriam of my paternal grandfather, Aldo. He worked hard for many years since he was young to grant a good life for his children and wife. He died in late 2018 and couldn’t see any of my accomplishments. Wish you were here, grandpa.

Agradecimentos (acknowledgments in portuguese)

Primeiramente, gostaria de reconhecer a importância de todas as agências de fomento para o desenvolvimento deste trabalho na UFMG: Coordenação de Aperfeiçoamento de Pessoal de Nível Superior (CAPES), Conselho Nacional de Desenvolvimento Científico e Tecnológico (CNPq), Institutos Nacionais de Ciência e Tecnologia (INCT) e em especial à Fundação de Amparo à Pesquisa do Estado de Minas Gerais (FAPEMIG). Todo esse apoio me faz ter esperança no desenvolvimento e no crescimento da ciência de ponta no Brasil.

Eu queria que este trabalho fosse impecável. Se esta tese foi algo próximo disso, só foi possível graças à orientação de Leandro Malard (ou Xubaka, Xubakinha para os mais chegados), que me ajudou durante toda a minha estadia na UFMG. Sempre serei grato por seus conselhos sobre a vida, por nossos encontros, e pelas oportunidades que você me deu e, principalmente, por sua paciência para discutir minhas ideias imaturas de Física, sempre me mostrando como enxergar formas diferentes de resolver problemas que pareciam estar fora do meu alcance. Muito obrigado por tudo, Xubaka!

Eu não teria me mudado para Belo Horizonte para estudar se não fosse pelos conselhos do meu orientador de graduação (também meu co-orientador de mestrado), Bruno Ricardo, que me recomendou vir para a UFMG e sempre serei grato por isso. Além de moldar um alto padrão de pesquisa e comunicação científica que jamais esquecerei, suas ideias em experimentos e fenômenos ópticos são asgardianos. Espero um dia ser como meus orientadores.

Sou grato aos professores incríveis que encontrei durante todos os meus anos na academia em Natal e em Belo Horizonte, principalmente Mario Sérgio Mazzoni, Ana Maria de Paula, Marcos Pimenta e Ronald Dickman pelas aulas incríveis de Física.

O pessoal do Laboratório de Nanoespectroscopia (LabNS) foi fundamental na minha jornada nesse grupo, principalmente o Fred, que me ajudou durante toda a minha estadia e mostrou sua infinita paciência para me ensinar e discutir sobre óptica e montagens experimentais. Muito obrigado aos meus irmãos acadêmicos Danilo e Will (e Fred), e aos meus primos acadêmicos Rafael, Vitor, Renan, Paula, Taiguara, Ana Clara, Jane, Lucas, Douglas, Márcia, Thiago, Hudson e Cassiano por me receberem tão calorosamente. Aos meus amigos da UFMG que sempre encontrei em congressos, Raphaela, Maria Clara Godinho, Campolina e Fábio.

Muito obrigado a Ana Paula Gomes Pereira e Yuri Hayashi do LCPNano por

sua boa vontade em treinar a mim e a vários outros alunos nas instalações do LCP-Nano, que certamente foram fundamentais para este trabalho. Agradeço também aos grandes pesquisadores que conheci durante minha curta estadia em Minas Gerais, em especial aos que me ajudaram por meio de medidas e discussões: Ana Paula Barboza (UFOP), Bernardo Neves (UFMG) e Matheus Matos (UFOP).

Também tenho muitas considerações fora da esfera acadêmica. Primeiramente, gostaria de agradecer aos meus pais Sergio e Suyane e ao meu irmão mais novo Bruno, que me apoiaram em minhas escolhas acadêmicas. Ficar longe deles não foi uma tarefa fácil para mim. A todos os meus amigos que me incentivaram, independentemente da distância que nos separava. Agradeço à minha madrinha Niaskara e ao meu padrinho Ricardo, e a toda a minha família que sempre acreditou em mim.

Por fim, porém não menos importante, agradeço minha noiva Maria Eduarda por todo o amor e carinho que me dá, sempre me apoiando apesar de todos os meus defeitos e insensibilidades. A esperança de estar com você me move todos os dias. Você é minha reyna, minha olivina, minha valquíria, minha IC 1101, minha Yggdrasil, minha estrela, meu silêncio perfeito. Eu amo você.

Dedico este trabalho ao meu afilhado, Théo.

Toda essa experiência foi inenarrável. *Incipit vita nova*!

"Que o sol me traduz
Viver da própria luz".
– Luz, Djavan.

Abstract

In this work, we have investigated the electronic and vibrational properties of WS_2 monolayers doped with 0%, 0.4%, and 2.0% concentrations of vanadium (V–WS_2), synthesized via Chemical Vapour Deposition. We used various linear and non-linear optical techniques, including Raman spectroscopy, Photoluminescence (PL), Second Harmonic Generation, and Four Wave Mixing, as well as Scanning Probe Microscopy. Fluorescence images indicate the existence of a one-dimensional defect region extending from the vertices to the centers of the triangular flakes of the V–WS_2 monolayers, indicating that the dopant concentration is non-homogeneous in these samples. Hyperspectral PL and Raman maps of samples with concentrations of 0%, 0.4%, and 2.0% V–WS_2 corroborate the existence of structural non-homogeneity in this same region. The appearance of a new excitonic state around 1.8–1.9 eV is observed in the non-pure samples, attributed to the introduction of vanadium. In addition, for highly doped samples, a negative energy shift of the first-order WS_2 vibrational modes is observed at the bisectors of the flakes, indicating that there is a greater accumulation of dopants in these regions, creating a mechanical stress effect in the crystal lattice. Non-linear optics measurements confirm the presence of two emission regions, one resonant with the WS_2 exciton and the other resonant with the peak attributed to the introduction of vanadium. Electron Force Microscopy measurements in this region show a more metallic behavior when replacing the tungsten atoms with vanadium. Our results establish linear and non-linear spectroscopy techniques as versatile, strong, and non-destructive tools for characterizing 2D samples doped by metal substitution. Our studies could be useful for improving and efficiently controlling these defects, contributing to the synthesis and large-scale applications of these materials in the near future.

Key-words: 2D materials; nonlinear optics; defects; second harmonic generation; four wave mixing; Raman; PL.

Resumo

Neste trabalho investigamos as propriedades eletrônicas e vibracionais de monocamadas de WS_2 dopadas com concentrações de 0%, 0,4% e 2,0% de vanádio (V–WS_2), sintetizadas via Deposição Quimica à Vapor. Utilizamos diversas técnicas ópticas lineares e não-lineares, incluindo espectroscopia Raman, Fotoluminescência (PL), Gerador de Segundo Harmônico e Mistura de Quatro Ondas, e, também, Microscopia de Varredura por Sonda. Imagens de fluorescência indicam a existência de uma região de defeitos unidimensional que se estende dos vértices aos centros dos flocos triangulares das monocamadas de V–WS_2, indicando que a concentração de dopantes é não-homogênea dessas amostras. Mapas hiperespectrais de PL e Raman em amostras com concentrações de 0%, 0,4% e 2,0% V–WS_2 indicam não-homeogenidades estruturais nessa mesma região. É observado o surgimento de um novo estado excitônico em torno de 1,8–1,9 eV nas amostras não puras, atribuído à introdução do vanádio. Além disso, para amostras altamente dopadas, observa-se um desvio negativo de energia dos modos vibracionais de primeira ordem do WS_2 nas bissetrizes dos flocos, indicando que há acúmulo maior de dopantes nessas regiões, criando um efeito de tensão mecânica na rede cristalina. Medidas de ótica não-linear confirmam a presença de duas regiões de emissão, uma ressonante com o éxciton do WS_2 e outra ressonante com o pico atribuído à introdução de vanádio. Medidas de Microscopia de Força Elétrica nessa região mostram um comportamento mais metálico ao substituir os átomos de tungstênio com vanádio. Nossos resultados estabelecem as técnicas de espectroscopia linear e não-linear como uma ferramenta versátil, forte e não-destrutiva para caracterizar as amostras 2D dopadas por substituição metálica. Nossos estudos podem ser úteis para melhorias e eficiência no controle desses defeitos, contribuindo para a síntese e aplicações destes materiais em grandes escalas num futuro próximo.

Palavras-chave: materiais 2D; ótica não-linear; defeitos; geração de segundo harmônico; mistura de quatro ondas; Raman; PL.

Resumé

Dans ce projet, nous avons étudié les propriétés électroniques et vibrationnelles des monocouches de WS_2 dopées avec des concentrations de 0 %, 0,4 % et 2 % de vanadium (V–WS_2), synthétisées par dépôt chimique en phase vapeur. Nous avons utilisé diverses techniques d'optiques linéaires et non linéaires, notamment la spectroscopie Raman, la photoluminescence (PL), le générateur de seconde harmonique et le mélange à quatre ondes, ainsi que la microscope à sonde locale. Les images de fluorescence indiquent l'existence d'une région de défauts unidimensionnelle s'étendant des sommets aux centres des flocons triangulaires des monocouches V–WS_2, ce qui indique que la concentration de dopant n'est pas homogène dans ces échantillons. Les cartes hyperspectrales PL et Raman d'échantillons ayant des concentrations de 0, 0,4 et 2,0 % de V–WS_2 corroborent l'existence d'une non-homogénéité structurelle dans cette même région. L'apparition d'un nouvel état excitonique autour de 1,8–1,9 eV est observée dans les échantillons non purs, attribuée à l'introduction de vanadium. En outre, pour les échantillons fortement dopés, un déplacement négatif de l'énergie des modes vibrationnels WS_2 du premier ordre est observé au niveau des bissectrices des paillettes, indiquant qu'il y a une plus grande accumulation de dopants dans ces régions, créant un effet de contrainte mécanique dans le réseau cristallin. Des mesures d'optique non linéaire confirment la présence de deux régions d'émission, l'une résonnant avec l'exciton WS_2 et l'autre avec le pic attribué à l'introduction de vanadium. Les mesures de microscopie à force électronique dans cette région montrent un comportement plus métallique lorsque les atomes de tungstène sont remplacés par du vanadium. Nos études pourraient être utiles pour améliorer et contrôler efficacement ces défauts causés par la croissance des lignes de défauts, contribuant ainsi à la synthèse et aux applications à grande échelle de ces matériaux dans un avenir proche.

Mots-clés : materiaux 2D; optique non linéaire, défauts, générateur de seconde harmonique; mélange à quatre ondes; Raman; PL.

List of Figures

1.1 Allotropic forms of carbon. Graphene is a two-dimensional (2D) form of carbon. Graphite is three-dimensional (3D), nanotube one-dimensional (1D) and fullerene zero-dimensional (0D). Adapted from [5]. 24

1.2 *Dark Side of The Moon* cover art adapted. 25

2.1 The family tree of 2D materials, which covers a diverse array of substances, including graphene itself and its analogues like hexagonal boron nitride (hBN), and black phosphorus (BP) and its analogues. The III-VI family of semiconductors, and the transition metal dichalcogenides (TMDs). These materials collectively cover a wide spectrum of electronic properties. The four corner diagrams display the cross-sectional structures of these materials. Taken from [11]. 28

2.2 Graphene honeycomb lattice structure. Lattice built from the basis of the carbons A and B. $\vec{a_1}$ and $\vec{a_2}$ are the primitive unit vectors. 29

2.3 Representation of the first Brillouin zone of graphene. $\vec{b_1}$ and $\vec{b_2}$ are the basis vectors of the reciprocal lattice. High symmetry points are labeled. 30

2.4 Graphene band structure. 31

2.5 Periodic Table of elements. The transition metals and chalcogens that can be combined to create TMD in a 2D form are highlighted above. The elements cobalt (Co), rhodium (Rh), iridium (Ir), and nickel (Ni) are partially highlighted because they do not form a layered structure with all chalcogenides [15]. 32

2.6 TMD polytypes. Adapted from [17]. 32

2.7 Computationally calculated band structures for bulk and monolayer (1L) WS_2. The calculated energy gap is 1.94 eV ($\sim$ 639 nm). The transition from indirect to direct gap is clear. Band structured obtained via Local Density Approximation (LDA), but experimental band-gap is $\sim$ 2.41 eV ($\sim$ 514 nm) [26]. Adapted from [27]. 33

2.8 Simple representation of the effects of dopants in Si. 34

2.9 45 elements that can replace M or X atoms in group 6B TMDs (MoS_2, WS_2 *et cetera*). Blue highlighted elements are acceptors (p-type), red are donors (n-type) and green are isoelectronics dopants [29]. 35

2.10 Eigenvalues of the highest occupied (red circles) and the lowest unoccupied (black squares) defect states in function of the cubic root of the calculated formation energies of various substitutional impurities in WS_2. Data adapted from [9]. 37

3.1 Simple schematic of Raman scattering. 40
3.2 Simple schematic of a Raman spectrum. Rayleigh response (at 0 relative energy) is the elastic contribution for the spectrum and always will be stronger than the inelastic response, which requires the use of an appropriate filter depending on the excitation beam. Peaks with energies $\omega_i - \omega_0$ derive from Stokes process, and peaks with energies $\omega_i + \omega_0$ derive from anti-Stokes process. 42
3.3 Raman spectrum of monolayer WS_2 with excitation beam of 633 nm. Peak positions were normalized by silicon peak position at 521.6 cm^{-1}. The corresponding atomic displacements of the Raman modes are shown. Blue circles represent W atoms and yellow circles represent S atoms). . . 45
3.4 Raman spectra of monolayer WS_2 with three different excitation beams. Peak positions and intensities from all spectra were normalized by the silicon peak position at 521.6 cm^{-1}. 45
3.5 Interband absorption and PL phenomena for both direct bandgap (left) and indirect bandgap (right). Red arrows represent the incoming light, and yellow arrows are the light emissions. Green arrow in the right represents an phonon. Blue and red dots are holes (h^+) and electrons (e^-), respectively. 46

4.1 Sum-frequency generation. **(a)** Geometry of the interaction. **(b)** Energy-level description. 51
4.2 Difference-frequency generation. **(a)** Geometry of the interaction. **(b)** Energy-level description. 51
4.3 **(a)** Geometry of Second Harmonic Generation. **(b)** Energy-level diagram describing Second Harmonic Generation. 52
4.4 Possible mixing process that can occur when three input waves interact in a medium characterized by a $\chi^{(3)}$ susceptibility. **(a)** Geometry of the interaction. **(b)** Energy-level description. 53
4.5 Possible mixing process that can occur when three input waves interact in a medium characterized by a $\chi^{(3)}$ susceptibility. **(a)** Geometry of the interaction. **(b)** Energy-level description. 53

5.1 Schematic of the synthesis of monolayer V-doped WS_2. 55

5.2 Atomic resolution HAADF-STEM images for **(a)** pristine and vanadium doped WS_2 monolayers at **(b)** 0.4, **(c)** 2 and **(d)** 8% at V. Scale bars are 2 nm. Adapted from [10]. 56

5.3 Magnetization *versus* field loops at 300 K for **(a)** pristine and vanadium doped WS_2 monolayers at **(b)** 0.4, **(c)** 2 and **(d)** 8 at % V. Adapted from [10]. 56

5.4 **(a)** Olympus BX51 Fluorescence Microscope and **(b)** its detailed scheme. Adapted from `lcpnano.ufmg.br`. 57

5.5 Simplified scheme of a Raman spectrometer. BS: beam splitter; EF: edge filter; DG: diffraction grating; CCD: charge coupled device. 57

5.6 Scheme of the set-up used in all nonlinear experiments. Red lines represents the laser and blue lines the nonlinear signal. The solid rectangles are mirrors, being the darker one a dichroic mirror. Mirrors inside the dashed box are scanning mirrors. 58

5.7 **(a)** Simplified scheme of a SPM. (i) Cantilever, (ii) probe, (iii) laser, and (iv) photodiode. **(b)** Inter-atomic interaction potential (V_{LJ}) plotted as function of the distance r as an approximation for the tip-sample interaction. In this representation, the blue curve signifies a strictly repulsive interaction, contrasting with the red curve that denotes a purely attractive interaction. The black curve intricately combines long-range attractive forces with short-range repulsive forces, known as the Lennard-Jones potential. 59

5.8 Simplified scheme of a LFM measurement. **(a)** Forward and backward scan direction measurements. **(b)** Profiles of the LFM signal in forward and backward scan direction. 61

6.1 Optical and fluorescent images (FI) of **(a,b)** pristine WS_2, **(c,d)** 0.4, **(e,f)** 2.0, and **(g,h)** 8.0% at V–WS_2 flakes. Scale bars are 50 µm. 62

6.2 Power-dependent PL spectra of pristine, 0.4, and 2.0% at V–WS_2. Powers are in top right of each graph in µW. 63

6.3 PL spectra of pristine, 0.4, and 2.0% at V–WS_2 acquired with $\sim$ 150 µW. . 63

6.4 Hyperspectral PL map. **(a)** Intensity and **(b)** energy maps with 532 nm excitation beam of pristine WS_2 sample. **(c)** Optical image of the region. Scale bar is 10 µm. Map dimensions are 20 µm × 20 µm. 64

6.5 Peak 1 **(a)** intensity and **(b)** energy maps with 532 nm excitation beam of 0.4% at V–WS_2 sample. **(c)** Optical image of the region. Scale bar is 10 µm. Map dimensions are 20 µm × 20 µm. 64

6.6 Peak 2 **(a)** intensity and **(b)** energy maps with 532 nm excitation beam of 0.4% at V–WS_2 sample. **(c)** Optical image of the region. Scale bar is 10 µm. Map dimensions are 20 µm × 20 µm. 64
6.7 Peak 1 **(a)** intensity and **(b)** energy maps with 532 nm excitation beam of 2.0% at V–WS_2 sample. **(c)** Optical image of the region. Scale bar is 10 µm. Map dimensions are 20 µm × 20 µm. 65
6.8 Peak 2 **(a)** intensity and **(b)** energy maps with 532 nm excitation beam of 2.0% at V–WS_2 sample. **(c)** Optical image of the region. Scale bar is 10 µm. Map dimensions are 20 µm × 20 µm. 65
6.9 Raman spectra acquired with 532 nm excitation beam for pristine, 0.4%, and 2.0% at V–WS_2. Peak position and intensities from all spectra were normalized by Silicon peak position and intensity at 521.6 cm^{-1}. 66
6.10 E_{2g} mode **(a)** intensity and **(b)** energy maps with 457 nm excitation beam of pristine WS_2 sample. **(c)** Optical image of the region. Scale bar is 10 µm. Map dimensions are 20 µm × 20 µm. 67
6.11 A_{1g} mode **(a)** intensity and **(b)** energy maps with 457 nm excitation beam of pristine WS_2 sample. **(c)** Optical image of the region. Scale bar is 10 µm. Map dimensions are 20 µm × 20 µm. 67
6.12 E_{2g} mode **(a)** intensity and **(b)** energy maps with 457 nm excitation beam of 0.4% at V–WS_2 sample. **(c)** Optical image of the region. Scale bar is 10 µm. Map dimensions are 20 µm × 20 µm. 67
6.13 A_{1g} mode **(a)** intensity and **(b)** energy maps with 457 nm excitation beam of 0.4% at V–WS_2 sample. **(c)** Optical image of the region. Scale bar is 10 µm. Map dimensions are 20 µm × 20 µm. 68
6.14 E_{2g} mode **(a)** intensity and **(b)** energy maps with 457 nm excitation beam of 2.0% at V–WS_2 sample. **(c)** Optical image of the region. Scale bar is 10 µm. Map dimensions are 20 µm × 20 µm. 68
6.15 A_{1g} mode **(a)** intensity and **(b)** energy maps with 457 nm excitation beam of 2.0% at V–WS_2 sample. **(c)** Optical image of the region. Scale bar is 10 µm. Map dimensions are 20 µm × 20 µm. 68
6.16 Simple representation of the changes generated by the exchange of the metal atom. **(a)** S–W–S bonding. **(b)** S–V–S bonding without bond-length contraction. **(c)** S–V–S bonding with bond-length contraction. . . 69
6.17 SHG images of **(a)** pristine, **(b)** 0.4, **(c)** 2.0, and **(d)** 8.0% at V–WS_2 at 405 nm. Scale bars are 50 µm. 69
6.18 SHG images of 2.0% at V–WS_2 at **(a)** 405 and **(b)** 395 nm. Both images were acquired using the same 405/10 nm filter. **(c)** Profile of the SHG signal for 405 nm at the dashed line. Scale bars are 50 µm. 70

6.19 FWM images at 626 nm for **(a)** pristine, **(b)** 0.4, **(c)** 2.0, and **(d)** 8.0% at V–WS_2 and at 680 nm for **(e)** pristine, **(f)** 0.4, **(g)** 2.0, and **(h)** 8.0% at V–WS_2. The pump, FWM signals, and filters used to acquire these images follow the same order as presented in Table (5.1). Scale bars are 50 µm. . 71

6.20 FWM images at various wavelengths of pristine WS_2. FWM signals are **(a)** 610, **(b)** 620, **(c)** 626, **(d)** 632, **(e)** 650, **(f)** 667, **(g)** 670, and **(h)** 680 nm. The pump, FWM signals, and filters used to acquire these images follow the same order as presented in Table (5.1). ∼70 mW were used for pump and 1064 nm lasers. Scale bars are 50 µm. 72

6.21 FWM images at various wavelengths of 0.4% at V–WS_2. FWM signals are **(a)** 610, **(b)** 620, **(c)** 626, **(d)** 632, **(e)** 650, **(f)** 667, **(g)** 670, and **(h)** 680 nm. The pump, FWM signals, and filters used to acquire these images follow the same order as presented in Table (5.1). ∼70 mW were used for pump and 1064 nm lasers. Scale bars are 50 µm. 72

6.22 FWM images at various wavelengths of 2.0% at V–WS_2. FWM signals are **(a)** 610, **(b)** 620, **(c)** 626, **(d)** 632, **(e)** 650, **(f)** 667, **(g)** 670, and **(h)** 680 nm. The pump, FWM signals, and filters used to acquire these images follow the same order as presented in Table (5.1). ∼70 mW were used for pump and 1064 nm lasers. Scale bars are 50 µm. 73

6.23 **(a,d)** Pristine and 2.0% at V–WS_2 flakes, respectively. **(b,e)** FWM intensity profile in function of FWM signal for pristine and 2.0% at V–WS_2, respectively. **(c,f)** FWM signal profile (dashed lines in **(a)** and **(d)**, respectively. 60 mW were used for pump and 1064 nm lasers. Scale bars are 50 µm. 74

6.24 **(a)** AFM, **(b)** EFM, and **(c)** LFM measurements of pristine WS_2. Scale bars are 5 µm. 75

6.25 **(a)** AFM, **(b)** EFM, and **(c)** LFM measurements of 2.0% at V–WS_2. Scale bars are 5 µm. 75

6.26 Optical and fluorescent images of various defective vanadium-doped WS_2 flakes. Scale bars are 50 µm. 76

6.27 SHG images of **(a,b)** pristine and **(c,d)** 0.4% at V–WS_2. **(a)** and **(c)** is a SHG signal at 405 nm excitation beam using a 405/10 nm band-pass filter. **(b)** and **(d)** are signals at 790 nm excitation beam with the same filter. Scale bars are 50 µm. 76

6.28 FWM images at various wavelengths of pristine WS_2.FWM signals are **(a)** 610, **(b)** 620, **(c)** 626, **(d)** 632, **(e)** 650, **(f)** 667, **(g)** 670, and **(h)** 680 nm. The pump, FWM signals, and filters used to acquire these images follow the same order as presented in Table (5.1). Scale bars are 50 µm. 77

6.29 FWM images at various wavelengths of 0.4% at V–WS_2. FWM signals are **(a)** 610, **(b)** 620, **(c)** 626, **(d)** 632, **(e)** 650, **(f)** 667, **(g)** 670, and **(h)** 680 nm. The pump, FWM signals, and filters used to acquire these images follow the same order as presented in Table (5.1). Scale bars are 50 µm. . 77

6.30 **(a)** SHG at 405 nm and **(b-d)** FWM images of 2% at V–WS_2. The FWM signals are **(b)** 610 nm, **(c)** 650 nm, and **(d)** 680 nm, in which we use a specific filter for each beam as reported in Table (5.1). Scale bars are 50 µm. 78

6.31 FWM images at **(a)** 610, **(b)** 626, **(c)** 650, and **(d)** 680 nm, in which we use a specific filter for each beam as reported in Table (5.1). Scale bars are 50 µm. 78

List of Tables

5.1 Tunable pump wavelengths to generate certain FWM signal with fixed 1064 nm laser along the filters used for every excitation beam. All values are in nanometers. A generic filter n/m nm means its band-pass range is $(n \pm m/2)$ nm. The correspondent photon energy of each FWM signal are displayed. 59

List of Abbreviations

UFMG	Universidade Federal de Minas Gerais
UFRN	Universidade Federal do Rio Grande do Norte
UFOP	Universidade Federal de Ouro Preto
ICEX	Instituto de Ciências Exatas
CAPES	Coordenação de Aperfeiçoamento de Pessoal de Nível Superior
PSU	Pennsylvania State University
FAPEMIG	Fundação de Amparo à Pesquisa do Estado de Minas Gerais
TMD	Transition metal dichalcogenides
FBZ	First Brillouin zone
BS	Band structure
VB	Valence band
CB	Conduction band
CVD	Chemical vapour deposition
PL	Photoluminescence
NLO	Nonlinear optics
SHG	Second Harmonic Generation
FWM	Four Wave Mixing
CARS	Coherent anti-Stokes Raman Spectroscopy
OPO	Optical Parametric Oscillator
PMT	Photomultiplier tube

CCD	Charge-coupled device
SPM	Scanning Probe Microscopy
AFM	Atomic Force Microscopy
EFM	Electrostatic Force Microscopy
LFM	Lateral Force Microscopy
TERS	Tip Enhanced Raman Spectroscopy

Contents

1 Introduction **23**
  1.1 Exploring other dimensions 23
  1.2 Optics as a study engine 25
  1.3 Background, motivations, and objectives 26
  1.4 Outline of the thesis 27

2 2D materials family **28**
  2.1 Two-dimensional materials family tree 28
  2.2 Transition metal dichalcogenides 31
  2.3 Doping concepts applied to TMDs 34
  2.4 Synthesis of 2D materials 35
  2.5 CVD-grown WS_2 36

3 Linear optical phenomena **39**
  3.1 Raman scattering 39
  3.2 Raman active modes in WS_2 44
  3.3 Photoluminescence 46

4 Nonlinear optical phenomena **48**
  4.1 Sum and Difference Frequency Generations 50
  4.2 Second Harmonic Generation 51
  4.3 Four Wave Mixing 52
  4.4 Applications of nonlinear optical techniques 54

5 Experimental methods **55**
  5.1 Sample preparation 55
  5.2 Fluorescence images 56
  5.3 Raman and Photoluminescence measurements 57
  5.4 Nonlinear optical measurements 58
  5.5 Scanning Probe Microscopy 59

6 Experimental results and discussions **62**
  6.1 Photoluminescence spectra 63

6.2 Raman spectra 66
6.3 Nonlinear optical characterization 69
6.4 Scanning Probe Microscopy measurements 75
6.5 Exploring more defects 76

7 Conclusion and further prospects **79**

Bibliography **81**

Chapter 1

Introduction

Studying the properties of materials is key in developing new technologies, which may serve various purposes. Even though several techniques are available, being able to choose appropriate tools to extract important physical information might be game-changing. We want to understand how 2D semiconductors – an important class of materials – can have its physical properties reveled through both nonlinear and linear optical techniques.

1.1 Exploring other dimensions

The universe is a three-dimensional space, and everything in it has length, width, and height as its basic characteristics. But what if our universe was two-dimensional? In this case, every object would be squeezed down to occupy a single plane of existence. How would that world look and behave? Certainly, it would be a very different and unfamiliar place, with unique physical laws and limitations that would profoundly affect our daily lives.

But what if our devices were squashed into the two-dimensional plane? What would we find if we squashed a tip of a pencil into a thin sheet? These questions did not just spark curiosity about the possibilities of new properties of materials, but motivated a series of studies, both theoretical and experimental, on this entirely "new" class of materials.

Before graphene was graphene, "2D graphite" was theoretically studied for almost sixty years [1]. In the 30's, Landau and Peierls affirmed two-dimensional crystals could not exist due to thermodynamic instability [2]. The name "graphene" was firstly used by Boehm and his group in 1986 [3].

Free-standing graphene was first isolated in 2004 by Prof. Andre Geim and Prof. Kostya Novoselov making use of a mere Scotch Tape by carefully exfoliating layers of graphene out of graphite bulks. Doubtlessly the graphene first obtained in the early two thousands was a major mark in Science, Physics, and mainly in Condensed Matter Physics, establishing a whole new set of paradigms in this field [4].

The means for understanding graphene properties requires knowledge of its structure. Graphene is a one-atom-thick sheet made of infinite carbon atoms with sp^2 hybridization, resulting in a hexagonal, honeycomb-like “grid”.

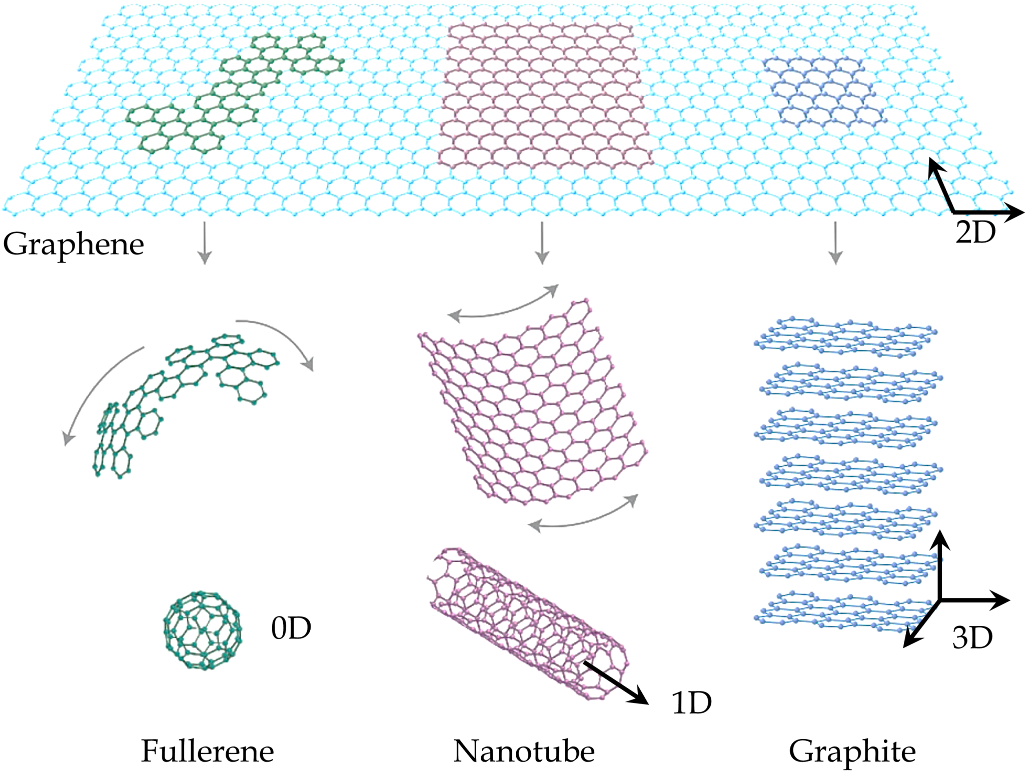

Figure 1.1: Allotropic forms of carbon. Graphene is a two-dimensional (2D) form of carbon. Graphite is three-dimensional (3D), nanotube one-dimensional (1D) and fullerene zero-dimensional (0D). Adapted from [5].

Figure (1.1) shows allotropic forms of carbon. We can stack layers of graphene at a certain point and still preserve the electron’s high mobility, beyond this point we will have its “bulk” form, graphite, which is 3D. For the sake of completeness, a 2D material is *not* two-dimensional in the mathematical sense, since it still has height.

Thus, a 2D material can be expanded in *two* dimensions without changing its primal properties. Otherwise, graphite can be expanded in *three* dimensions without changing its overall settings. Out of our main scope, *one* and *zero* dimensional materials follow the same logic as shown for nanotubes and fullerenes, respectively.

In addition to be the first synthesized 2D material, graphene has a set of “super” proprieties such high tensile strength (1 TPa), very low resistivity in comparison with pure metals and metallic alloys ($10^{-6}\ \Omega \cdot \mathrm{cm}$), low-thickness (0.34 nm, one atom thick), high transmittance (near to 97.7%) and yet high absorbance (2.3% per layer), high heat conductivity ($5300\ \mathrm{W} \cdot \mathrm{m}^{-1} \cdot \mathrm{K}^{-1}$), fastest moving electrons in-plane ($\sim 10^6$ m/s) despite being very elastic, flexible, impermeable, and inert [6, 7].

The emergence of this set of "super" proprieties in graphene is due, in general, to the transition from 3D to 2D, which leads to the confinement of electrons, which can move only in two dimensions rather than three, then the lower screening effect on charge carriers. All these phenomena impact directly the electronic band structure of the material. Graphene, for example, is classified as semi-metal due to the touching of conduction and valence bands in $\mathbf{K}$ and $\mathbf{K}'$ points in the First Brillouin Zone (FBZ), which may explain the rising of some of these new proprieties.

The isolation of graphene in 2004 was only a flash-point to the exploration of different 2D families. The relatively simple technique of isolation of these materials allowed the achievement of layered forms of numerous compounds, breaking the threshold of their usual proprieties to new, interesting sets of physical proprieties, such as electronic and optical, as seen further in this work. In various Transition Metal Dichalcogenide (TMDs), for example, it was reported a transition from indirect to direct band-gap from "bulk" to a two-dimensional form.

1.2 Optics as a study engine

Optics, at first glance, evokes the feeling of resemblance to the *Dark Side of the Moon* from the rock band Pink Floyd. It seems natural to start talks and lectures related to optics with the cover art of this musical masterpiece, not for its elegance, but for its simplicity without being simplistic. In this section, we scratch the surface of fundamental topics, forging basic notions to be further presented in this thesis.

Light-matter interactions are the phenomena that occur when light interacts with matter, such as atoms, molecules, and solid-state materials. Generally speaking, these interactions involve exchanging energy between light and matter, leading to a wide range of physical and chemical effects.

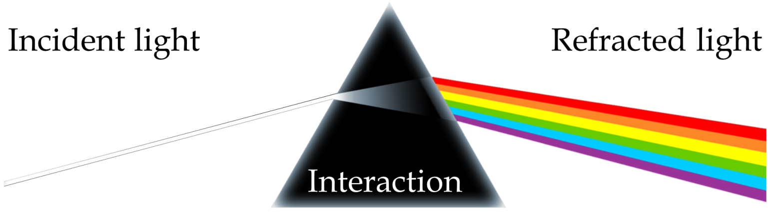

Figure 1.2: *Dark Side of The Moon* cover art adapted.

There are various kinds of light-matter interactions. The nature of the interaction depends on the properties of the given material, whether it is metallic, polymeric, and so on, but it also depends on the characteristics of the incident light, such as its wavelength, polarization, intensity, and coherence.

Light-matter interaction is a fundamental process that underlies a wide range of phenomena, including photosynthesis, eye vision, lasers, and various spectroscopic techniques used to study materials and chemical reactions. Understanding these interactions is essential for developing new devices and technologies based on how light interacts with innovative materials.

1.3 Background, motivations, and objectives

Exfoliating and characterizing graphene was a mark in Solid State Physics. A few years of massive research followed, and new 2D materials started popping into the scene, like hexagonal boron nitride (hBN). Starting around 2010, Transition Metal Dichalcogenides (TMDs) have been exfoliated to mono and few-layered forms [8].

The majority of these TMDs also has been massively studied in the last decade, particularly MoS_2 and WS_2, which are semiconducting and diamagnetic at ambient conditions. However, at certain regimes, these TMDs may present slight (*or not*) changes in these properties, like being ferromagnetic at low temperatures. Doping these materials may also impact their characteristics.

Rosa *et al.* have shown that synthetic WS_2 samples present a 1D defect line along the triangular island bisections, which were proven to be more susceptible to accumulating in these regions via numerical calculations and experimental observations (Second Harmonic Generation, Raman, Scannig Probe Microscopy (SPM), fluorescence) [9]. This is further developed in **Section 2.5**.

Zhang *et al.* fabricated via CVD samples of monolayer WS_2 doped with various concentrations of vanadium, which presented magnetic responses at room temperature, in contrast with its pristine counterparts. Our collaboration with this group allowed us to characterize these samples to investigate how the doping spread throughout the WS_2 flakes and the impacts on the overall properties [10].

In this very work, we will use linear and nonlinear optical techniques to map the spatial distribution of dopants in synthetic WS_2 samples.

1.4 Outline of the thesis

This thesis aims to collate of notions of nanoscience and optics, ranging from basic to advanced concepts, from 2D materials and their proprieties, and how to use light to observe them. In this very chapter, we tried to warm up for what is next, pointing out where we deepen the topics. To better divide these ideas, this thesis has been structured as follows:

Chapter 2 is an overview of the families of two-dimensional materials, in which we briefly explore graphene, and the TMD family which is more focus centered. We want to establish the boundaries of our knowledge on this topic and where we can contribute.
Chapter 3 describes the Raman scattering and Photoluminescence (linear optics) from a theoretical perspective, along with the historical context of the discovery of the Raman phenomenon.
Chapter 4 complements the notions of optical-matter interactions by describing nonlinear optical phenomena such as Second Harmonic Generation (SHG) and Four Wave Mixing (FWM), as we will use these techniques to characterize and identify a great variety of processes in this work.
Chapter 5 describes our experimental setups and sample preparations.
Chapter 6 displays a complete study of vanadium-doped 2D tungsten disulfide, discussing in detail all the results we have obtained so far as we try to understand the range of the impacts of defects in this material.
Chapter 7 concludes this work and outlines a few of its perspectives, pointing to possible roads to follow to fully comprehend the effects of doping 2D TMDs.

Chapter 2

2D materials family

2.1 Two-dimensional materials family tree

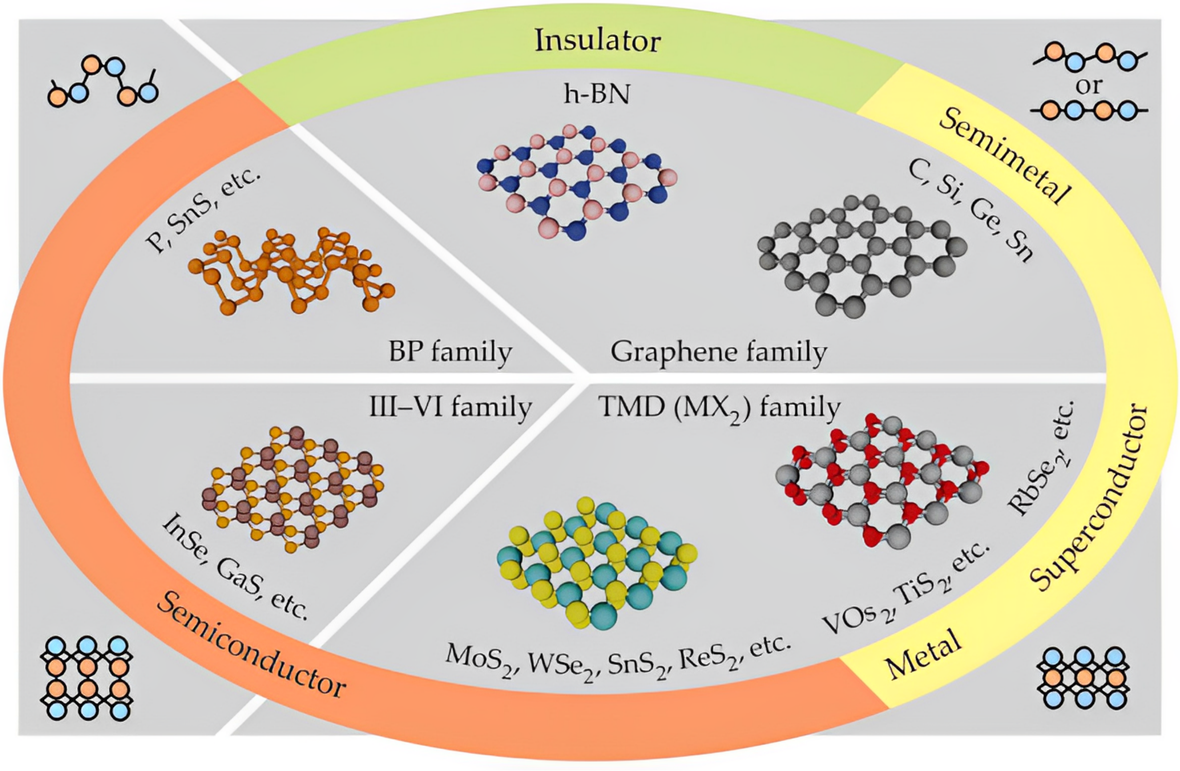

Figure 2.1: The family tree of 2D materials, which covers a diverse array of substances, including graphene itself and its analogues like hexagonal boron nitride (hBN), and black phosphorus (BP) and its analogues. The III-VI family of semiconductors, and the transition metal dichalcogenides (TMDs). These materials collectively cover a wide spectrum of electronic properties. The four corner diagrams display the cross-sectional structures of these materials. Taken from [11].

As discussed briefly in **Chapter 1**, the isolation of a single one-atom thick carbon sheet was a milestone. The obtaining of new 2D materials flowed naturally. The graphene family is formed by hexagonal boron nitride (hBN), which is an insulator, and others one-element one-atom-thick sheet, as graphene itself, and antimonene (Sb), which are semimetals, just to cite a few [12].

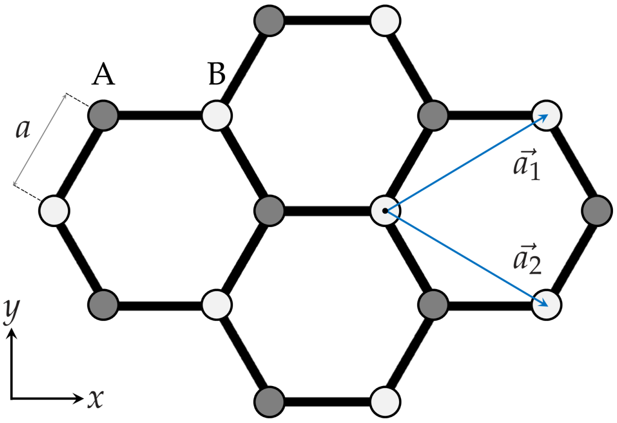

Figure 2.2: Graphene honeycomb lattice structure. Lattice built from the basis of the carbons A and B. $\vec{a}_1$ and $\vec{a}_2$ are the primitive unit vectors.

Monolayer graphene can be represented by an unit cell consisting in two carbon atoms, lets say A and B (for differentiation proposes), shaping a hexagonal grid. To physically write the unit cell, we shall define the primitive vectors of the lattice, as shown in Figure (2.2). Using the distance from two neighbours atoms a as parameter, we may then represent the unit cell. The parameter a equals 1.42 Å for graphene. We can write the primitive vectors as

$$\vec{a}_1 = \frac{3}{2}a\hat{\mathbf{x}} + \frac{\sqrt{3}}{2}a\hat{\mathbf{y}}. \tag{2.1}$$

$$\vec{a}_2 = \frac{3}{2}a\hat{\mathbf{x}} - \frac{\sqrt{3}}{2}a\hat{\mathbf{y}}. \tag{2.2}$$

A priori, unit cells must represent a unit of repetition of any given tree-dimensional structure. Therefore, we must define another primitive vector as

$$\vec{a}_3 = c\hat{\mathbf{z}}. \tag{2.3}$$

We do not want to consider any van der Waals bonding between the layers of graphene. In this case we can take the limit where c goes to infinity.

The unit cell is useful because it allow us to build an infinity crystal only by adding the base (two atoms of carbon) in a sum of integers multipliers of the primitive vectors, which means that the choice of the unit cell is *not* unique. We may also use the primitive vectors to construct the representation of the lattice in reciprocal space. The construction of the vectors in reciprocal space is made by

$$\vec{b}_i = \frac{\vec{a}_j \times \vec{a}_k}{\vec{a}_1 \cdot (\vec{a}_2 \times \vec{a}_3)}. \tag{2.4}$$

Being $\vec{a}_1 \cdot (\vec{a}_2 \times \vec{a}_3)$ the volume of the unit cell. Since $\vec{a}_1, \vec{a}_2 \perp \vec{a}_3$ and c is much greater than other vectors, the vector $\vec{b}_3$ must be null. The unit cell in reciprocal space is the first Brillouin Zone (FBZ), represented in Figure (2.3). The basis vectors in reciprocal space are

$$\vec{b}_1 = \frac{2\pi}{3a}\hat{\mathbf{k}}_\mathbf{x} + \frac{2\pi}{\sqrt{3}a}\hat{\mathbf{k}}_\mathbf{y}. \tag{2.5}$$

$$\vec{b}_2 = \frac{2\pi}{3a}\hat{\mathbf{k}}_\mathbf{x} - \frac{2\pi}{\sqrt{3}a}\hat{\mathbf{k}}_\mathbf{y}. \tag{2.6}$$

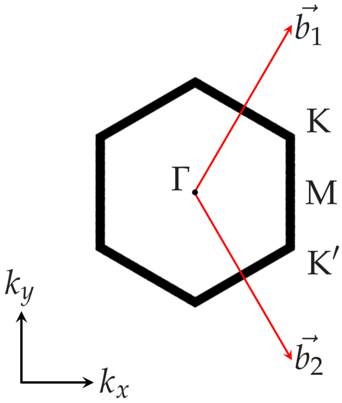

Figure 2.3: Representation of the first Brillouin zone of graphene. $\vec{b}_1$ and $\vec{b}_2$ are the basis vectors of the reciprocal lattice. High symmetry points are labeled.

The first Brillouin zone is hexagonal as shown in Figure (2.3). The FBZ also has four points of high symmetry, which are the points **Γ** at $(0, 0)$, **M** at $(2\pi/3a, 0)$, **K** and **K′** at $(2\pi/3a, \pm 2\pi/3a\sqrt{3})$, which are not equivalent. Note that $\vec{a}_i \cdot \vec{b}_j = 2\pi\delta_{ij}$.

The first calculation of the band structure of graphene was done using the tight-binding method, in which we consider an atom interacting with only the first nearest neighbours [1]. The electronic bands π $(-)$ and π^* $(+)$ of graphene are given by

$$E_\pm(\mathbf{k}) = \pm t\sqrt{3 + 2\cos(\sqrt{3}ak_y) + 4\cos\left(\frac{\sqrt{3}}{2}ak_y\right)\cos\left(\frac{3}{2}ak_x\right)}. \tag{2.7}$$

Being t a hopping term that counts the electron being able to hop to one the three direct neighbours. Take note that the tight-binding model is an approximated model, and analytically solved. The expression of $E_\pm$ allow us to write the band structure of the graphene by plugging into the FBZ.

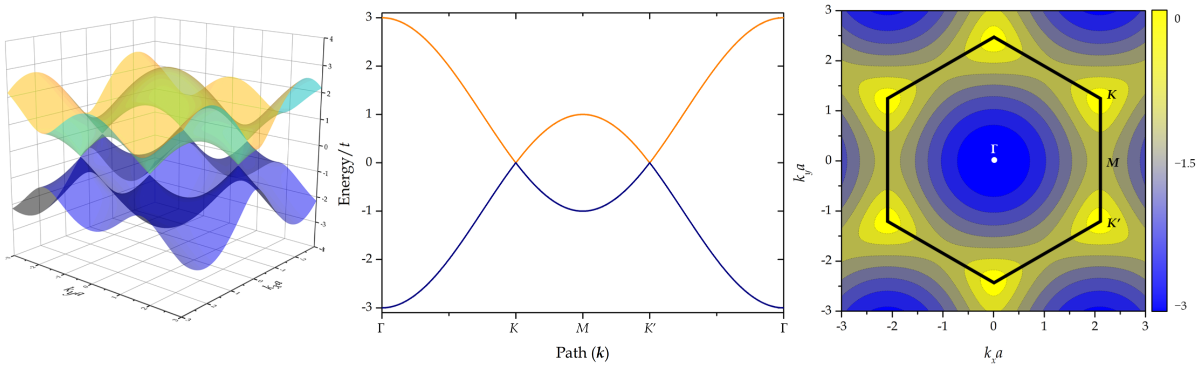

Figure 2.4: Graphene band structure.

It is trivial to see that Equation (2.7) is symmetric in relation to the energy-zero plane. At $E = 0$, positive and negative bands touch at six points ($\mathbf{K}$ and $\mathbf{K}'$), in which the two bands are degenerated, as shown in Figure (2.4) [13]. For pure graphene, carbon atoms are sigma-bonded with other three atoms via sp^2 hybridized orbitals, resulting in out-of-plane p$_z$ orbital, which will form π bonding with other p$_z$ orbitals. Each carbon atom then provides one electron, with spin up or down. In the proximity of these points, we may write their wavevectors as

$$\mathbf{k} = \mathbf{K} + \delta\mathbf{k}. \tag{2.8}$$

For these points, taking the first order Taylor expansion of (2.7) results in

$$E_{\pm}(\delta\mathbf{k}) = \pm\hbar v_{\mathrm{F}}|\delta\mathbf{k}|. \tag{2.9}$$

Being v_{F} the Fermi velocity. These encounters in the $\mathbf{K}$ and $\mathbf{K}'$ points form cones, often named Dirac cones, therefore these high symmetric points are called Dirac points, in which the dispersion is linear, instead of quadratic as usually happens in solids [14].

2.2 Transition metal dichalcogenides

Transition metal dichalcogenides (TMDs, or even TMDCs) are a group of materials composed of an outer transition metal (M) and a chalcogen (X), with a general chemical formula MX$_2$. These materials are layered crystals, in which covalent bonds hold tightly the atoms within the layer but the layers are bonded by a weaker force via van der Waals interaction.

Then the transition metal dichalcogenides can be exfoliated to monolayers, but instead of one atom thickness, TMDs present a trilayer structure formed by two layers of dichalcogenides (X) "sandwiching" one layer of transition metal (M), linked via a strong covalent bonding, forming an X – M – X configuration. The overall proprieties depends mostly on M specie, as briefly shown in Figure (2.1).

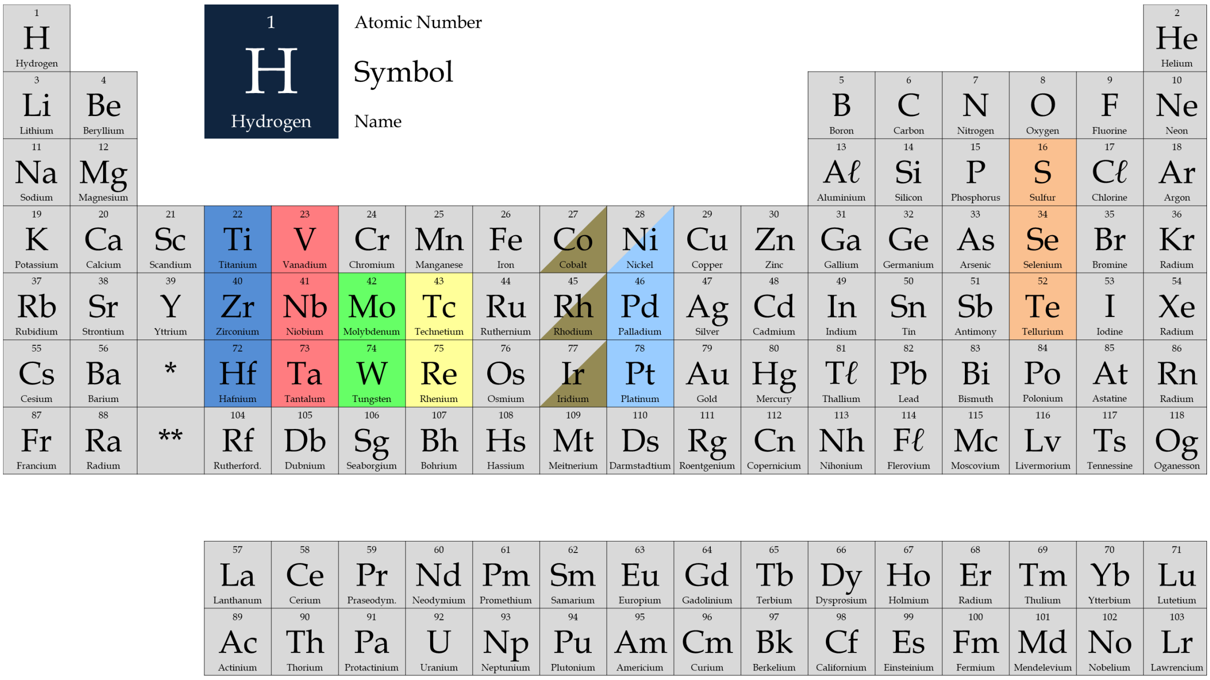

1
H
Hydrogen: Atomic Number, Symbol, Name

1 H Hydrogen																	2 He Helium
3 Li Lithium	4 Be Beryllium											5 B Boron	6 C Carbon	7 N Nitrogen	8 O Oxygen	9 F Fluorine	10 Ne Neon
11 Na Sodium	12 Mg Magnesium											13 Aℓ Aluminium	14 Si Silicon	15 P Phosphorus	16 S Sulfur	17 Cℓ Chlorine	18 Ar Argon
19 K Potassium	20 Ca Calcium	21 Sc Scandium	22 Ti Titanium	23 V Vanadium	24 Cr Chromium	25 Mn Manganese	26 Fe Iron	27 Co Cobalt	28 Ni Nickel	29 Cu Copper	30 Zn Zinc	31 Ga Gallium	32 Ge Germanium	33 As Arsenic	34 Se Selenium	35 Br Bromine	36 Kr Radium
37 Rb Rubidium	38 Sr Strontium	39 Y Yttrium	40 Zr Zirconium	41 Nb Niobium	42 Mo Molybdenum	43 Tc Technetium	44 Ru Ruthernium	45 Rh Rhodium	46 Pd Palladium	47 Ag Silver	48 Cd Cadmium	49 In Indium	50 Sn Tin	51 Sb Antimony	52 Te Tellurium	53 I Iodine	54 Xe Radium
55 Cs Cesium	56 Ba Barium	*	72 Hf Hafnium	73 Ta Tantalum	74 W Tungsten	75 Re Rhenium	76 Os Osmium	77 Ir Iridium	78 Pt Platinum	79 Au Gold	80 Hg Mercury	81 Tℓ Thallium	82 Pb Lead	83 Bi Bismuth	84 Po Polonium	85 At Astatine	86 Rn Radium
87 Fr Francium	88 Ra Radium	**	104 Rf Rutherford.	105 Db Dubnium	106 Sg Seaborgium	107 Bh Bohrium	108 Hs Hassium	109 Mt Meitnerium	110 Ds Darmstadtium	111 Rg Roentgenium	112 Cn Copernicium	113 Nh Nihonium	114 Fℓ Flerovium	115 Mc Moscovium	116 Lv Livermorium	117 Ts Tennessine	118 Og Oganesson
			57 La Lanthanum	58 Ce Cerium	59 Pr Praseodym.	60 Nd Neodymium	61 Pm Promethium	62 Sm Samarium	63 Eu Europium	64 Gd Gadolinium	65 Tb Terbium	66 Dy Dysprosium	67 Ho Holmium	68 Er Radium	69 Tm Thulium	70 Yb Ytterbium	71 Lu Lutetium
			89 Ac Actinium	90 Th Thorium	91 Pa Protactinium	92 U Uranium	93 Np Neptunium	94 Pu Plutonium	95 Am Americium	96 Cm Curium	97 Bk Berkelium	98 Cf Californium	99 Es Einsteinium	100 Fm Fermium	101 Md Mendelevium	102 No Nobelium	103 Lr Lawrencium

Figure 2.5: Periodic Table of elements. The transition metals and chalcogens that can be combined to create TMD in a 2D form are highlighted above. The elements cobalt (Co), rhodium (Rh), iridium (Ir), and nickel (Ni) are partially highlighted because they do not form a layered structure with all chalcogenides [15].

Instead of presenting a hexagonal grid resulting from sp^2 hybridization like group 4 presents (C, Si, Ge, Sn), TMDs energy bands are majorly ruled by the d orbitals in the transition metals, with little contribution from chalcogens p orbitals by hybridization, leading to a strong spin-orbit coupling effect [16].

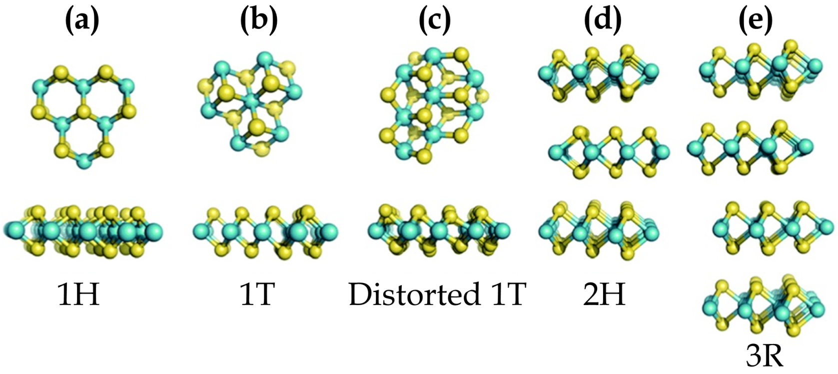

Figure 2.6: TMD polytypes. Adapted from [17].

Even though every TMD follows the same chemical formula, their crystal structure may vary. These possible structure variations are often named polytypes, as shown in Figure (2.6). The most common polytypes are trigonal prismatic (1H), and octahedral (1T) [18]. This notation holds for monolayers only. For bulk TMDs, the trigonal prismatic polytype is noted as 2H. Beyond that, some TMDs may also organized in a distorted 1T polytype, named distorted 1T (or 1T′) [19].

Some 2D materials from the TMD family exhibit structural polymorphism. This means that the same material may exist with different crystal structures. For example, molybdenum ditelluride ($MoTe_2$) can be arranged in trigonal (2H phase), octahedral (1T), and monoclinic (1T′ phase) structures [20, 21]. In this thesis, we are interested in semiconducting group 6B TMDs (MoX_2 and WX_2). Sulfides and selenides are semiconducting ($E_g \sim 1.0$ eV). Tellurides are semimetallic ($\rho \sim 10^{-3}$ Ωcm). These materials are diamagnetic [15]. Other TMD that may be relevant to this work is vanadium disulfide (VS_2), which was reported to be metallic [22, 23].

Analogously to the graphene, we may write the unit cell and proceed to build its reciprocal in k-space (similarly to Figure (2.3), except we need an extra vector in k_z axis for bulk TMDs). In Figure (2.6), we can see monolayers WS_2 do not have an inversion center, in contrast with even-layered WS_2. This is an important note that will be relevant when discussing some nonlinear optical effects further in **Chapter 4**.

Both molybdenum and tungsten disulfides present an indirect energy gap in bulk form. When exfoliating these materials to single-layers we observe not only the change of the energy gap but a transition from indirect to direct (at **K** point) gap as shown in Figure (2.7). Photoluminescence (see **Chapter 3**) spectra of N-layer MoS_2 exhibits an enhancement of a factor $\sim 10^2$ from $N = 2$ to $N = 1$, and $\sim 10^4$ from $N = 6$ to $N = 1$. [24]. Figure (2.7) compares the energy band gaps for bulk, and 1L-WS_2. Indirect gap for bulk is ~ 0.88 eV, and direct gap for 1L is ~ 1.94 eV [25].

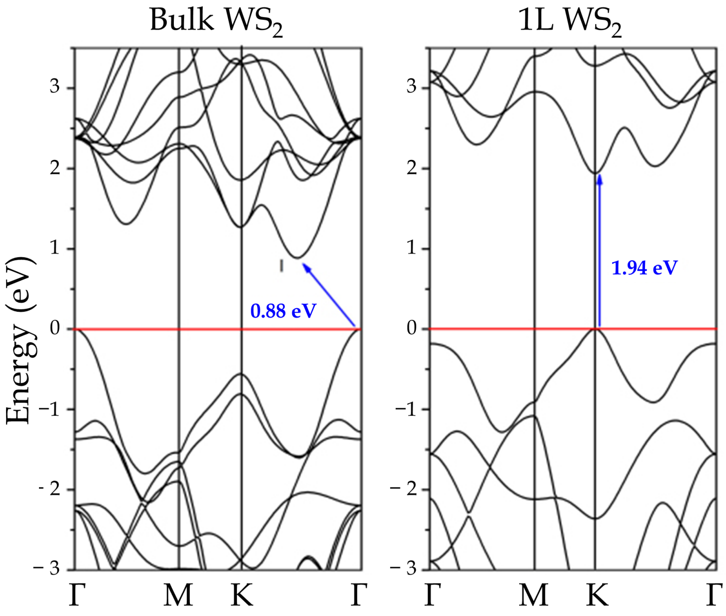

Figure 2.7: Computationally calculated band structures for bulk and monolayer (1L) WS_2. The calculated energy gap is 1.94 eV ($\sim$ 639 nm). The transition from indirect to direct gap is clear. Band structured obtained via Local Density Approximation (LDA), but experimental band-gap is $\sim$ 2.41 eV ($\sim$ 514 nm) [26]. Adapted from [27].

2.3 Doping concepts applied to TMDs

Exposing semiconductors to light will cause the electrons to be excited from the valence band (VB) to the conduction band (CB), creating a density of negative charges in the CB, and the same density of positive charges in the VB. However, this affirmation does not hold up if the semiconductor is not intrinsic [28].

Considering a silicon (Si, family 4A, [Ne]$3s^2 3p^2$) crystal, which is a semiconductor with band-gap of ∼1.1 eV. We plan to replace one single Si atom with a phosphorus (P, family 5A, [Ne]$3s^2 3p^3$) atom. This P atom behaves roughly as a Si atom, except with one more electron, and proton. The valence bands of the Si atoms are completely occupied, which means this extra electron will be in the conduction band.

Instead of replacing a Si atom with a P atom, if we use an aluminium (Aℓ, family 3A, [Ne]$3s^2 3p^1$) atom, we will create an opposite effect, because there will be an electron missing in the conduction band. In case of the P, we name this kind of dopants *n*-dopants or donors, once it donates an electron to the CB. Analogously, we name Aℓ type of dopants *p*-dopants or acceptors, once it creates a positive charge density.

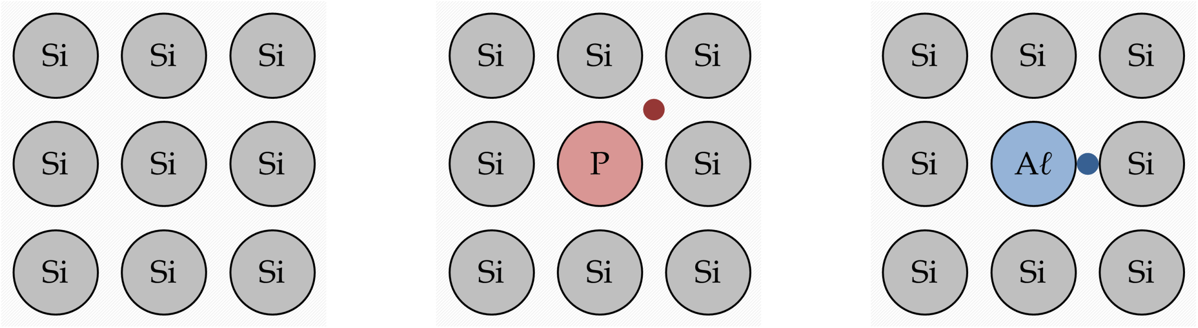

(a) Intrinsic **(b)** *n*-doped **(c)** *p*-doped

Figure 2.8: Simple representation of the effects of dopants in Si.

Regarding the TMDs, doping will cause the enhancement of carriers for bulk crystals (3D). However, in the few-layered regime, the doping effects may differ once the Coulomb screening effect is lower, resulting in weaker doping effects, which means that a higher concentration of dopants is required to achieve more impactful electronic modifications in these materials [29].

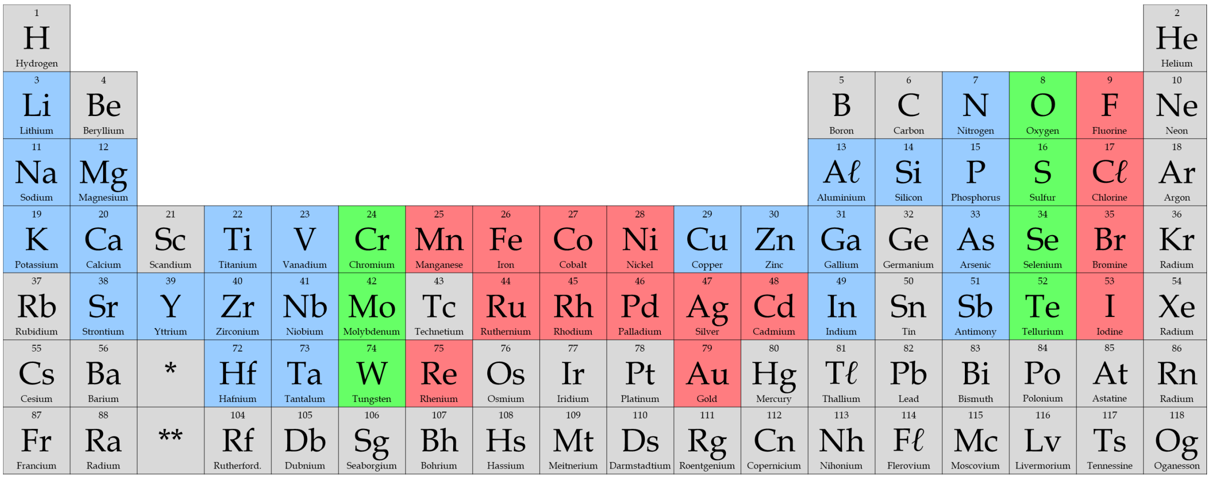

1 H Hydrogen																	2 He Helium
🟦 3 Li Lithium	🟦 4 Be Beryllium											5 B Boron	6 C Carbon	🟦 7 N Nitrogen	🟩 8 O Oxygen	🟥 9 F Fluorine	10 Ne Neon
🟦 11 Na Sodium	🟦 12 Mg Magnesium											🟦 13 Aℓ Aluminium	🟦 14 Si Silicon	🟦 15 P Phosphorus	🟩 16 S Sulfur	🟥 17 Cℓ Chlorine	18 Ar Argon
🟦 19 K Potassium	🟦 20 Ca Calcium	21 Sc Scandium	🟦 22 Ti Titanium	🟦 23 V Vanadium	🟩 24 Cr Chromium	🟥 25 Mn Manganese	🟥 26 Fe Iron	🟥 27 Co Cobalt	🟥 28 Ni Nickel	🟦 29 Cu Copper	🟦 30 Zn Zinc	🟦 31 Ga Gallium	32 Ge Germanium	🟦 33 As Arsenic	🟩 34 Se Selenium	🟥 35 Br Bromine	36 Kr Radium
37 Rb Rubidium	🟦 38 Sr Strontium	🟦 39 Y Yttrium	🟦 40 Zr Zirconium	🟦 41 Nb Niobium	🟩 42 Mo Molybdenum	43 Tc Technetium	🟥 44 Ru Ruthernium	🟥 45 Rh Rhodium	🟥 46 Pd Palladium	🟦 47 Ag Silver	🟥 48 Cd Cadmium	🟦 49 In Indium	50 Sn Tin	🟦 51 Sb Antimony	🟩 52 Te Tellurium	🟥 53 I Iodine	54 Xe Radium
55 Cs Cesium	56 Ba Barium	*	🟦 72 Hf Hafnium	🟦 73 Ta Tantalum	🟩 74 W Tungsten	🟥 75 Re Rhenium	76 Os Osmium	77 Ir Iridium	78 Pt Platinum	🟥 79 Au Gold	80 Hg Mercury	81 Tℓ Thallium	82 Pb Lead	83 Bi Bismuth	84 Po Polonium	85 At Astatine	86 Rn Radium
87 Fr Francium	88 Ra Radium	**	104 Rf Rutherford.	105 Db Dubnium	106 Sg Seaborgium	107 Bh Bohrium	108 Hs Hassium	109 Mt Meitnerium	110 Ds Darmstadtium	111 Rg Roentgenium	112 Cn Copernicium	113 Nh Nihonium	114 Fℓ Flerovium	115 Mc Moscovium	116 Lv Livermorium	117 Ts Tennessine	118 Og Oganesson

Figure 2.9: 45 elements that can replace M or X atoms in group 6B TMDs (MoS_2, WS_2 *et cetera*). Blue highlighted elements are acceptors (p-type), red are donors (n-type) and green are isoelectronics dopants [29].

Figure (2.9) displays which elements may be used as dopants specifically for group 6B TMDs. Note that the elements that constitute the pure TMDs crystals are isoeletronics, while the elements on the left are acceptors, and in the right are donors, due the electronic distribution in the Periodic Table.

Following the periodic properties, elements within the same group are isoelectronics dopants. Elements of the groups on the right are n-type dopants and on the left are p-dopants. 2D group 6B TMDs can be doped by: (i) replacing the chalcogenide; or (ii) replacing the outer transition metal. Method (i) may be achieved after the growth of the samples by bombardment [30]. In contrast, method (ii) must be achieved during the growth introducing precursors which contain the dopant material.

2.4 Synthesis of 2D materials

Mechanical exfoliation (or mechanical cleavage) is the most common process for obtaining 2D materials by simplicity. Using an adhesive tape over a crystal and repeatedly overlapping the tape, the crystal will get thinner and thinner to the point where thin layers are obtained. This is only possible because the bonds between the layers are van der Waals bonds. This technique yield 2D sheets with a high crystalline quality.

Atomic-thick materials have high transmittance, which makes it difficult to differentiate stacking. For this reason, substrates that offer good optical contrast are used. In the case of TMDs, the use of a silicon oxide/silicon (SiO_2/Si) substrate proved to be the best candidate due to the contrast between the phases [14]. We must take extra care after exfoliation. Some TMDs present a high reactivity under normal temperature and pressure conditions. For this reason, we must quickly isolate the material as soon as it is obtained in order to stabilize it and prevent it from oxidizing. The isolation process is done through encapsulation, usually with hexagonal boron nitride (hBN). This process prevents the material from oxidizing. Alternatively, the samples must be kept/stored in vacuum.

Another widely used method for obtaining 2D materials is Chemical Vapor Deposition (CVD). This process has the greatest control over the synthesis parameters, such as the substrate, temperature, and precursors (base materials) [31], and is capable of synthesizing carbon-based inorganic substances [32, 33] and boron nitride nanostructures [34, 35]. In standard CVD procedures, the substrate is exposed to a volatile precursor, reacting with the surface of the substrate. The material of interest is then deposited on the substrate. Depending on the synthesis temperature, it is possible to crystallize TMDs in different phases (polytypes) [36].

In addition to the methods mentioned above, there are other methods for synthesizing two-dimensional materials. It is not our aim to discuss or detail all the known methods, only to consider their advantages and disadvantages. The molecular assembly method is also quite common, although it does not have a good crystalline quality compared to the other methods [37]. The liquid phase exfoliation method is little used compared to the others, but despite its low crystalline quality, it has great synthesis capacity.

Of all the methods, the mechanical cleavage method is the most widely used for fundamental studies, not only because it was used to synthesize the first graphene sheet, but because it produces high-quality crystalline layers when the method is done well. However, the disadvantage of this method lies in the low production due to the care and size of the tape used. On the other hand, the CVD method also has a good quality of the synthesized samples and is able to produce on a much larger scale [38].

2.5 CVD-grown WS_2

Mechanical exfoliation only demands a bulk of the material, a Scotch tape, and patience. Despite resulting in the highest crystal quality over all other methods, it is nearly impractical to rely on mechanical exfoliation for industrial assembly, even for a small production scale. Otherwise, CVD is the perfect candidate for large-scale production of 2D materials in the near future, not only for producing good quality crystals but for the control of the growth parameters.

Particularly, CVD-grown WS_2 flakes grow in triangular shapes. Other shapes may appear due to the choice of the chemical precursors used [39]. This topic will be briefly discussed further in **Chapter 6**. CVD growth can be well controlled by temperature, pressure, and time of exposure [40, 41]. However, even with great control of the process, CVD-fabricated WS_2 samples present spatially localized 1D defect lines across the bisections of the triangular-shaped flakes [9].

Computational calculations show that finite WS_2 triangular-shaped flakes may present non-crystal-like local structures. Rosa *et al.* also took into account the possible W atoms substitution from different regions (edges, corners, and bulk regions). In the end, they demonstrated the removal of W atoms from flake corners requires much less energy than the removal from other regions. In the question of energy, these calculations show that the arising of W vacancies are favorable to occur in the bisections of the triangular-shaped WS_2 flakes [9].

An *et al.* argues the formation of these vacancies defect lines is the result of poor hydrogen gas flow rate. This also leads to the formation of usual triangular-shaped WS_2 flakes, leading to the formation of flakes with tens of micrometers in size. On the other hand, a high H_2 flow rate induces the growth of hexagonal-shaped flakes [42]. Rosa *et al.* assign these defect lines to a higher accumulation of dopants.

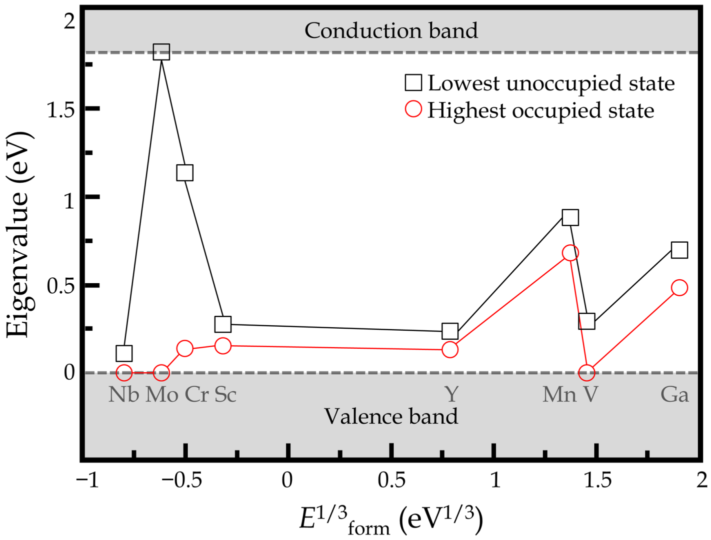

Figure 2.10: Eigenvalues of the highest occupied (red circles) and the lowest unoccupied (black squares) defect states in function of the cubic root of the calculated formation energies of various substitutional impurities in WS_2. Data adapted from [9].

Figure (2.10) shows the calculated eigenvalues of the lowest unoccupied and the highest occupied defect-induced electronic states within the WS_2 band gap as functions of the cubic root of the calculated formation energies ($E^{1/3}_{\text{form}}$) of various substitutional impurities at the W site candidates.

In this diagram, smaller E_{form} implies smaller energetic costs for its occurrence, which is consistent with the smallest calculated E_{form} value in the figure are experimentally observed more often: niobium (Nb), molybdenum (Mo), and chromium (Cr). When the higher or lower occupied electronic state eigenvalues lie within the WS_2 band gap CB or VB indicates the possible action of the defect as an electron and/or hole trap [43].

Figure (2.10) also shows that vanadium (V) exhibits lowest occupied electronic state eigenvalue matching the VB energy value. Despite having a higher E_{form}, it can be easily incorporated into the lattice under favorable conditions. Similarly for other dopants, the addition of V will affect the PL response because it creates unoccupied midgap states [44]. In this work, we try to expand these claims by performing various measurements in intentionally doped WS_2 with vanadium at different concentrations.

Chapter 3

Linear optical phenomena

"I propose this evening to speak to you on a new kind of radiation or light emission from atoms and molecules". Chandrasekhara Venkata Raman introduces his lecture to the South Indian Science Association, at the University of Calcutta, on 16 March 1928, in which he presented his ideas and works about this light interaction phenomenon, lately being named after him.

3.1 Raman scattering

In many of his overseas journeys, Raman, with the use of a simple Nicol prism, noticed variations in the shades of water colour throughout the travel the from India to United Kingdom and vice-versa. He was able to say that the colour of the water was changing with azimuth of observation relatively to the plane of incidence of the sun's rays on the water which makes it possible to observe water in a brilliant, light blue to a deeper, dark blue (almost indigo). The variation of shade and intensity was also affected by the sun's altitude. The matter in this riddle is the azimuth dependence cannot be explained by any absorption theory [45].

Raman scattering is the name given to this light-matter interaction in which the medium responds at different wavelengths with more or less energy than the incident wave. In addition to the honor of having his name associated with this phenomenon, Raman was awarded the Nobel Prize in 1930, just two years after the publication of his work on light. He was the first Asian to win a Nobel Prize in Science.

Figure (3.1) shows an incident wave of frequency ω_0 interacting with a generic molecule, which have normal modes of vibration, and the response will be a unaltered, elastically scattered light, and other responses with frequencies ω' where $\omega' \neq \omega_0$, being greater or smaller then the incident, depending on which normal mode vibration the emission is associated with.

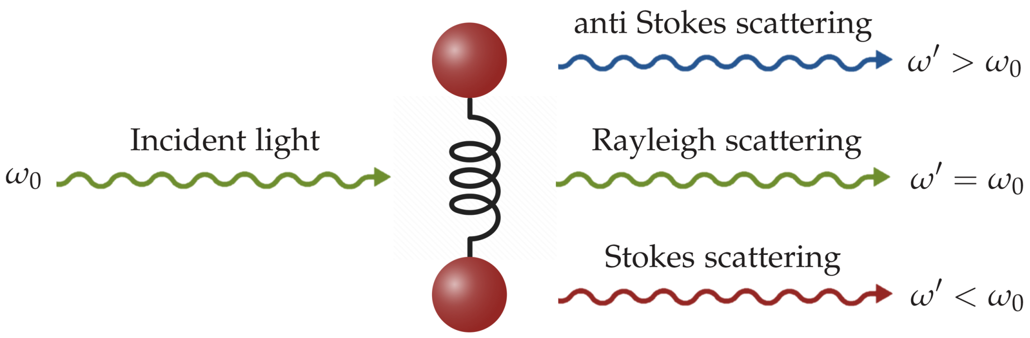

Figure 3.1: Simple schematic of Raman scattering.

Classical Raman process theory succeeds in explaining light-matter interactions, which induce polarization of certain medium. Let us consider an infinite crystal for sake of simplicity so that we do not need to worry about edge problems. *A priori* this crystal is at a finite temperature. The crystal that we are studying has a dielectric susceptibility $\chi^{(1)}$. We will also consider an electromagnetic field radiation of intensity $|\mathbf{E}|$. The polarization of this crystal can be written as [46]

$$\mathbf{P}(\mathbf{x},t) = \varepsilon_0 \chi^{(1)} \cdot \mathbf{E}(\mathbf{x},t). \tag{3.1}$$

$$P_i = \varepsilon_0 \sum_{i,j} \chi^{(1)} E_j. \tag{3.2}$$

In which $\chi^{(1)}$ is a second rank tensor with 9 components,

$$\chi^{(1)} = \begin{pmatrix} xx & xy & xz \\ yx & yy & yz \\ zx & zy & zz \end{pmatrix}. \tag{3.3}$$

We must evaluate the behavior of the interaction between electromagnetic waves in a material medium. Since the electric field is related to a radiation, it can be written as a plane wave of amplitude $\mathbf{E_0}$.

$$\mathbf{E} = \mathbf{E_0} \cos(\omega_0 t). \tag{3.4}$$

Note that the electric field amplitude depends on the wave vector $\mathbf{k}_i$ and frequency of the incident radiation ω_0. The susceptibility tensor depends on the atomic displacement of the medium $\mathbf{Q}(\mathbf{x},t)$. For small atomic vibrations (considering a crystal at room temperature), χ is a linear function of $\mathbf{Q}$, we are able then write the approximate form of the susceptibility with a Taylor series expansion [47].

$$\chi^{(1)} = \chi_0^{(1)} + \left(\frac{\partial \chi^{(1)}}{\partial \mathbf{Q}}\right)_0 \mathbf{Q}(\mathbf{x}, t) + \cdots \tag{3.5}$$

In which the χ_0 term is the portion of the susceptibility that presents no fluctuations. The term that depends on the first derivative at $\mathbf{Q}$ is the portion that represents the fluctuating portion of the susceptibility induced by the displacement vector $\mathbf{Q}$. Since we can do the separation shown in Equation (3.5), we are able to rewrite $\mathbf{P}$ as

$$\mathbf{P}(\mathbf{x}, t) = \mathbf{P}_0(\mathbf{x}, t) + \mathbf{P}_{\text{induced}}(\mathbf{x}, t, \mathbf{Q}). \tag{3.6}$$

Being the term $\mathbf{P_0}$ the polarization vector that oscillates in resonance with the incident radiation, giving rise to elastic (also called Rayleigh) scattering, and $\mathbf{P}_{\text{induced}}$ is induced by atomic vibration. To determine the induced polarizability, we need to consider the normal mode of vibration of $\mathbf{Q}(\mathbf{x}, t)$ in the form of a plane wave [48].

$$\mathbf{Q}(\mathbf{x}, t) = \mathbf{Q}_0(\mathbf{q}, \omega_0) \cos(\mathbf{q} \cdot \mathbf{x} - \omega_0 t). \tag{3.7}$$

The displacement is a periodic cosine function that depends on the medium wave vector $\mathbf{q}$ and the material vibration frequency ω_0. Thus we can call the Equations (3.1), (3.4) and (3.6) and write in the form

$$\mathbf{P}(\mathbf{x}, t, \mathbf{Q}) = \chi_0^{(1)} \mathbf{E_0} \cos(\omega_0 t) + \mathbf{E_0} \mathbf{Q_0} \left(\frac{\partial \chi^{(1)}}{\partial \mathbf{Q}}\right)_0 \cos(\omega_0 t) \cos(\omega_Q t). \tag{3.8}$$

Equation (3.8) can be separated into elements, one belonging to the induced polarizability and other to the polarizability intrinsic to the material. Thus, the induced polarizability depends on the atomic displacement and can be written as

$$\mathbf{P}_{\text{induced}}(\mathbf{x}, t, \mathbf{Q}) = \frac{1}{2} \mathbf{E_0} \mathbf{Q_0} \left(\frac{\partial \chi^{(1)}}{\partial \mathbf{Q}}\right)_0 \left\{\cos([\omega_0 - \omega_q] t) + \cos([\omega_0 + \omega_q] t)\right\}. \tag{3.9}$$

Showing that in this context, when light interacts with matter, incident photons can be scattered (i) elastically or inelastically by (ii) creating or (iii) destroying an atomic vibration, *id est*, a phonon.

Therefore, Equation (3.9) shows that the induced polarization has two components: one with wave vector $\mathbf{k}_{\text{aS}} = \mathbf{k} + \mathbf{q}$ and frequency $\omega_{\text{aS}} = \omega + \omega_0$ and the other part with wave vector $\mathbf{k}_{\text{S}} = \mathbf{k} - \mathbf{q}$ and frequency $\omega_S = \omega - \omega_0$. The wave vector $\mathbf{k}_{\text{aS}}$ and frequency ω_{aS} correspond to anti-Stokes scattering (destroying a phonon), while wave vector $\mathbf{k}_{\text{S}}$ and frequency ω_{S} correspond to Stokes scattering (creating a phonon), both being inelastic scattering between the incident radiation and the medium. The portion of the radiation that interacts elastically with the medium is called Rayleigh scattering (first term in Equation (3.8)).

The Raman spectra show peaks at energies $E_{\text{laser}} - E_{\text{scattering}}$, which corresponds to the phonon energy E_{Ph}. The phonon excitation can be described by a damped harmonic oscillator, in which the damping emerge from the interaction with the medium. The external force ω (excitation beam) is applied to a damped oscillator with natural frequency ω_q (phonon frequency), resulting in a behavior very similar to a classic oscillator damped by a fluid.

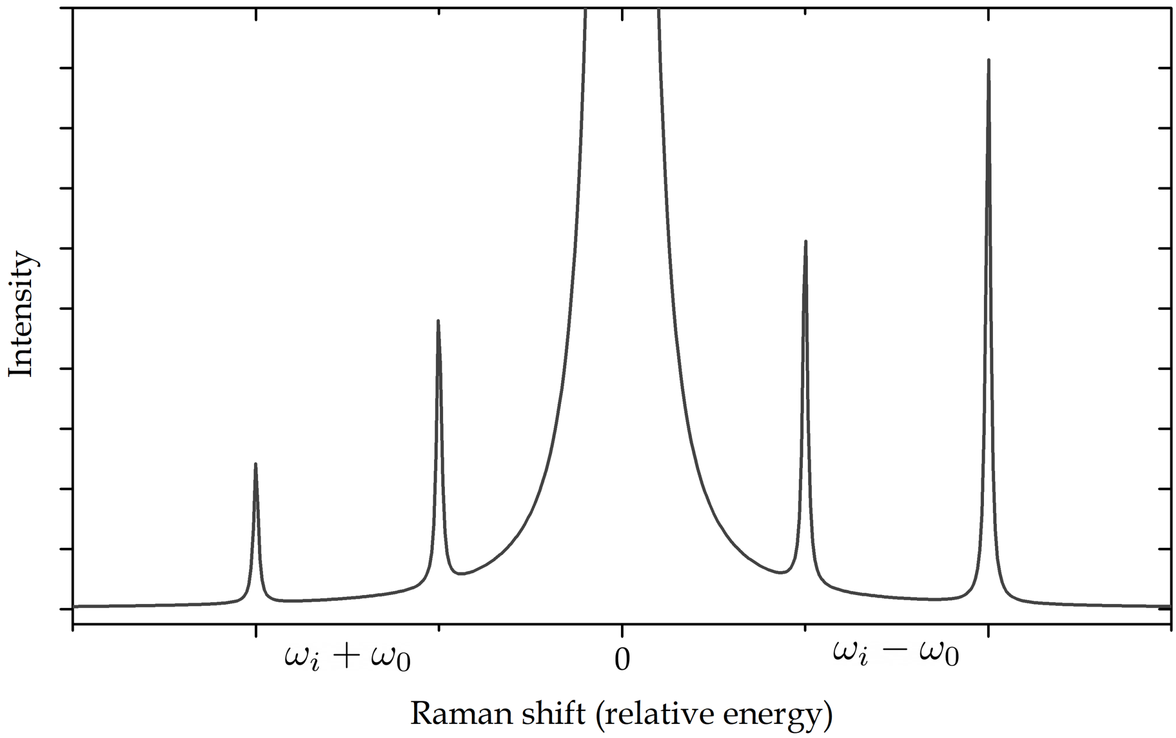

Figure 3.2: Simple schematic of a Raman spectrum. Rayleigh response (at 0 relative energy) is the elastic contribution for the spectrum and always will be stronger than the inelastic response, which requires the use of an appropriate filter depending on the excitation beam. Peaks with energies $\omega_i - \omega_0$ derive from Stokes process, and peaks with energies $\omega_i + \omega_0$ derive from anti-Stokes process.

Thus, the look of a Raman spectrum will be the sum of the response of the damped oscillators with natural frequency ω_q externally forced by the beam ω (as shown in Figure (3.2)). The response of this oscillator will be given by a Lorentzian curve as

$$I(\omega) = \frac{I_0}{\pi\Gamma_q} \frac{1}{(\omega - \omega_q)^2 + \Gamma_q^2}. \tag{3.10}$$

In a particular case where $\omega_q \gg \Gamma_q$. The center of the peak gives the particular frequency of the Raman mode. The width of the peak is related to damping energy of the phonon. Also, the width is related with uncertainty in energy of the phonon. It is, higher energy uncertainty, smaller the uncertainty of the phonon lifespan by the Heisenberg's principle.

The classical formalism starts from the concepts of polarizability, electromagnetic waves and the principle of conservation of momentum, which succeeds in finding an expression capable of explaining the first-order modes, describing induced polarization into two portions that interact inelastically given by distinct wavevectors **k** and **q**.

However, it cannot describe the electron-phonon interaction, which is stronger than the photon-phonon interaction. Therefore, in order to obtain information on electron-phonon interactions, it is convenient to understand Raman scattering within the quantum formalism. With this propose, we consider a Hamiltonian $\mathcal{H}$ of the system based on the perturbation theorem [47].

$$\mathcal{H} = \mathcal{H}_{\mathrm{e}} + \mathcal{H}_{\ell} + \mathcal{H}_{\mathrm{r}} + \mathcal{H}_{\mathrm{eR}} + \mathcal{H}_{\mathrm{eL}}. \tag{3.11}$$

In which $\mathcal{H}_{\mathrm{e}} + \mathcal{H}_{\ell} + \mathcal{H}_{\mathrm{r}}$ corresponds to the unperturbed hamiltonian, representing the electron, lattice vibrations and incoming radiation, respectively. $\mathcal{H}_{\mathrm{eR}} + \mathcal{H}_{\mathrm{eL}}$ corresponds perturbed, representing the electron interacting with incoming radiation and the electron-phonon interaction, respectively.

Raman processes are said to be of the first order when only one phonon is involved. In this case, the process takes place in stages: (i) an incident photon of frequency ω_i, in the initial state $|i\rangle$, interacts with the material creating an electron-hole pair, placing the system in the state $|a\rangle$ (via $\mathcal{H}_{\mathrm{eR}}$); (ii) the electron (and/or hole) is scattered inelastically (via $\mathcal{H}_{\mathrm{eL}}$), emitting a phonon of frequency $\hbar\omega_{\mathrm{Ph}}$, placing the system in the $|b\rangle$ state; (iii) finally, the electron-hole pair recombines, emitting a photon of energy $\hbar\omega_{\mathrm{s}}$, where the system enters the $|f\rangle$ state. The probability of Raman scattering can be described by Fermi's golden rule written as

$$W_{i\to j} = \frac{2\pi}{\hbar} \left|\langle i|\mathcal{H}|j\rangle\right|^2 \delta(E_j - E_i). \tag{3.12}$$

Equation (3.12) describes the probability of an electron in the initial state $|i\rangle$ and energy E_i of absorbing a photon of energy $\hbar\omega$ and going to a final state $|j\rangle$ with energy E_j, thus allowing the intensity of the process to be determined, given by

$$I(\hbar\omega) \propto \sum_{a,b} \left| \frac{\langle f|\mathcal{H}_{\mathrm{eR}}|b\rangle\langle b|\mathcal{H}_{\mathrm{e-Ph}}|a\rangle\langle a|\mathcal{H}_{\mathrm{eR}}|i\rangle}{(\hbar\omega - E_a - i\gamma)(\hbar\omega - \hbar\omega_{\mathrm{Ph}} - E_b - i\gamma)} \right|^2 . \tag{3.13}$$

The terms E_a and E_b correspond to the transition energies of the material and γ is the damping frequency related to the lifetime of the electron-phonon coupling. This is just one of the scattering probabilities taking place; other processes such as the annihilation of a phonon, processes involving the hole and even more than one phonon participating are taking place simultaneously. In the latter case, when you have two phonons participating in the process, the intensity of the second-order Raman process is given by

$$I(\hbar\omega) \propto \sum_{a,b} \left| \frac{\langle f|\mathcal{H}_{\mathrm{eR}}|c\rangle \langle c|\mathcal{H}_{\mathrm{e-Ph}}|b\rangle \langle b|\mathcal{H}_{\mathrm{e-Ph}}|a\rangle \langle a|\mathcal{H}_{\mathrm{eR}}|i\rangle}{(\hbar\omega - E_a - i\gamma)(\hbar\omega - \hbar\omega_{\mathrm{Ph}} - E_b - i\gamma)(\hbar\omega - \hbar\omega_{\mathrm{Ph}'} - \hbar\omega_{\mathrm{Ph}} - E_c - i\gamma)} \right|^2 . \tag{3.14}$$

In which E_i $(i = a, b, c)$ is the transition energy of the material. From the Equation (3.14) it is clear that, unlike the first-order processes in which the phonons existed near the center of the Brillouin zone (point $\mathbf{\Gamma}$), the phonons participating in the second-order process must satisfy the principle of conservation of momentum, since they occur at the edges of the FBZ [49, 50].

It is interesting to note that when the energy of the incident photon coincides with the electronic gap of the material (E_g), the intensities of the Raman bands are "amplified" so that some quantum processes are allowed or easily observed, like the double resonance Raman scattering (DRR) process [47, 51].

It should be noted that this process is not to be confused with the second-order process which is a reflection of the Density of States (DoS), *id est* changing the excitation energy does *not* affect the positions of the peaks in the spectroscopy, in contrast to the DRR process in which it is possible to observe the dispersion (shifting) of the bands with the change in the energies used [52].

3.2 Raman active modes in WS_2

Figure (3.3) exhibits a typical Raman spectrum of 1L–WS_2 excited by 633 nm laser beam (1.96 eV). For this excitation energy, the Raman spectrum is non-resonant, so we see only first order Raman responses. The A_{1g} mode (at $\sim$ 417 cm^{-1}) is the result of the displacement of S atoms out of plane, in which the W atom is not involved in the vibration. The E_{2g} mode (at $\sim$ 356 cm^{-1}) is the result of displacement of S atoms out of phase with the W atoms in plane. The peak at 521 cm^{-1} is related with the Si (substrate) response.

Figure (3.4) shows three Raman spectra of 1L–WS_2 acquired with different laser lines. According to Equation (3.14), the intensity of the Raman modes will enhance when the excitation beam energy matches the energy gap. In comparison with the spectra measured with 633 nm and 568 nm, the spectrum obtained with the 514 nm beam is much richer, where second-order Raman processes take place. In-resonance Raman spectrum is dominated by second-order Raman processes.

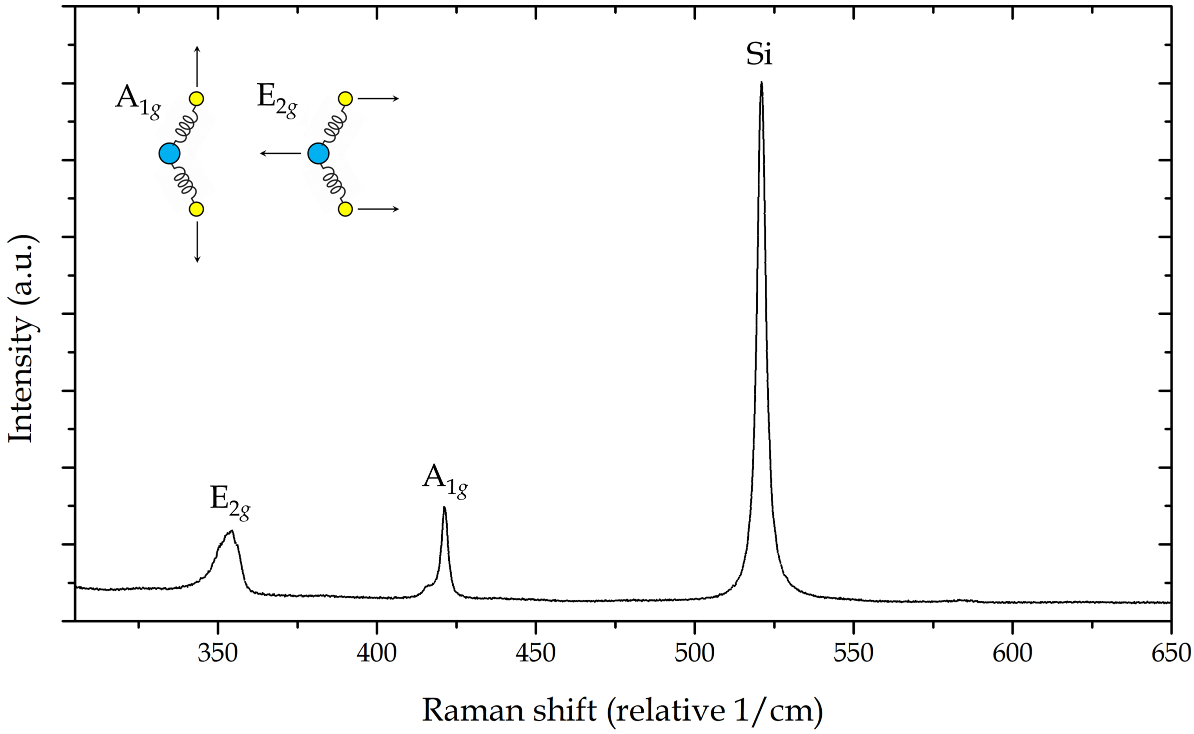

Figure 3.3: Raman spectrum of monolayer WS_2 with excitation beam of 633 nm. Peak positions were normalized by silicon peak position at 521.6 cm^{-1}. The corresponding atomic displacements of the Raman modes are shown. Blue circles represent W atoms and yellow circles represent S atoms).

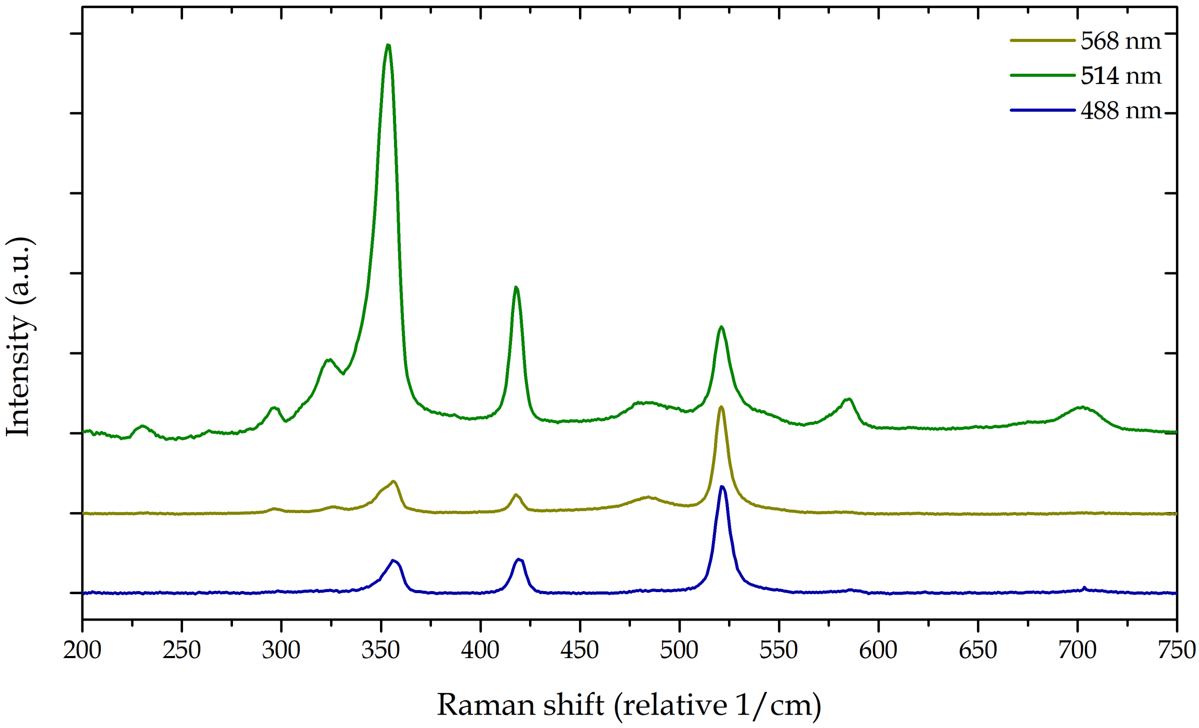

Figure 3.4: Raman spectra of monolayer WS_2 with three different excitation beams. Peak positions and intensities from all spectra were normalized by the silicon peak position at 521.6 cm^{-1}.

3.3 Photoluminescence

Atoms can attain excited states through various means, including the absorption of light, electrical stimulation, heat exposure, chemical reactions, and even friction. In everyone of these scenarios, the media will respond, and emit light, that radiates in all directions. All these phenomena are examples of luminescence. In this work, we are particularly interested in Photoluminescence, in which light excites the material.

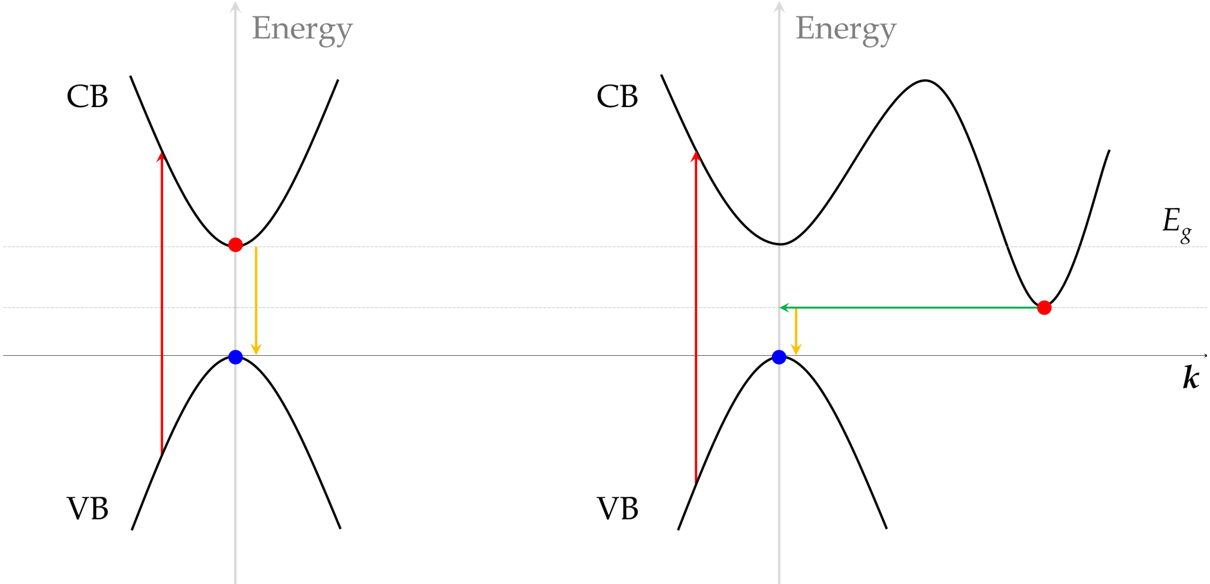

Figure 3.5: Interband absorption and PL phenomena for both direct bandgap (left) and indirect bandgap (right). Red arrows represent the incoming light, and yellow arrows are the light emissions. Green arrow in the right represents an phonon. Blue and red dots are holes (h^+) and electrons (e^-), respectively.

In semiconducting group 6B TMDs, the optical absorption is dominated by interband absorption, it means the electrons are excited from the VB to the CB, leaving holes (h^+) in the VB, creating an electron-hole pair [53]. Recalling that monolayers of these materials have direct bandgaps. From basic principles, momentum and energy are conserved during the absorption process. Hence we can affirm that

$$E_{\text{final}} = E_{\text{initial}} + \hbar\omega_i. \tag{3.15}$$

$$\mathbf{k}_{\text{final}} = \mathbf{k}_{\text{initial}}. \tag{3.16}$$

In which $\hbar\omega_i$ is the energy of the incident photon, and $\mathbf{k}$ is the wavevector of the electron. Interband absorption for direct bandgapgs implies directly that $\mathbf{k}_{\text{final}} = \mathbf{k}_{\text{initial}}$, being a vertical transition, as show in Figure (3.5). In this case, absorption will only occur if $\hbar\omega \geq E_{\text{gap}}$. Photoluminescence is result of the recombination of electrons and holes, emitting a photon. However, this recombination may lead to another phenomena, like phonon emissions or even non-radiative recombinations.

It is important to note that the hole will interact attractively with the electron via Coulomb interaction, which gives rise to a bounded pair named electron-hole pair, or exciton. In monolayers of group 6B TMDs, excitonic effects are very intense due to the low screening effect [54, 55]. The binding energy of the n^{th} exciton is [26].

$$E^{(n)}_{\text{binding}} = \frac{\mu e^4}{2\hbar\varepsilon^2(n-1/2)^2}. \tag{3.17}$$

Resulting in a exciton binding energy of 0.32 eV. In Equation (3.17), μ is the exciton reduced mass of $16m_{\text{e}^-}$. The exciton binding energies in this context are more than ten times greater than those found in bulk materials and conventional two-dimensional systems composed of GaAs-like semiconductors [56]. This results shows that the optical proprieties of 1L semiconducting group 6B TMDs are majorly ruled by excitons.

Back to Figure (3.5), we see the participation of a phonon (green arrow) on the right. It happens because the CB minimum and the VB maximum are in different wavevectors. Therefore, we must rewrite the conservation laws as

$$E_{\text{final}} = E_{\text{initial}} + \hbar\omega_i \pm \hbar\Omega. \tag{3.18}$$

$$\mathbf{k}_{\text{final}} = \mathbf{k}_{\text{initial}} \pm \mathbf{q}. \tag{3.19}$$

In which $\hbar\Omega$ is the energy of the phonon and $\mathbf{q}$ is its wavevector. $\pm$ indicates that the phonon may be created of annihilated. The indirect transition is a second order process, which means it is less likely to happen. This translates in a much weaker light absorption in the close range of E_{gap} if compared with direct transitions.

Chapter 4

Nonlinear optical phenomena

Every optical effect emerges from disruption of a certain material caused by the incidence of a light beam, *id est*, of an electromagnetic perturbation in the medium as previously discussed. In order to describe any optical phenomenon, we shall then use the physical quantity "polarization", which quantifies the effects of these perturbations. Generally speaking, polarization can be expressed as being the sum of a linear term and a nonlinear term.

$$\mathbf{P}(\mathbf{x}, t) = \mathbf{P}_{\text{linear}}(\mathbf{x}, t) + \mathbf{P}_{\text{nonlinear}}(\mathbf{x}, t). \tag{4.1}$$

Linear and nonlinear optical effects *always* takes place when light interacts with matter. However, for low light intensities (weak fields), the polarization can be approximated as the linear term. In these cases, the polarization takes form

$$\mathbf{P}(\mathbf{x}, t) \approx \varepsilon_0 \chi^{(1)} \cdot \mathbf{E}(\mathbf{x}, t). \tag{4.2}$$

For this reason, we are able to represent linear optical phenomena such as absorption and Raman Scattering (as described in **Chapter 3**). In order to observe expressive nonlinear effects, such as Second Harmonic Generation (SHG) and Four Wave Mixing (FWM), we need more intense sources. In regimes of large light intensities, the material will exhibit noticeable nonlinear responses. Thus, the nonlinear polarization can be written as

$$\mathbf{P}_{\text{nonlinear}}(\mathbf{x}, t) = \varepsilon_0 \left(\sum_{j,k} \chi^{(2)}_{ijk} E_j E_k + \sum_{j,k,\ell} \chi^{(3)}_{ijk\ell} E_j E_k E_\ell + \cdots \right). \tag{4.3}$$

Similarly to the linear case, for which we need a second order tensor to have full information of the material, for higher order processes we will need higher order tensors. For example, the SHG phenomenon, which has second-order nonlinear nature, requires a third-order tensor to be represented, $\chi^{(2)}$. As a rule, a n^{th} order nonlinear process shall be seen thru susceptibility $\chi^{(n)}$, a $n+1^{\text{th}}$ rank tensor with 3^{n+1} terms, therefore third-order nonlinear effects require fourth order tensors to be represented. Note for obtain relevant nonlinear polarization effects we need higher intensities beams due to tensors' elements values are very small ($\chi^{(2)} \sim 10^{-6}$ and $\chi^{(3)} \sim 10^{-12}$ in the International System of Units). For this reason, nonlinear optical effects were only observed after the creation of lasers [57].

Nonlinear phenomena cause the medium's polarization to create additional frequency components that are absent in the initial radiation field. These newly generated frequency components act as sources of the electromagnetic field's new frequency components. Below, we explore how Maxwell's equations explain the generation of these additional field components. Additionally, we examine how the nonlinear interaction leads to the coupling of different frequency components of the field.

Atomic response exhibits nonlinearities, causing the atoms to generate an oscillating dipole moment. In the absence of external influences, a solitary atom would emit dipole radiation at this frequency. In a material sample, the multitude of atomic dipoles oscillate with varying phases that correspond to the phases of the incident fields. Proper alignment of the relative phases of these dipoles allows the radiation fields of each dipole to combine constructively in the forward direction, producing a distinct and focused beam.

We shall now examine the wave equation governing the propagation of light in a nonlinear optical medium. To derive this equation, we shall start with Maxwell's equations.

$$\vec{\nabla} \cdot \mathbf{D} = \rho. \tag{4.4}$$

$$\vec{\nabla} \cdot \mathbf{B} = 0. \tag{4.5}$$

$$\vec{\nabla} \times \mathbf{E} = -\frac{\partial \mathbf{B}}{\partial t}. \tag{4.6}$$

$$\vec{\nabla} \times \mathbf{H} = \frac{\partial \mathbf{E}}{\partial t} + \mathbf{J}. \tag{4.7}$$

We want to explore the solutions in regions of space in which $\mathbf{J} = 0$ and $\rho = 0$. We also assume that the material is nonmagnetic, we may say

$$\mathbf{B} = \mu_0 \mathbf{H}. \tag{4.8}$$

As discussed, polarization quantifies optical processes in matter. Nonlinearty means we may write a relation between **E** and **D**.

$$\mathbf{D} = \varepsilon_0 \mathbf{E} + \mathbf{P}. \tag{4.9}$$

The polarization vector **P** typically exhibits a nonlinear dependence on the local electric field strength **E**. Using Equations (4.8) and (4.9) and the fact current density and charge density are zero in free space, we can affirm that

$$\vec{\nabla} \times \vec{\nabla} \times \mathbf{E} + \mu_0 \frac{\partial^2 \mathbf{D}}{\partial t^2} = 0. \tag{4.10}$$

Using Equation (4.9) we will have

$$\vec{\nabla} \times \vec{\nabla} \times \mathbf{E} = \frac{1}{c^2} \frac{\partial^2 \mathbf{E}}{\partial t^2} = -\frac{1}{\varepsilon_0 c^2} \frac{\partial^2 \mathbf{P}}{\partial t^2}. \tag{4.11}$$

Equation (4.11) relates a time-varying polarization, which can potentially serve as a source of new components for the applied optical field, to the strength of the optical field $\mathbf{E}(t)$. It is worth noting that the polarization of a material is generated through its interaction with the electromagnetic field. In the case of a linear response, the relationship between the time-varying polarization $\mathbf{P}(t)$ and the optical field strength $\mathbf{E}(t)$ can be expressed using Equation (4.2).

4.1 Sum and Difference Frequency Generations

Second order nonlinear processes are described by the first term in Equation (4.3), which polarization is given as

$$\mathbf{P}^{(2)}(t) = \varepsilon_0 \chi^{(2)} \mathbf{E}^2(t). \tag{4.12}$$

Lets set up an experiment in which two fields with different frequencies interact with a second order nonlinear media. The incident field is given by

$$\mathbf{E}(t) = \mathbf{E}_1 e^{-i\omega_1 t} + \mathbf{E}_2 e^{-i\omega_2 t} + \text{complex conjugate}. \tag{4.13}$$

Nonlinear polarization is then

$$\begin{aligned} \mathbf{P}^{(2)}(t) = \varepsilon_0 \chi^{(2)} \big[& \mathbf{E}_1^2 e^{-2i\omega_1 t} + \mathbf{E}_1^2 e^{-2i\omega_2 t} + 2\mathbf{E}_1 \mathbf{E}_2 e^{i(\omega_1+\omega_2)t} \\ & + 2\mathbf{E}_1 \mathbf{E}_2^* e^{i(\omega_1-\omega_2)t} + \text{c.c.} \big] + 2\varepsilon_0 \chi^{(2)} \left[\mathbf{E}_1 \mathbf{E}_2^* + \mathbf{E}_1^* \mathbf{E}_2 \right]. \end{aligned} \tag{4.14}$$

The last term in Equation (4.14) emerges from optical rectification phenomena, a nonlinear effect with constant value. The third term in Equation (4.14) is associated with Sum Frequency Generation and the fourth with Difference Frequency Generation.

Sum Frequency Generation (SFG) is a nonlinear optical process in which two input frequencies are combined to generate a new output frequency that is the sum of the two input frequencies. Specifically, when two input beams of different frequencies interact with a material, the resulting SFG process generates a new beam of light at a frequency that is equal to the sum of the two input frequencies.

Difference Frequency Generation (DFG) is a nonlinear optical process in which two input frequencies are combined to generate a new output frequency that is the difference between the two input frequencies. Specifically, when two input beams of different frequencies interact with a material, the resulting DFG process generates a new beam of light at a frequency that is equal to the difference between the two input frequencies.

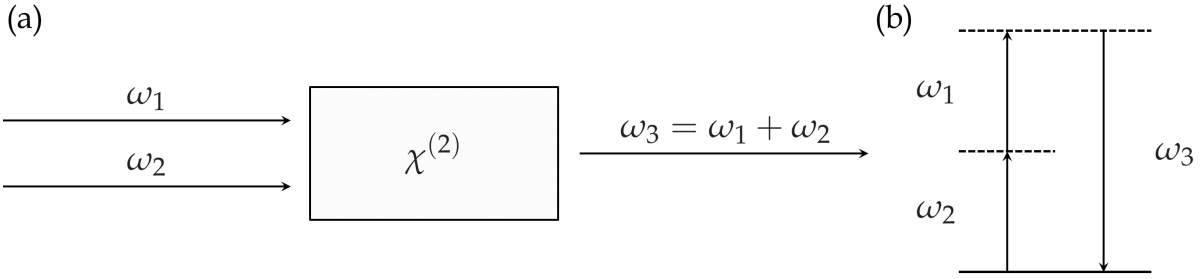

Figure 4.1: Sum-frequency generation. **(a)** Geometry of the interaction. **(b)** Energy-level description.

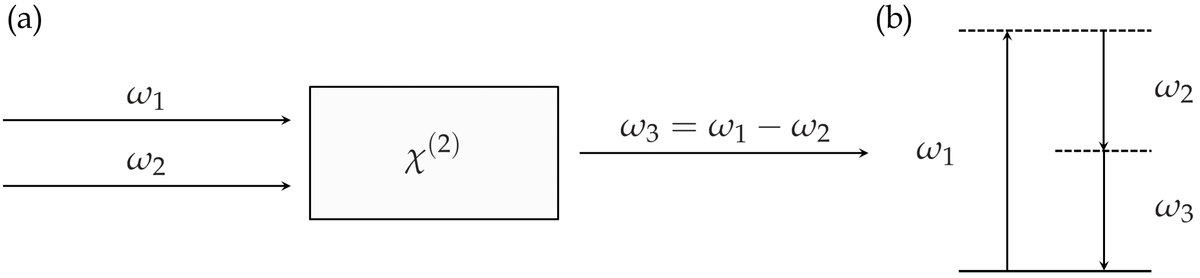

Figure 4.2: Difference-frequency generation. **(a)** Geometry of the interaction. **(b)** Energy-level description.

4.2 Second Harmonic Generation

Being a particular case of Sum Frequency Generation (with $\omega_1 = \omega_2$ in Figure (4.1)), Second Harmonic Generation was firstly employed in 1961 by Franken *et al.* using a ruby laser at 694.3 nm and observing emission from a quartz crystal. The response was a beam with 347.2 nm. [58, 59].

The first two terms in Equation (4.14) refers to Second Harmonic Generation for two incident fields, in which emits a double-energy signal with respective field frequency.

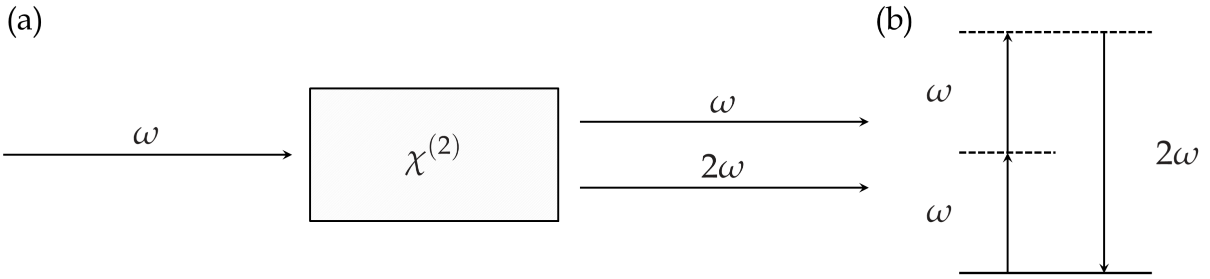

Figure 4.3: (a) Geometry of Second Harmonic Generation. **(b)** Energy-level diagram describing Second Harmonic Generation.

Note that Equation (4.12) directly implies that structures with symmetrical center cannot be observed using SHG technique once its signal depends on $\mathbf{E}^2(\mathbf{x}, t)$. It is trivial to see if we consider an inverse electric field excitation, resulting in inverse polarization. Then: $\mathbf{E}(\mathbf{x}, t) \to -\mathbf{E}(\mathbf{x}, t)$ and $\mathbf{P}(\mathbf{x}, t) \to -\mathbf{P}(\mathbf{x}, t)$ (in general). Thus

$$\mathbf{P}^{(2)}_{\text{nonlinear}}(\mathbf{x}, t) = \varepsilon_0 \chi^{(2)} \mathbf{E}^2(\mathbf{x}, t). \tag{4.15}$$

$$-\mathbf{P}^{(2)}_{\text{nonlinear}}(\mathbf{x}, t) = \varepsilon_0 \chi^{(2)} \left(-\mathbf{E}(\mathbf{x}, t)\right)^2. \tag{4.16}$$

Leading directly to $\chi^{(2)} = 0$, with no second order nonlinear response. Other manner to see this is to consider that a material with symmetrical center is going to emit two second order nonlinear signals out of phase, destructively interfering each other. Despite structures with symmetry center presents no second order linear response, this do not prohibit it from presenting third order nonlinear response.

As a result, this process occurs only can be observed in materials that lack a center of symmetry, such as certain crystals, and it is often used to probe the surface and bulk properties of materials, as well as for generating new sources of coherent light at higher frequencies.

4.3 Four Wave Mixing

Four Wave Mixing is a third-order nonlinear phenomenon which signal depends on the third-order nonlinear polarization. To describe this interactions, we shall use $\chi^{(3)}$, which has 81 terms.

$$\mathbf{P}^{(3)}_{\text{nonlinear}}(\mathbf{x}, t) = \varepsilon_0 \chi^{(3)} \mathbf{E}^3(t). \tag{4.17}$$

The electric field has the form

$$\mathbf{E}(t) = \mathbf{E}_1 e^{-i\omega_1 t} + \mathbf{E}_2 e^{-i\omega_2 t} + \mathbf{E}_3 e^{-i\omega_3 t} + \text{complex conjugate}. \tag{4.18}$$

Calculating polarization from Equation (4.17) using Equation (4.18) we find an extensive nonlinear polarization expression with a wide range of possible values for ω_4 frequencies, summing up to 22 possible responses (not counting with their negative counterparts). Every FWM phenomenon is followed by the emission of every possible value of ω_4 in proportion to its coefficients..

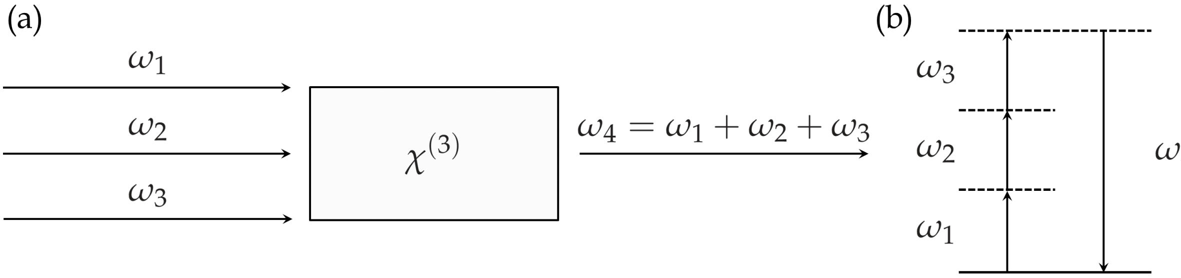

Figure 4.4: Possible mixing process that can occur when three input waves interact in a medium characterized by a $\chi^{(3)}$ susceptibility. **(a)** Geometry of the interaction. **(b)** Energy-level description.

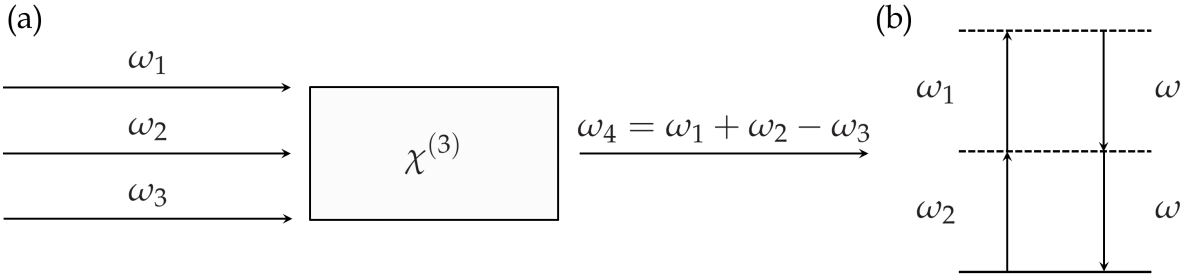

Figure 4.5: Possible mixing process that can occur when three input waves interact in a medium characterized by a $\chi^{(3)}$ susceptibility. **(a)** Geometry of the interaction. **(b)** Energy-level description.

The "simplest" case of Four Wave Mixing is named Third Harmonic Generation (THG), an analogous of SHG compared with SFG, which results from interaction of three photons with the same energies, lets say $\hbar\omega$. In this case, the material is emitting a photon with energy $3\hbar\omega$ (case of the Figure (4.4) with $\omega_1 = \omega_2 = \omega_3$).

At first glance, the figures above may seem confusing and even misleading, particularly Figure (4.5), in which ω_3 apparently is not contributing with energy to reach a excited level (dashed line), but it is part of the radiative emission. To better understand what is happening, we may think of a nonlinear medium with third-order susceptibility mediates incident photons in order to conserve energy. To be a little bit simpler, we can think in three pool balls interacting in different manners and the medium have to conserve energy by throwing another ball.

In our experiments, we are interested in a particular energy signal in which $\omega_4 = \omega_1 + \omega_2 - \omega_3$ (same as shown in Figure (4.5) with $\omega_1 = \omega_2 \equiv \omega'$) often named Degenerated Four Wave Mixing (DFWM). Applying conservation of energy principle we shall obtain

$$\lambda_4 = \frac{\lambda' \lambda_3}{2\lambda_3 - \lambda'}. \tag{4.19}$$

Another interesting DFWM particular setting is named Coherent anti-Stokes Raman Spectroscopy (CARS) in which we aim to match $\omega_1 + \omega_2$ with ω_{vib}, one of material's normal vibrational Raman modes thus obtaining an intense, resonant response signal. This setup allow us to select any molecule's Raman mode we desire to enhance and see how this mode is present in certain sample, mapping the mode intensity over a sample [60].

4.4 Applications of nonlinear optical techniques

Lafetá *et al.* have shown that FWM signal are resonant within 2D TMD excitonic energies [61]. Cunha *et al.* have shown that nonlinear optical techniques can be applied to identify protein placards in retina, which may useful for identifying early Alzheimer symptoms [62]. Besides that, various nonlinear techniques can be useful for biological studies [63].

In **Chapter 5** we discuss in deeper details the time scales for several techniques we used in this work, but for simple comparison, conventional Raman maps take dozen of hours to be performed, while nonlinear images such SHG and FWM take only a few seconds. Stabilising direct equivalences in both of these phenomena along Raman measurements may be game-changing.

In this work, we expect to use techniques of linear and nonlinear optics to map defects in CVD-fabricated V-doped WS_2 monolayers. If we manage to use nonlinear optics to investigate these defects, they may be used in large-scale mapping of 2D materials in the near future.

Chapter 5

Experimental methods

5.1 Sample preparation

The samples used for the measurements presented in this thesis were synthesized in a collaboration with the group from The Pennsylvania State University (State College, PA, US), composed of researchers from several departments (Physics, Materials Science and Engineering, 2-Dimensional and Layered Materials and Engineering Science and Mechanics).

Monolayers of pristine and V-doped WS_2 were fabricated by CVD using ammonium metatungstate, $(NH_4)_6H_2W_{12}O_{40}{\cdot}xH_2O$, as tungsten precursor and vanadium dioxide, $VO(SO)_4$, as vanadium precursor. Sodium cholate, $C_{24}H_{39}NaO_5 \cdot xH_2O$, was also used as surfactant salt. Every compound was dissolved together in deionized water. The prepared solutions were spin-coated on oxidized Si substrates, followed by sulfidation at 800 °C under atmospheric pressure, as seen in Figure (5.1).

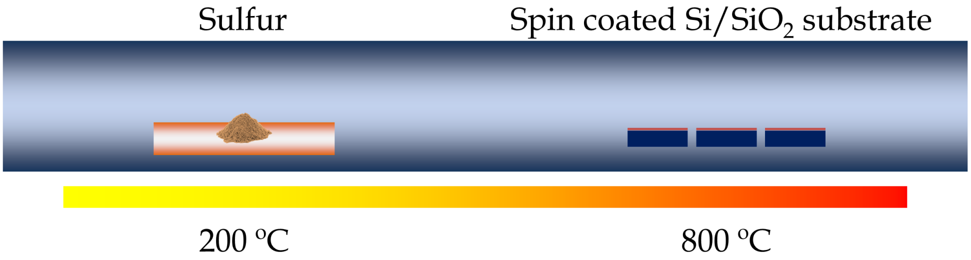

Figure 5.1: Schematic of the synthesis of monolayer V-doped WS_2.

Grown pristine and V-doped WS_2 monolayers have regular triangular shapes of 10–50 µm range. Different concentrations of vanadium precursor yields different concentrations of V in the flakes. The higher the concentrations, the higher the chances of compromising crystallinity, edge quality, and flatness. Flakes with average vanadium concentrations of 0.4, 2.0, and 8.0% were produced. Other precursors along with other concentrations were primarily discussed in our collaborator's article [10].

To confirm the presence of substitutional V atoms at W sites and to ascertain its concentration high-angular annular dark-field scanning transmission electron microscopy (HAADF-STEM) measurements were performed.

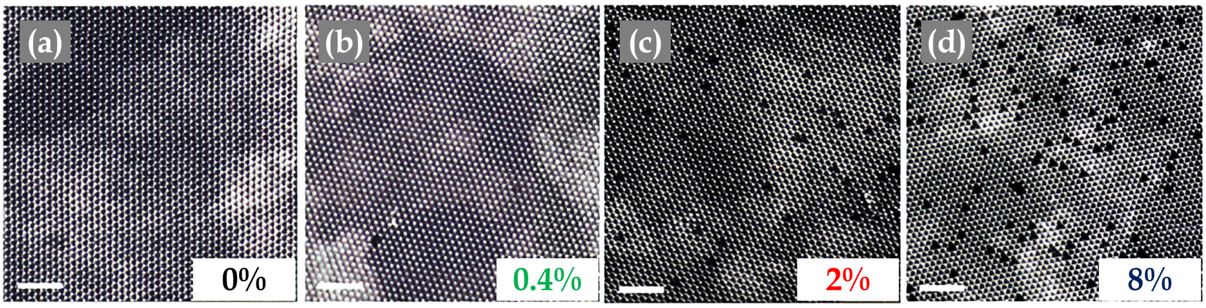

Figure 5.2: Atomic resolution HAADF-STEM images for **(a)** pristine and vanadium doped WS_2 monolayers at **(b)** 0.4, **(c)** 2 and **(d)** 8% at V. Scale bars are 2 nm. Adapted from [10].

In contrast with its pristine counterparts, vanadium-doped WS_2 monolayers present a magnetic response at room conditions, while pure crystals behaves diamagnetically. To observe such behavior in pure Group 6 TMDs, low-temperature regimes are required.

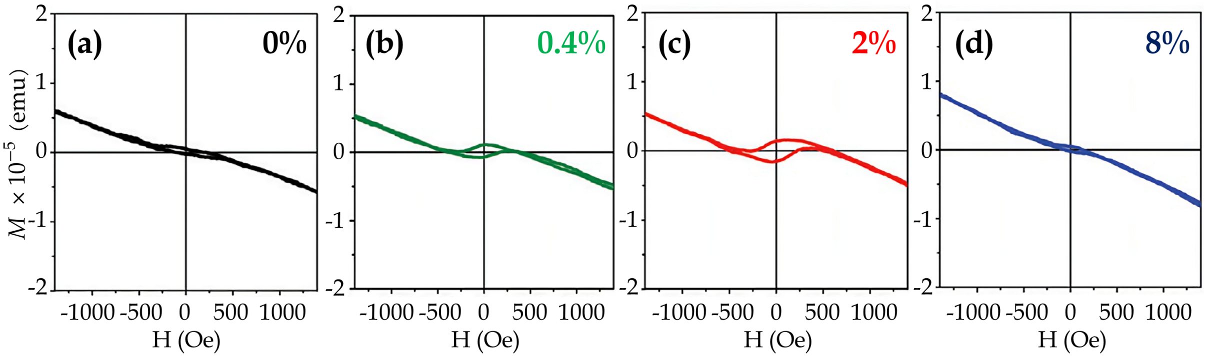

Figure 5.3: Magnetization *versus* field loops at 300 K for **(a)** pristine and vanadium doped WS_2 monolayers at **(b)** 0.4, **(c)** 2 and **(d)** 8 at % V. Adapted from [10].

5.2 Fluorescence images

Fluorescence images (FI) images were taken using an Olympus BX51 Fluorescence Microscope, in which we used a Hg lamp as an exciting light source. This light is then directed through the objective and onto the specimen by a special dichroic mirror that reflects certain wavelengths while passing through others (green long pass). All FI were taken at room temperature.

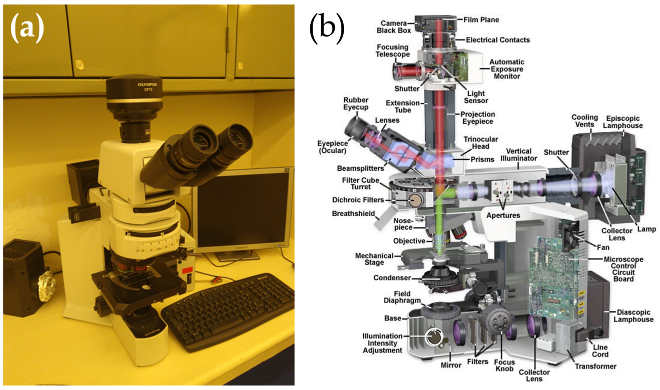

Figure 5.4: **(a)** Olympus BX51 Fluorescence Microscope and **(b)** its detailed scheme. Adapted from `lcpnano.ufmg.br`.

5.3 Raman and Photoluminescence measurements

Raman and PL were performed using a WITec Alpha 300 spectrometer exciting the samples with a 457 nm or 532 nm laser. For Raman, we used a 1800 gr/mm grating and power ∼300 µW. For PL, we used a 600 gr/mm grating and power ∼150 µW. To collect the data, it was used an Electron Multiplying Charge-Coupled Device (EMCCD). An Zeiss 100× objective with NA of 0.9 was used to focus the scattered light. Raman and PL data were analysed using a dedicated software, PortoFlow[1]. All Raman and PL measurements were performed at room temperature.

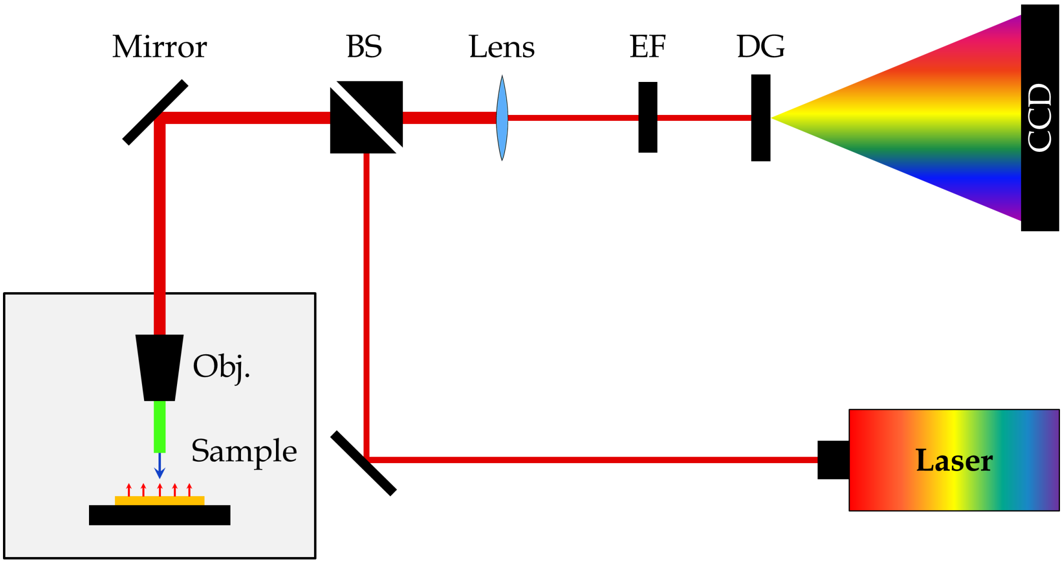

Figure 5.5: Simplified scheme of a Raman spectrometer. BS: beam splitter; EF: edge filter; DG: diffraction grating; CCD: charge coupled device.

---

[1] PortoFlow is a dedicated software developed for spectroscopic data analysis developed by FabNS. Web page: `fabns.com.br`.

5.4 Nonlinear optical measurements

SHG and FWM experiments were performed using an Optical Parametric Oscillator (OPO) beam system (APE Berlin picoEmerald) with continuous range, tunable from 750 nm to 950 nm, with 7 ps pulse width and 80 MHz repetition rate. An 40× objective with NA of 0.95 was used to focus the beam on the sample. The back-scattered nonlinear signals were collected by the same objective and then reflected by a dichroic mirror, leading the signal to a photomultiplier tube (PMT). We use a laser scanning microscope, in which the laser scan point by point and an image is generated. A simple schematic of the set-up is shown in Figure (5.6). The images were acquired using a dedicated software. Various data collection were performed changing the pump wavelength. SHG signal is collected with the aid of a 405/10 nm band-pass filter, while the pump wavelength is 810 nm. For FWM measurements we used two lasers $\omega_1 = 750$–950 nm; $\omega_2 = 1064$ nm. Thus, we detected the FWM generated by $2\omega_1 - \omega_2$ varying ω_1 from 775 to 830 nm. In this very work, we selected some values of ω_1 to match the available filters. Pump, and filters used are shown in Table (5.1). All nonlinear measurements were performed at room temperature.

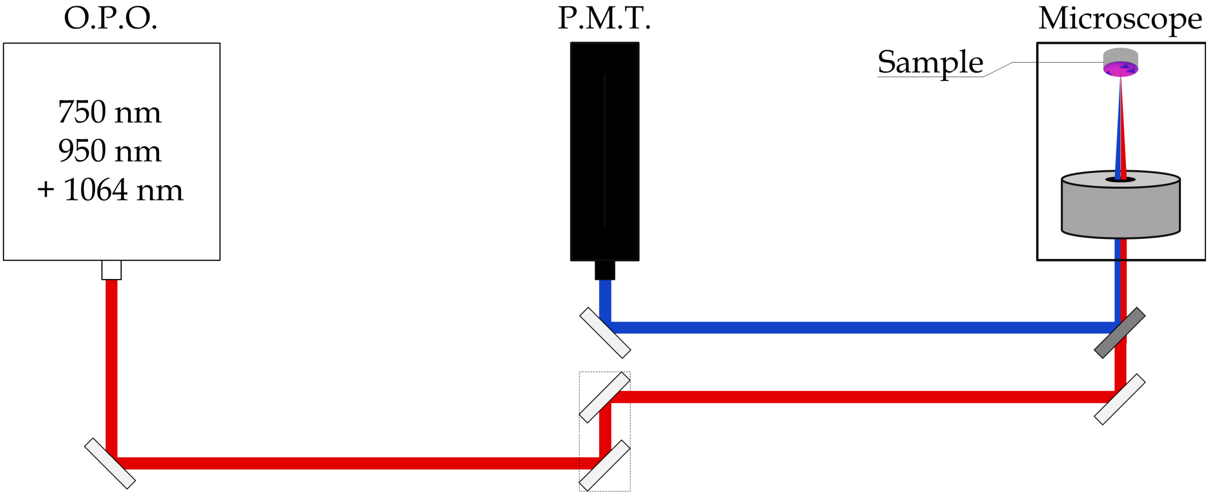

Figure 5.6: Scheme of the set-up used in all nonlinear experiments. Red lines represents the laser and blue lines the nonlinear signal. The solid rectangles are mirrors, being the darker one a dichroic mirror. Mirrors inside the dashed box are scanning mirrors.

As discussed in **Chapter 4**, our desired FWM signal wavelength is given by Equation (4.19), but every possible combination is being generated simultaneously by the media. We shall then use filters to pick our response of interest, as reported in Table (5.1). The filters are positioned between the dichroic mirror and the photomultiplier tube.

Table 5.1: Tunable pump wavelengths to generate certain FWM signal with fixed 1064 nm laser along the filters used for every excitation beam. All values are in nanometers. A generic filter n/m nm means its band-pass range is $(n \pm m/2)$ nm. The correspondent photon energy of each FWM signal are displayed.

Pump	775	783	788	793	807	820	822	830
FWM	610	620	626	632	650	667	670	680
Filter	605/15	620/60	632/22	632/22	655/40	661/11	670/10	680/13
E **(eV)**	2.03	1.99	1.98	1.96	1.90	1.86	1.85	1.82

5.5 Scanning Probe Microscopy

Scanning Probe Microscopy (SPM) is a generic term used to refer to a family of techniques which share a common element of usage of a mechanical probe to explore a wide range of physical properties of surfaces. Every technique is tailored based on the specific probe-sample interaction it monitors. These methods not only enable highly detailed morphological analyses of the samples under examination but also facilitate the generation of diverse information on intrinsic properties like hardness, magnetic, and electrical properties [64, 65].

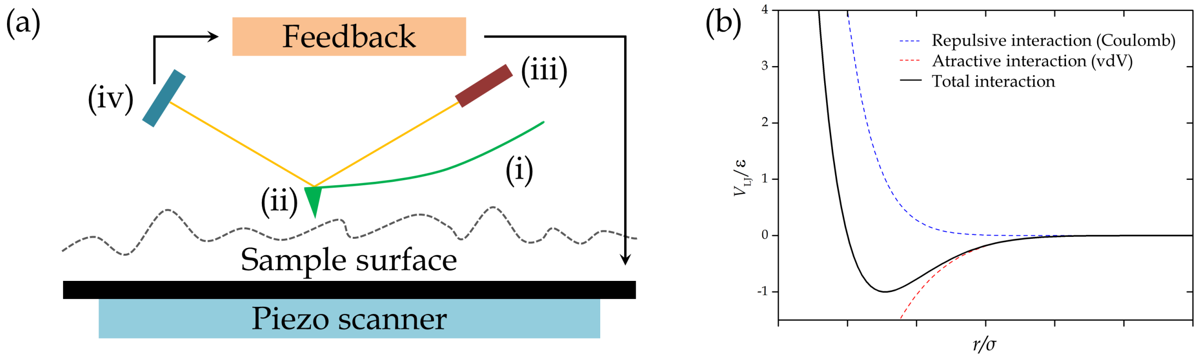

Figure 5.7: **(a)** Simplified scheme of a SPM. (i) Cantilever, (ii) probe, (iii) laser, and (iv) photodiode. **(b)** Inter-atomic interaction potential (V_{LJ}) plotted as function of the distance r as an approximation for the tip-sample interaction. In this representation, the blue curve signifies a strictly repulsive interaction, contrasting with the red curve that denotes a purely attractive interaction. The black curve intricately combines long-range attractive forces with short-range repulsive forces, known as the Lennard-Jones potential.

SPM measurements were performed in collaboration with the group of Laboratory of Nanoscopy (*Laboratório de Nanoscopia*) at UFMG. The experiments were conducted and discussed by collaborators Ana Paula Moreira Barboza and Bernardo Neves from Federal University of Ouro Preto (UFOP) and UFMG, respectively. The collected data were discussed with both Ana and Bernado Neves from UFMG. All

SPM measurements were performed at room temperature.

Atomic Force Microscopy (AFM). The fundamental principle of the AFM is depicted in Figure (5.7). This technique is based on an AFM probe, equipped with a sharp tip, across a sample surface in a raster pattern. Typically crafted from silicon or silicon nitride, the AFM tip is integrated near the flexible end of an AFM cantilever. A piezoelectric ceramic scanner controls both the lateral and vertical positioning of the AFM probe concerning the surface.

As the AFM tip traverses areas with varying heights, it prompts shifts in the deflection of the AFM cantilever. This deflection is monitored via a laser beam directed onto the backside of the AFM cantilever, which then interacts with a position-sensitive photodetector. A feedback loop modulates the vertical movement of the scanner to sustain nearly constant AFM cantilever deflection, thereby maintaining a consistent interaction force. The tracked coordinates of the AFM tip during the scan process are amalgamated to construct a three-dimensional topographic representation of the surface [66].

In Tapping Mode, the AFM probe cantilever undergoes oscillation driven by a piezoelectric actuator at or close to its fundamental resonance frequency, often ranging from several tens to several hundred kilohertz. The AFM probe is gradually brought nearer to the sample surface until the tip slightly touches the surface during the lower phase of the AFM cantilever's oscillation, thereby damping its oscillation amplitude. To maintain consistency, a feedback loop regulates a stable AFM cantilever oscillation amplitude, ensuring a constant interaction force throughout the process [65].

Electrostatic Force Microscopy (EFM). This technique stands as a prevalent electrical AFM operational mode, offering valuable qualitative insights into the electric field gradients across a sample surface. This method facilitates the generation of contrast linked to the sample's electrical properties. EFM operates within the amplitude modulation mode, a dynamic force mode wherein a cantilever, coated thinly with an electrically conductive material, oscillates at its resonance frequency [67].

Lateral Force Microscopy (LFM). This technique shares similarities with the AFM technique, but LFM is performed employing a four-segment photodetector and scanning, allowing the microscope to detect the vertical deflection of the AFM cantilever and also discern its torsional twisting, typically induced by lateral forces, such as friction, acting on the AFM probe tip. In contrast to AFM, LFM measurements are performed using a probe to friction-interact with the sample, in forward and backward senses, so it is possible to remove height artifacts and enhance torsion differences caused by different domains of your sample, as shown in Figure (5.8) [68].

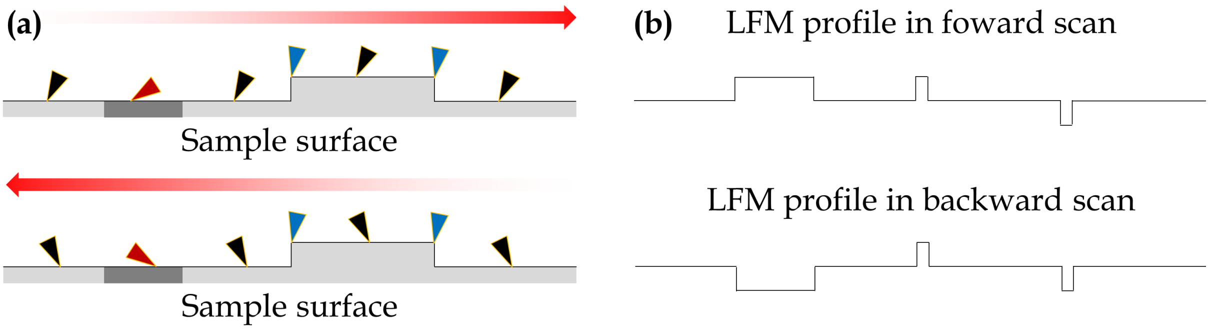

Figure 5.8: Simplified scheme of a LFM measurement. **(a)** Forward and backward scan direction measurements. **(b)** Profiles of the LFM signal in forward and backward scan direction.

AFM and LFM performed were acquired using a CSC37 No Al probe (MikroMash), with $k = 0.3$ N/m and $\omega_0 = 20$ kHz. EFM experiments were performed using a HQ:XSC11 (MikroMash), with $k = 7$ N/m and $\omega_0 = 155$ kHz. Experiments done with the Nanoscope V MultiMode8 SPM (Bruker Instruments). LFM signal are presented as the difference in lateral torsion between scans in forward and backward. This procedure enhance the friction diference and minimizes topographic artefacts. These techniques were briefly discussed because they are not the main scope of this work, but they will show great relevance in **Chapter 6**.

Chapter 6

Experimental results and discussions

The previous chapter described the growth process of pristine and V-doped WS_2 monolayers that exhibited regular triangular shapes of 10–50 µm range. In reason of the good quality of synthesis and the abundance of samples, we were able to choose which flakes are best for our measurements. We selected various flakes with regular triangular shapes to perform our experiments.

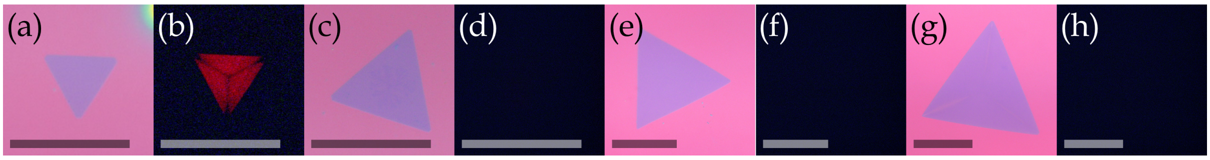

Figure 6.1: Optical and fluorescent images (FI) of **(a,b)** pristine WS_2, **(c,d)** 0.4, **(e,f)** 2.0, and **(g,h)** 8.0% at V–WS_2 flakes. Scale bars are 50 µm.

Figure (6.1) shows the size pattern of the triangular flakes. In general, 2.0 and 8.0% at V–WS_2 are larger, with ∼100 µm side length. Figure (6.1b) shows that the emission of the sample in the pristine image, and it is noticeable that the PL emission is reduced in the dark lines. These dark line are the same regions reported by Rosa *et al.* in which defects accumulate preferentially. Figures (6.1d),(6.1f), and (6.1g) show no emission, which shows that doping effects decrease the PL emission.

6.1 Photoluminescence spectra

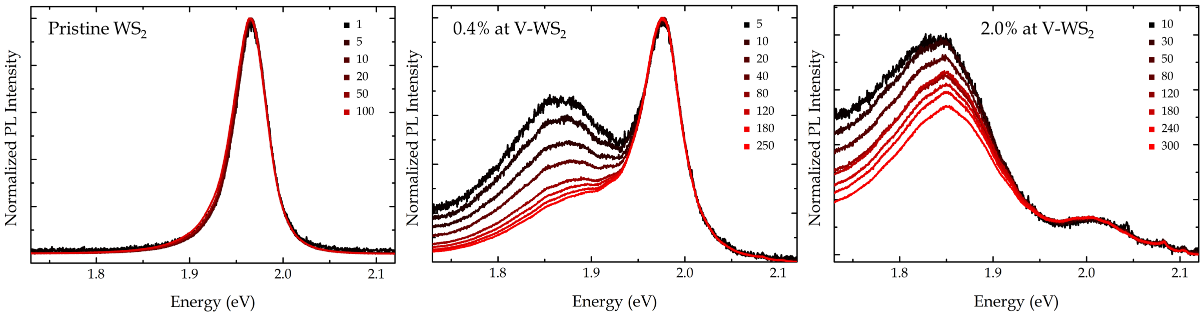

Figure 6.2: Power-dependent PL spectra of pristine, 0.4, and 2.0% at V–WS_2. Powers are in top right of each graph in µW.

The results shown in Figure (6.2) were obtained by using a 561 nm CW diode laser. The laser beam was focused on the sample by a 40× objective with NA 0.95. Backscattered signal was collected by the same objective and directed to the spectrometer (Andor Shamrock 303i) equipped with a sensitive CCD (Andor IDUS DU401A-BV). A 561 nm longpass filter was used.

Power-dependent PL spectra were normalized with respect to higher energy peaks. Figure (6.2a) show only one peak at 1.96 eV. This peak is related to the A exciton. In Figure (6.2b,c), we see two energy peaks: one at 1.8–1.9 eV (P_1) and the other at 2.0 eV (P_2). P_2 is linear with respect of the power, *id est*, if we double the power, the PL response will double. This behavior means this peak is related with an exciton [69]. While P_2 presents a blueshift within the increase of V concentration, P_1 presents a redshift and its shape changes with the incident power, showing a sublinear behavior, which may indicate that this peak is related to a radiative recombination process from a donor or to an acceptor level [69].

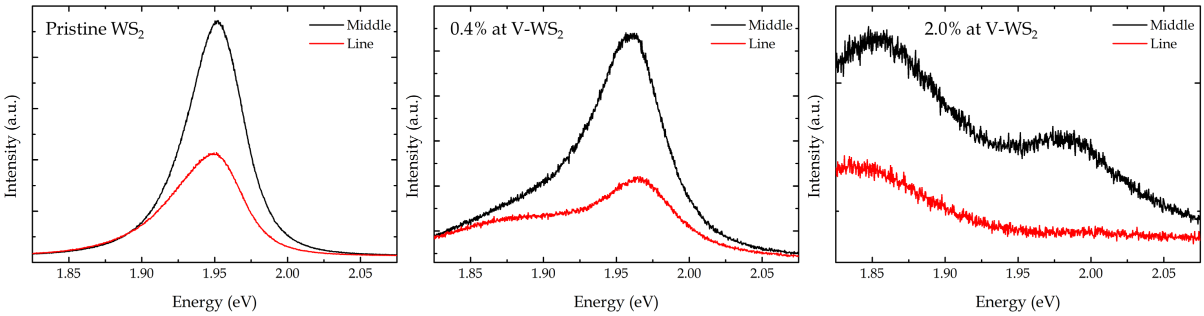

Figure 6.3: PL spectra of pristine, 0.4, and 2.0% at V–WS_2 acquired with ∼ 150 µW.

Figure (6.2) displays a power-dependent PL analysis *without* caring about spatial defect accumulation regions we previously discussed. In order to understand how the PL changes spatially, we performed a hyperspectral PL map. Figure (6.3) compares the PL response between the bisection of the flakes and the rest of the flake.

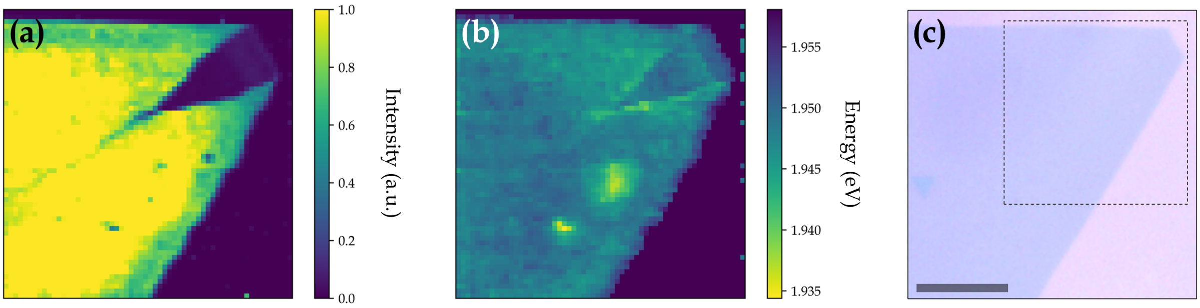

Figure 6.4: Hyperspectral PL map. **(a)** Intensity and **(b)** energy maps with 532 nm excitation beam of pristine WS_2 sample. **(c)** Optical image of the region. Scale bar is 10 µm. Map dimensions are 20 µm × 20 µm.

Figure (6.4) shows hyperspectral PL maps for pristine WS_2. Figure (6.4) shows a decreased PL intensity in the defect line, but there is no energy shift in Figure (6.4b).

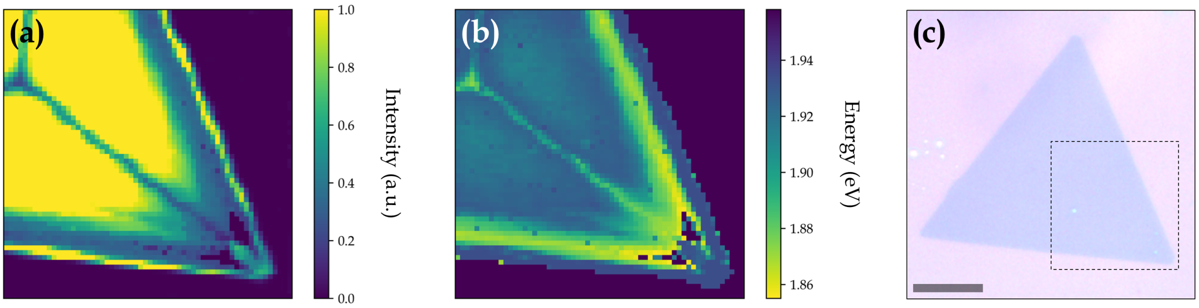

Figure 6.5: Peak 1 **(a)** intensity and **(b)** energy maps with 532 nm excitation beam of 0.4% at V–WS_2 sample. **(c)** Optical image of the region. Scale bar is 10 µm. Map dimensions are 20 µm × 20 µm.

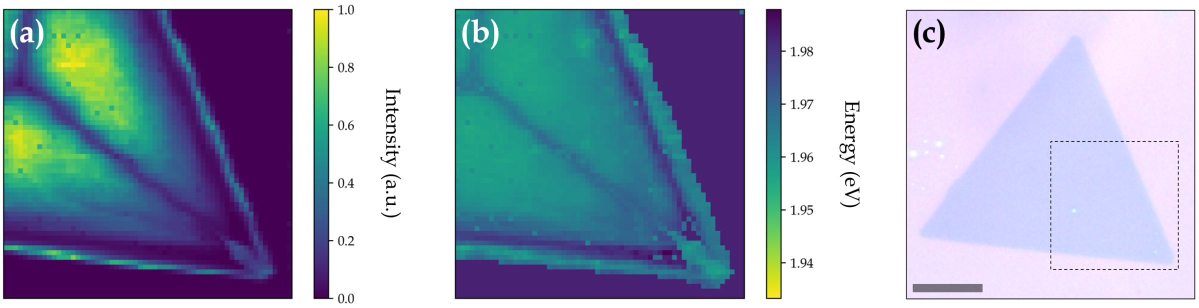

Figure 6.6: Peak 2 **(a)** intensity and **(b)** energy maps with 532 nm excitation beam of 0.4% at V–WS_2 sample. **(c)** Optical image of the region. Scale bar is 10 µm. Map dimensions are 20 µm × 20 µm.

Figures (6.5) and (6.6) shows hyperspectral PL maps for 0.4% at V–WS_2 for both P_1 and P_2, respectively. For P_2, we see a vertiginous decrease in Figures (6.5a) of P_1

intensity along with a small blueshift (~0.012 eV) in energy at the defect line. P_1 also shows a decrease in intensity, but notably much less in comparison with P_2. A redshift is observed for P_1 in the defect line.

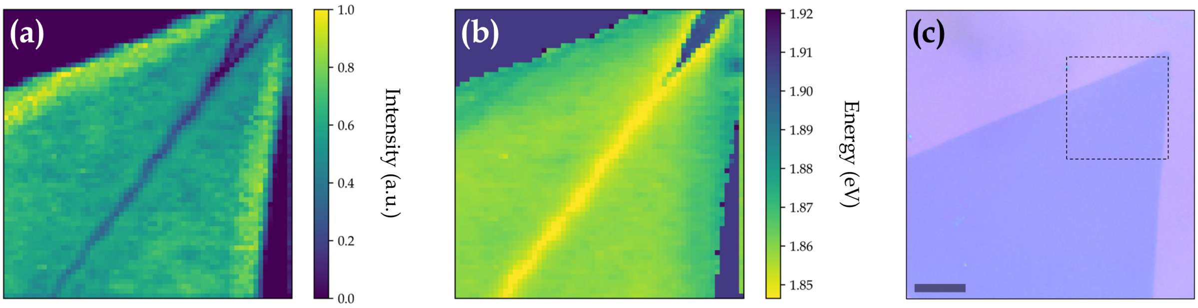

Figure 6.7: Peak 1 **(a)** intensity and **(b)** energy maps with 532 nm excitation beam of 2.0% at V–WS_2 sample. **(c)** Optical image of the region. Scale bar is 10 µm. Map dimensions are 20 µm × 20 µm.

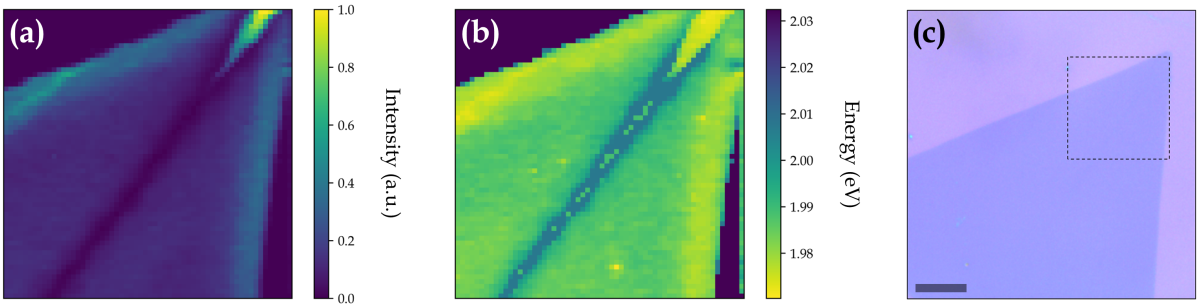

Figure 6.8: Peak 2 **(a)** intensity and **(b)** energy maps with 532 nm excitation beam of 2.0% at V–WS_2 sample. **(c)** Optical image of the region. Scale bar is 10 µm. Map dimensions are 20 µm × 20 µm.

Figures (6.7) and (6.8) show hyperspectral PL maps for 2.0% at V–WS_2 for both P_1 and P_2. These images are very similar to the hyperspectral PL maps for 0.4% at V–WS_2. Again for P_2, Figure (6.8b) shows a decrease of the intensity along the defect line with a small blueshift in energy (~0.21 eV). Figure (6.7a) shows that P_1 also shows a decrease in intensity in the defect line, but notably much less in comparison with P_2. Figure (6.7) shows a redshift is also observed for P_1 in the defect line.

6.2 Raman spectra

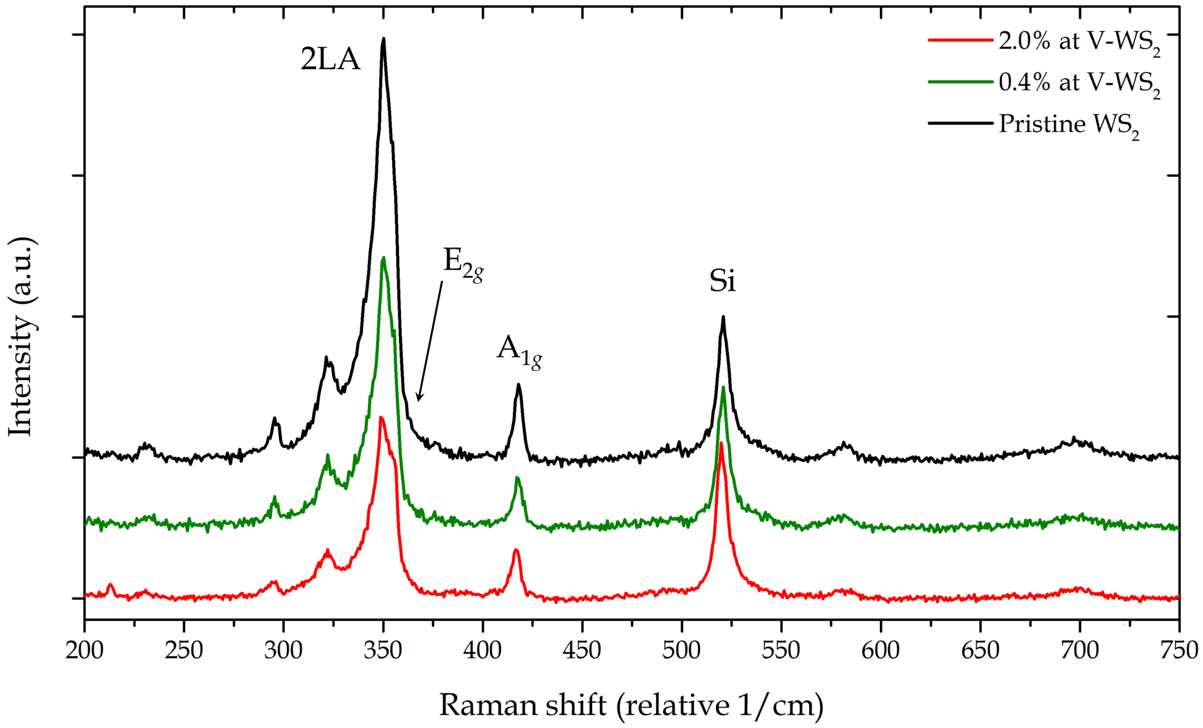

Figure 6.9: Raman spectra acquired with 532 nm excitation beam for pristine, 0.4%, and 2.0% at V–WS_2. Peak position and intensities from all spectra were normalized by Silicon peak position and intensity at 521.6 cm^{-1}.

Generally speaking, PL measurements give a clue regarding the stacking (number of layers) of the sample once the quantum yield from 1L and 2L in group 6B TMDs ratio is in order of 10^2 [24]. Alternatively, Raman spectroscopy may also provide this information. For excitation energies close to 514.5 nm, the intensity ratio of the 2LA and A_{1g} is around 2.2 for monolayers. For bilayers, this ratio is 1.0. This ratio decrease even more to trilayer and bulk regimes [70]. It is due to the A_{1g} mode corresponding to the vibration out of the plane.For the sake of completeness, we wanted to check that we had monolayer WS_2 samples. The spectra shown in Figure (6.9) clearly indicates the monolayer features of the samples under study in this work.

Based on previous research, our first hypothesis was that dopant atoms would replace tungsten atoms at a much higher density in the bisection lines of the flakes [9]. If so, we predicted to observe a blueshift of the E_{2g} mode once its frequency depends on the mass of W atoms. Once V atoms are lighter, a higher vibrational mode frequency is expected, while smaller shift would occur for A_{1g} mode since the metal atoms do not participate in the vibration.

To pursue these evidence, we performed a hyperspectral Raman map to investigate how the vibrational modes change. However, we were particularly interested in first order Raman modes (see **Chapter 3**). Therefore, we performed the hyperspectral measurements out of resonance with a 457 nm excitation beam. In this regime, we only observe E_{2g} and A_{1g} modes, so it is easier to evaluate its intensity and frequency.

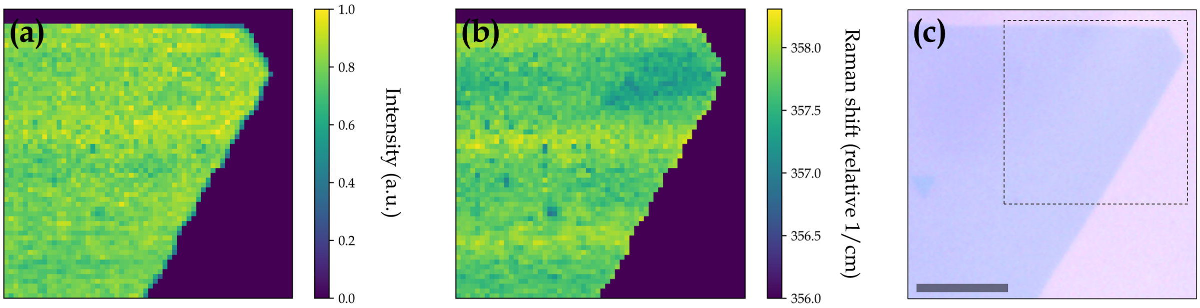

Figure 6.10: E_{2g} mode **(a)** intensity and **(b)** energy maps with 457 nm excitation beam of pristine WS_2 sample. **(c)** Optical image of the region. Scale bar is 10 µm. Map dimensions are 20 µm × 20 µm.

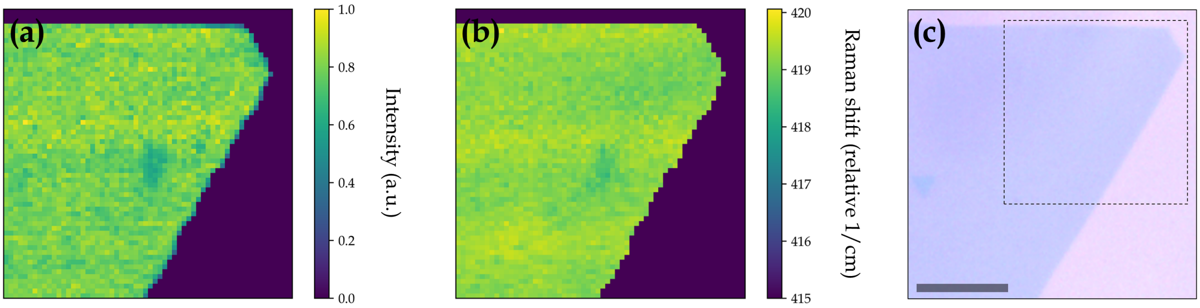

Figure 6.11: A_{1g} mode **(a)** intensity and **(b)** energy maps with 457 nm excitation beam of pristine WS_2 sample. **(c)** Optical image of the region. Scale bar is 10 µm. Map dimensions are 20 µm × 20 µm.

Figures (6.10) and (6.11) display intensity and frequency maps for both E_{2g} and A_{1g} Raman modes of pristine WS_2. As shown, these modes keep almost unaffected in terms of intensity and frequency. Despite PL measurements accuse changes in the electronic structures, it is not evident any effect in vibrational properties.

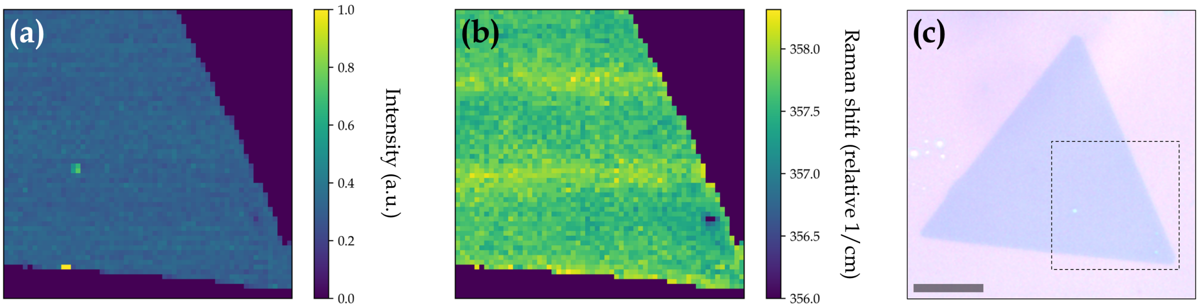

Figure 6.12: E_{2g} mode **(a)** intensity and **(b)** energy maps with 457 nm excitation beam of 0.4% at V–WS_2 sample. **(c)** Optical image of the region. Scale bar is 10 µm. Map dimensions are 20 µm × 20 µm.

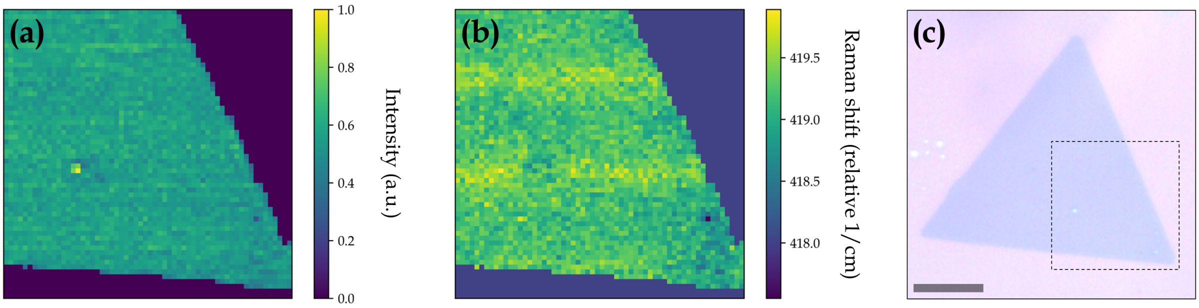

Figure 6.13: A_{1g} mode **(a)** intensity and **(b)** energy maps with 457 nm excitation beam of 0.4% at V–WS_2 sample. **(c)** Optical image of the region. Scale bar is 10 µm. Map dimensions are 20 µm × 20 µm.

Figures (6.12) and (6.13) display intensity and frequency maps for both E_{2g} and A_{1g} Raman modes of 0.4% at V–WS_2. Similarly observed for pristine WS_2, these modes are not significantly affected.

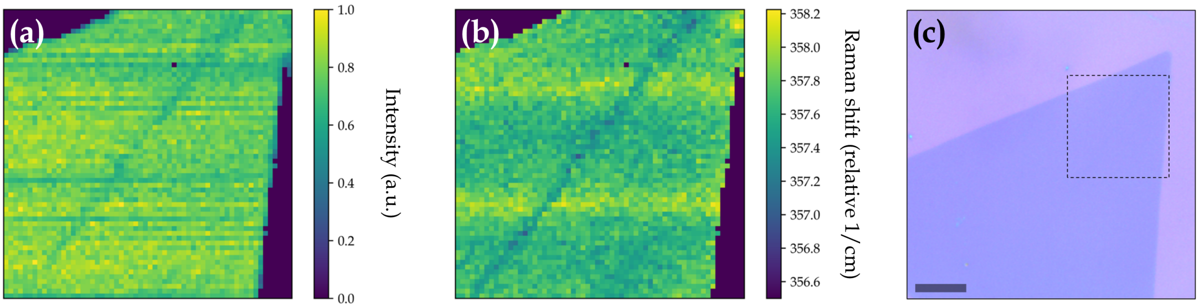

Figure 6.14: E_{2g} mode **(a)** intensity and **(b)** energy maps with 457 nm excitation beam of 2.0% at V–WS_2 sample. **(c)** Optical image of the region. Scale bar is 10 µm. Map dimensions are 20 µm × 20 µm.

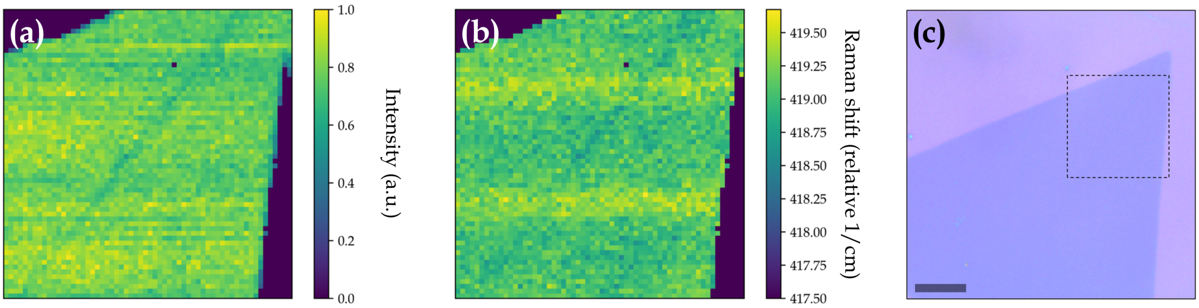

Figure 6.15: A_{1g} mode **(a)** intensity and **(b)** energy maps with 457 nm excitation beam of 2.0% at V–WS_2 sample. **(c)** Optical image of the region. Scale bar is 10 µm. Map dimensions are 20 µm × 20 µm.

Figures (6.14) and (6.15) display intensity and frequency maps for both E_{2g} and A_{1g} Raman modes of 2.0% at V–WS_2. In contrast with other measurements, it is very noticeable the changes in intensity and frequency for both Raman modes, which was not expected as discussed initially.

To understand what lies in the redshift of both Raman modes, we tried to adapt our hypothesis that a higher density of vanadium atoms in the defect lines would change exclusively in E_{2g} mode.

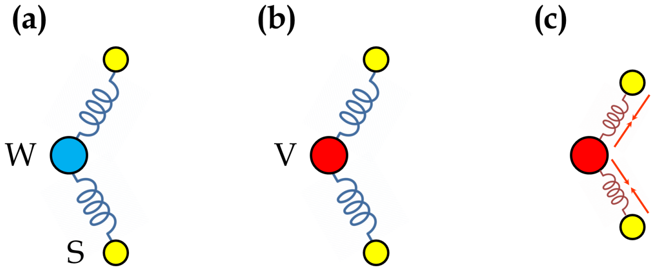

Figure 6.16: Simple representation of the changes generated by the exchange of the metal atom. **(a)** S–W–S bonding. **(b)** S–V–S bonding without bond-length contraction. **(c)** S–V–S bonding with bond-length contraction.

As well as changing the mass of the metal, we also change the length of the bond between the metal atom and the sulphur atoms, so we would also expect a strain effect in the defective line since the bond length between vanadium and sulfur atoms is much smaller than the length between tungsten and sulfur atoms as shown in Figure (6.16). This effect results in a tensile stress in the crystal, which explains the redshift of both first order Raman modes as described by Dadgar *et al.*, that report energy redshift for both modes as consequence of tensile strains in WS_2 [71].

6.3 Nonlinear optical characterization

Linear optical techniques gave us good insights into what phenomena that are concealed in the defect lines of CVD-grown WS_2 monolayers. However, these techniques take tens of hours to be acquired. The PL maps previously shown took ~5 hours each, while Raman maps took ~10 hours each. They are powerful tools for fundamental studies, but they are nearly impractical to evaluate sample quality where fast time are required.

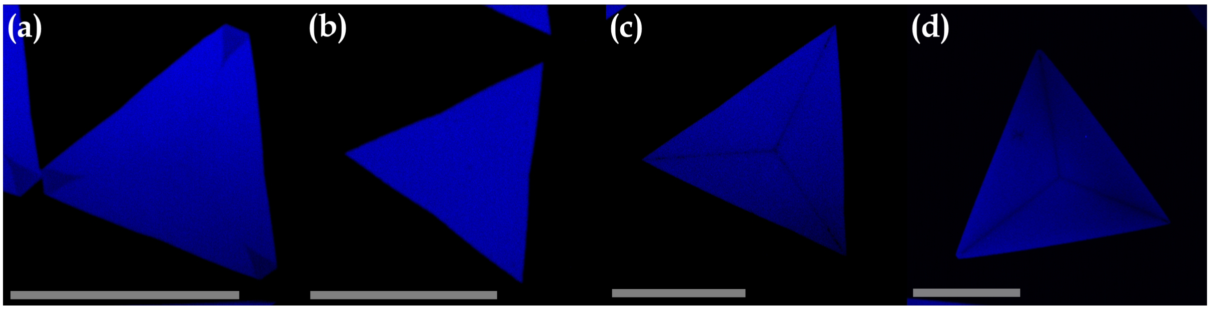

Figure 6.17: SHG images of **(a)** pristine, **(b)** 0.4, **(c)** 2.0, and **(d)** 8.0% at V–WS_2 at 405 nm. Scale bars are 50 µm.

Figure (6.17) shows SHG images that took ∼15 seconds each to be obtained. Note that the measurement areas are roughly 6 to 25 times larger if compared with Raman and PL maps shown in the previous section for each concentration of V–WS_2. As expected, the SHG image for pristine samples does not show any feature at the defect line. The same is observed for 0.4% V–WS_2. On the other hand, there is a decrease in SH signal localized at the defect lines for both 2.0 and 8.0% V–WS_2 flakes.

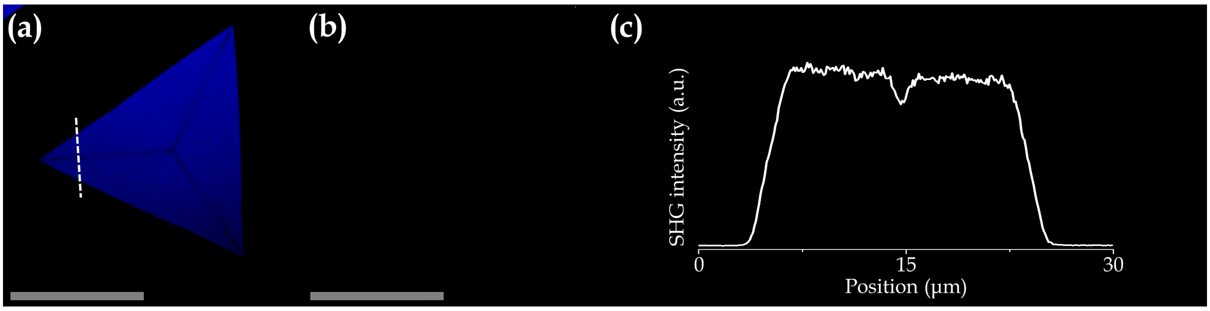

Figure 6.18: SHG images of 2.0% at V–WS_2 at **(a)** 405 and **(b)** 395 nm. Both images were acquired using the same 405/10 nm filter. **(c)** Profile of the SHG signal for 405 nm at the dashed line. Scale bars are 50 µm.

Figure (6.18) images show a 2.0% at V–WS_2 flake. Figure (6.18a) and (6.18b) show the SHG response acquired with a excitation energy of 405 nm and 395 nm, respectively. Note that in Figure (6.18c), which displays a line profile from Figure (6.18a), indicates a clear intensity decrease at the defective line. To further expand the use of nonlinear techniques to map these defects, we employed a more complex experimental setup, which allowed us to probe these samples with various energy values in order to define the optimal configuration for future characterizing procedures.

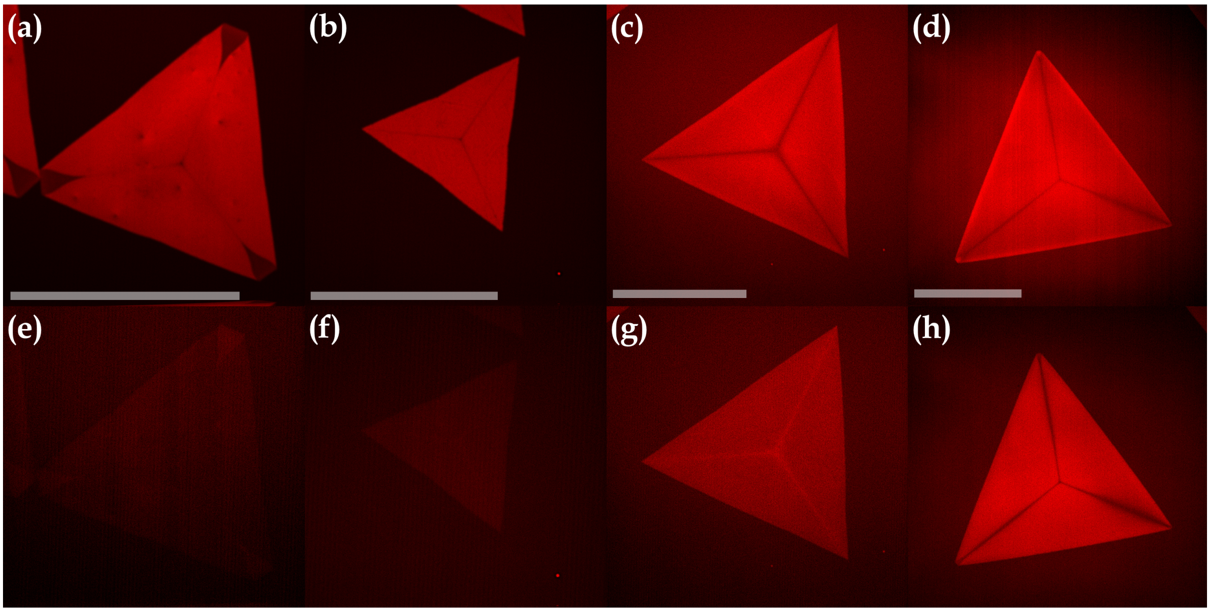

Figure 6.19: FWM images at 626 nm for **(a)** pristine, **(b)** 0.4, **(c)** 2.0, and **(d)** 8.0% at V–WS_2 and at 680 nm for **(e)** pristine, **(f)** 0.4, **(g)** 2.0, and **(h)** 8.0% at V–WS_2. The pump, FWM signals, and filters used to acquire these images follow the same order as presented in Table (5.1). Scale bars are 50 µm.

Figure (6.19) images show various FWM images for the same flakes presented in Figure (6.17). FWM signal were acquired using two lasers, for (6.19a–d) we used $\omega_1 = 788$ nm and $\omega_2 = 1064$ nm, resulting $\omega_{\text{FWM}} = 626$ nm, and for (6.19e–h) we used $\omega_1 = 830$ nm and $\omega_2 = 1064$ nm, resulting in $\omega_{\text{FWM}} = 680$ nm. At 680 nm, pristine and 0.4% at V–WS_2 present barely any FWM signal. However, the defect lines are noticable for these same V concentrations for FWM at 626 nm, which were not evident in SHG images. From this point, we proceed to perform FMW measurements with different wavelengths in order to observe some resonant behavior.

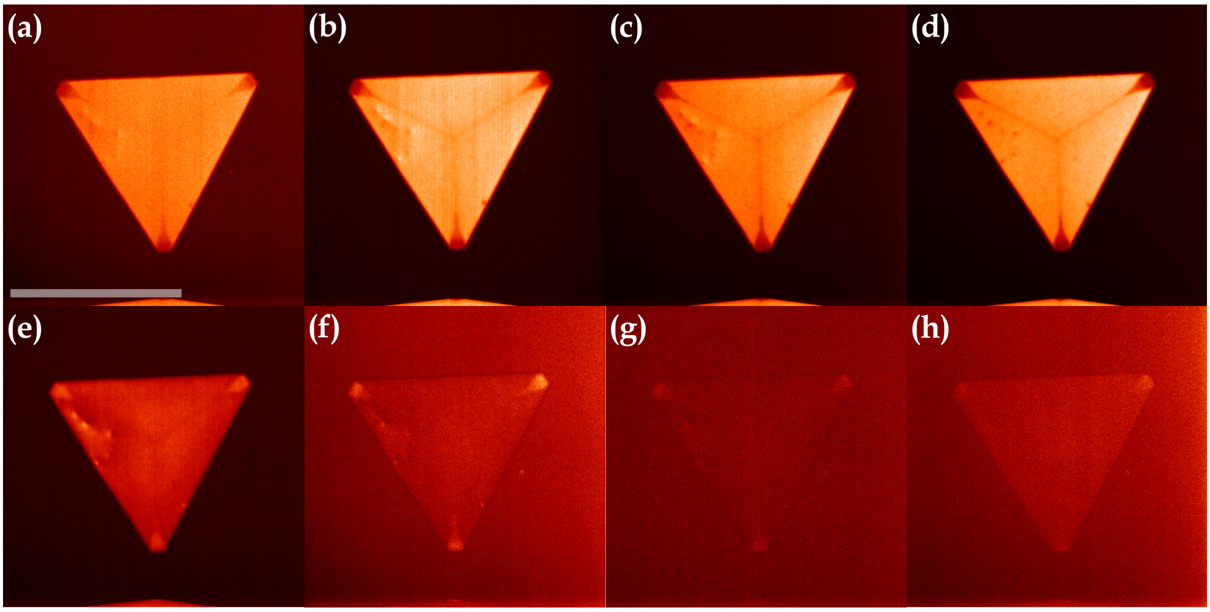

Figure 6.20: FWM images at various wavelengths of pristine WS_2. FWM signals are **(a)** 610, **(b)** 620, **(c)** 626, **(d)** 632, **(e)** 650, **(f)** 667, **(g)** 670, and **(h)** 680 nm. The pump, FWM signals, and filters used to acquire these images follow the same order as presented in Table (5.1). ∼70 mW were used for pump and 1064 nm lasers. Scale bars are 50 µm.

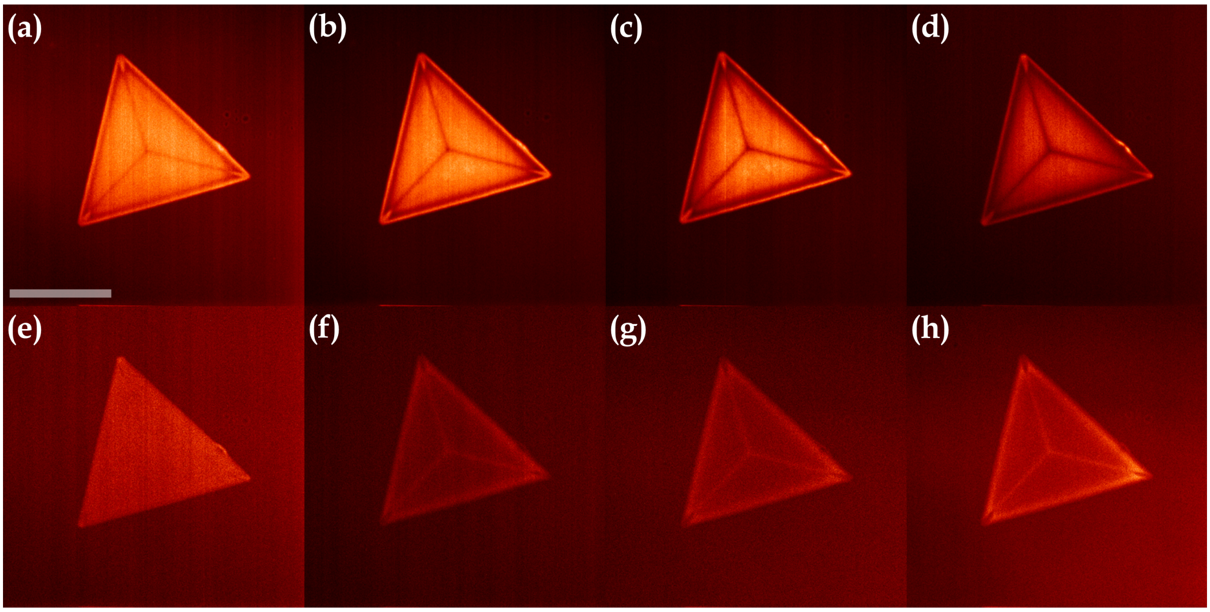

Figure 6.21: FWM images at various wavelengths of 0.4% at V–WS_2. FWM signals are **(a)** 610, **(b)** 620, **(c)** 626, **(d)** 632, **(e)** 650, **(f)** 667, **(g)** 670, and **(h)** 680 nm. The pump, FWM signals, and filters used to acquire these images follow the same order as presented in Table (5.1). ∼70 mW were used for pump and 1064 nm lasers. Scale bars are 50 µm.

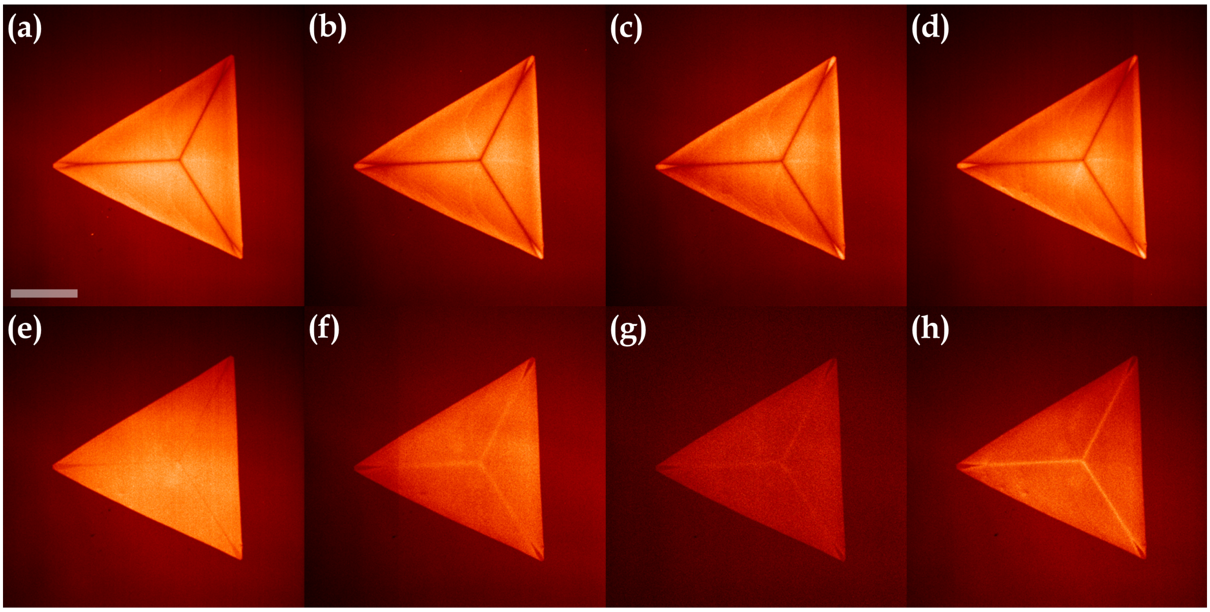

Figure 6.22: FWM images at various wavelengths of 2.0% at V–WS_2. FWM signals are **(a)** 610, **(b)** 620, **(c)** 626, **(d)** 632, **(e)** 650, **(f)** 667, **(g)** 670, and **(h)** 680 nm. The pump, FWM signals, and filters used to acquire these images follow the same order as presented in Table (5.1). ~70 mW were used for pump and 1064 nm lasers. Scale bars are 50 µm.

Figures (6.20), (6.21), and (6.22) are FWM images within the PL energy range (1.82–2.03 eV). Pristine WS_2 presents a strong signal within the 610–632 nm range, but it decreases for less energetic excitations. Doped samples, however, exhibit good contrast to the defect lines. Within the 610–632 nm range, the FWM signal of the defect line is smaller than the FWM signal of the rest of the flake. Within the 667–680 nm, the FWM signal of the defect line enhances relative to the rest of the flake.

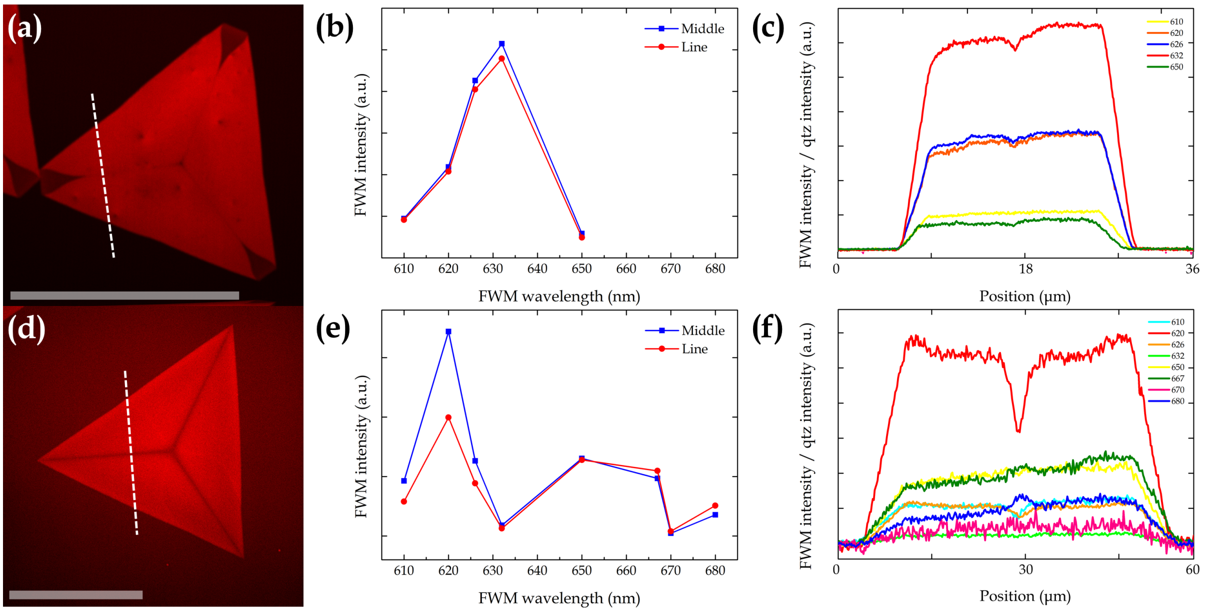

Figure 6.23: (a,d) Pristine and 2.0% at V–WS_2 flakes, respectively. **(b,e)** FWM intensity profile in function of FWM signal for pristine and 2.0% at V–WS_2, respectively. **(c,f)** FWM signal profile (dashed lines in **(a)** and **(d)**, respectively. 60 mW were used for pump and 1064 nm lasers. Scale bars are 50 µm.

Figure (6.23) shows FWM signal profiles for pristine (top) and 2.0% at V–WS_2 (bottom). Figure (6.23a,d) show the profile line used, whilst Figure (6.23b,e) compares the intensities of the FWM signal in the line and out of the line. The FWM signal is normalized by the quartz crystal FWM signal at the same wavelengths and incident power [61]. Figure (6.23c,f) display the profile of the dashed line in **(a)** and **(d)**, respectively. Figure (6.23b) does not show FWM intensity points for 667 nm or above because the FWM signal are negligible.

Figure (6.23), in combination with PL measurements, allows us to compare linear and nonlinear techniques. PL spectra show two excitonic energies for V-doped WS_2 samples. Pristine samples are resonant with 632 nm emission energy, while 2.0% V-doped samples present resonant behavior within two energy ranges. Figure (6.22) shows that the defect lines are resonant with 680 nm wavelength. This information matches with Figure (6.3) in which we see a low-energy excitonic energy formation in agreement with vanadium introduction.

Resonant FWM images along with FWM profiles show that this technique is useful to localize substitutional defects under proper initial investigation using other techniques such as PL and Raman spectroscopy. In contrast with linear methods, SHG and FWM proved to be much more reliable for large-scale investigation tools, to evaluate sample qualities for industrial and technological uses.

6.4 Scanning Probe Microscopy measurements

In the final stages of this work, a series of experiments were performed in sequence. To obtain accurate quantitative information from SPM measurements, the samples must be electricaly discharged. We were concerned about this procedure of tearing the samples apart. Therefore, we proceed to perform SPM experiments without discharging, which may cause artifacts to appear in the data. However, we are using SPM as qualitative information to support our previous claims.

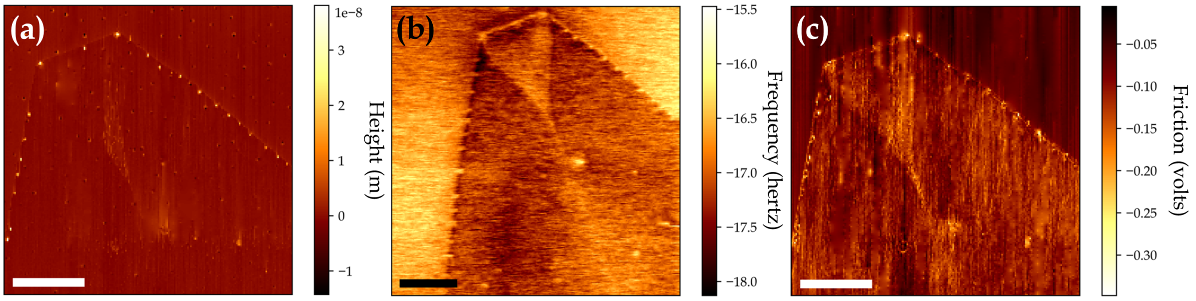

Figure 6.24: **(a)** AFM, **(b)** EFM, and **(c)** LFM measurements of pristine WS_2. Scale bars are 5 µm.

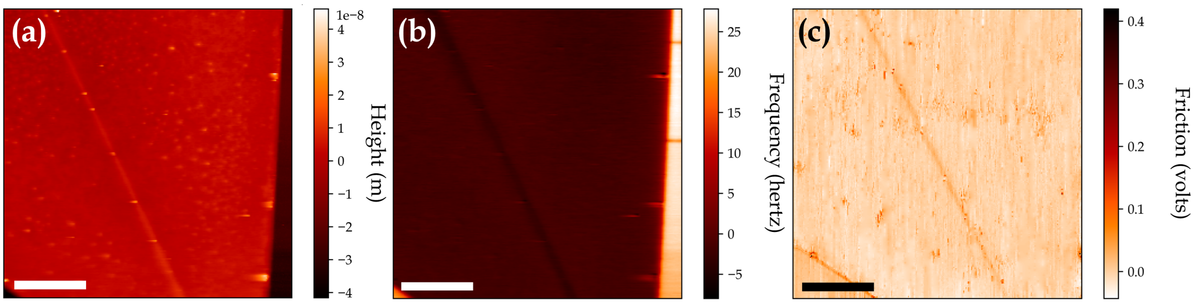

Figure 6.25: **(a)** AFM, **(b)** EFM, and **(c)** LFM measurements of 2.0% at V–WS_2. Scale bars are 5 µm.

Figure (6.25a) shows an AFM image for 2.0% at V–WS_2 sample shows an evident higher topography line at the defective region, while the the pristine sample has roughly constant topography as shown in Figure (6.24a). As discussed, accumulated charge causes a topography artifact, resulting in the line in AFM of Figure (6.25a) with tens of nanometers. AFM measurements were performed on Tapping Mode.

Figure (6.25b) shows an EFM image for 2.0% at V–WS_2 presents a dark line in our region of interest, which is indicative of a region with a higher dielectric constant (*i.e.,* closer to a metal) than its surroundings. The same is not observed for the pristine sample in Figure (6.24b). Our hypothesis was based that the intentional introduction of V-dopants not only has non-homogeneous doping effects but causes V atoms to replace W atoms with more frequency at the bisection lines at triangular flakes. EFM shows a more metallic material in these lines, which fits with the formation of a new material at these regions, VS_2, a metallic TMD.

Figure (6.25c) shows a LFM image for 2.0% at V–WS_2 clearly shows that the central line has greater friction with the probe than the rest of the flake (darker region in the image), indicating that it has a different chemical composition. In the case of the pristine sample, Figure (6.24a) shows that there is no such central line with a different composition.

6.5 Exploring more defects

Besides well-behaved V–WS_2 triangular samples, other types of defect were observed in various flakes. We selected a few to present.

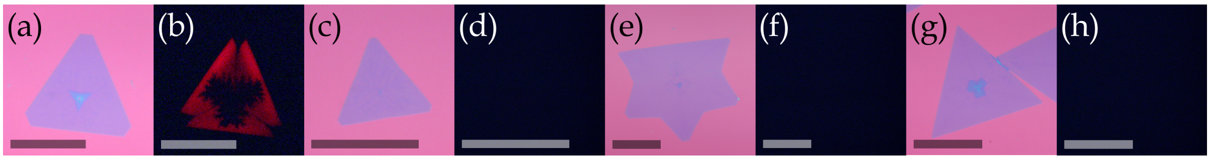

Figure 6.26: Optical and fluorescent images of various defective vanadium-doped WS_2 flakes. Scale bars are 50 µm.

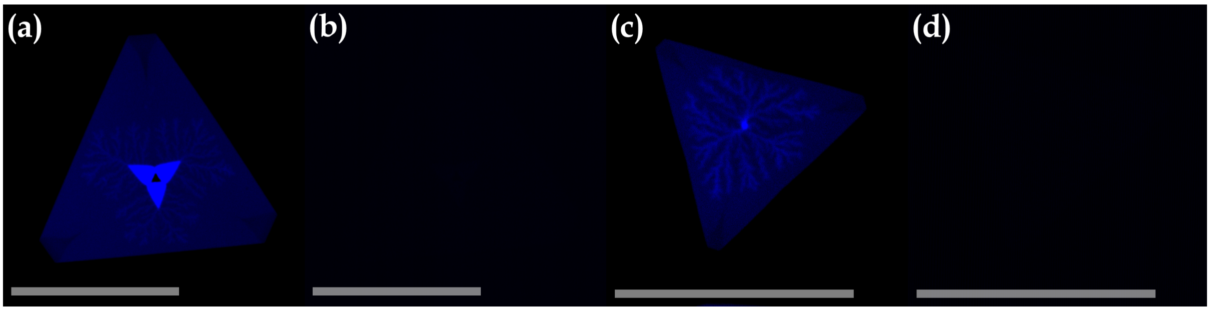

Figure 6.27: SHG images of **(a,b)** pristine and **(c,d)** 0.4% at V–WS_2. **(a)** and **(c)** is a SHG signal at 405 nm excitation beam using a 405/10 nm band-pass filter. **(b)** and **(d)** are signals at 790 nm excitation beam with the same filter. Scale bars are 50 µm.

Figure (6.26a,b) shows pristine WS_2 optical and fluorescence images, respectively. FI depicts three dark regions: the bisection lines, the tip of the flakes, and a large "irregular" region close to the nucleation point (center). The SHG signal for the same flake is shown in Figure (6.27a). W-vacancy regions are favorable spots for dopants. Figure (6.28) shows resonant FWM for the same flake. Similarly to doped samples, FWM shows a resonant region, but this time at these irregular large regions. The shape of the flake resembles the growth of hexagonal WS_2 flakes induced by a high H_2 flow. Hexagonal WS_2 flakes present two regions: α-domain and β-domain, which have higher chances to show W vacancies [72]. The growth of β-domains may also be the result of the precursors used in the growth of the samples, which may result in formation of these irregular defective regions [39, 72].

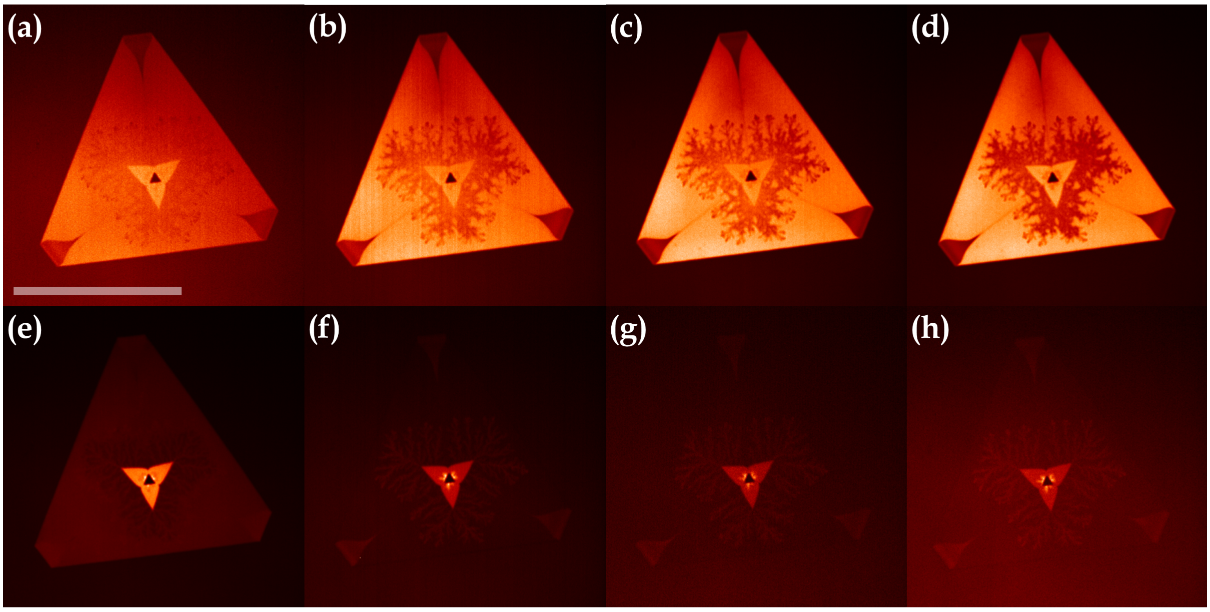

Figure 6.28: FWM images at various wavelengths of pristine WS_2.FWM signals are **(a)** 610, **(b)** 620, **(c)** 626, **(d)** 632, **(e)** 650, **(f)** 667, **(g)** 670, and **(h)** 680 nm. The pump, FWM signals, and filters used to acquire these images follow the same order as presented in Table (5.1). Scale bars are 50 µm.

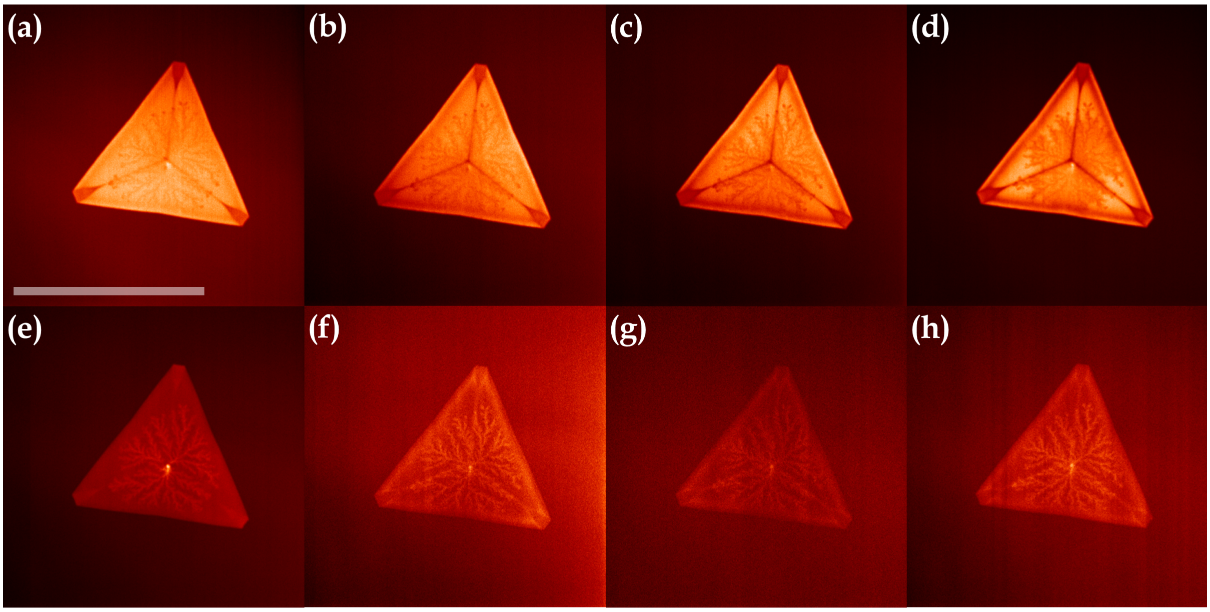

Figure 6.29: FWM images at various wavelengths of 0.4% at V–WS_2. FWM signals are **(a)** 610, **(b)** 620, **(c)** 626, **(d)** 632, **(e)** 650, **(f)** 667, **(g)** 670, and **(h)** 680 nm. The pump, FWM signals, and filters used to acquire these images follow the same order as presented in Table (5.1). Scale bars are 50 µm.

Figure (6.29) shows resonant FWM for 0.4% at V–WS_2. **(a-d)** depicts the same

1D defect region at bisection lines, but also presents dark regions similarly shown in Figure (6.28). FWM at 680 nm makes clear that the defect accumulation is not only in the bisection lines, but also are very present in these irregular regions.

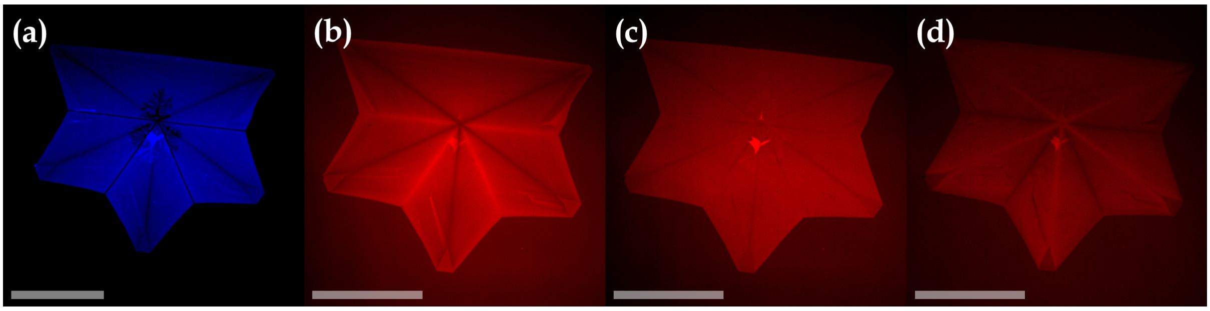

Figure 6.30: **(a)** SHG at 405 nm and **(b-d)** FWM images of 2% at V–WS_2. The FWM signals are **(b)** 610 nm, **(c)** 650 nm, and **(d)** 680 nm, in which we use a specific filter for each beam as reported in Table (5.1). Scale bars are 50 μm.

Figure (6.30) presents nonlinear images of 2.0% at V–WS_2. Figure (6.30a) is a SHG image of the flake, which show us two types of dark lines with different widths, evident by sharpness. The less sharp lines are compatible with dopant-accumulation defect line linked to V-deposition regions. However, sharp dark lines may be related with grain boundaries due to more than one nucleation point [73]. FWM images at 610 nm show V-related lines as dark lines and bright lines at 680 nm, as discussed previously, in contrast with ground boundaries defect lines, that are bright at 610 nm and dark at 680 nm.

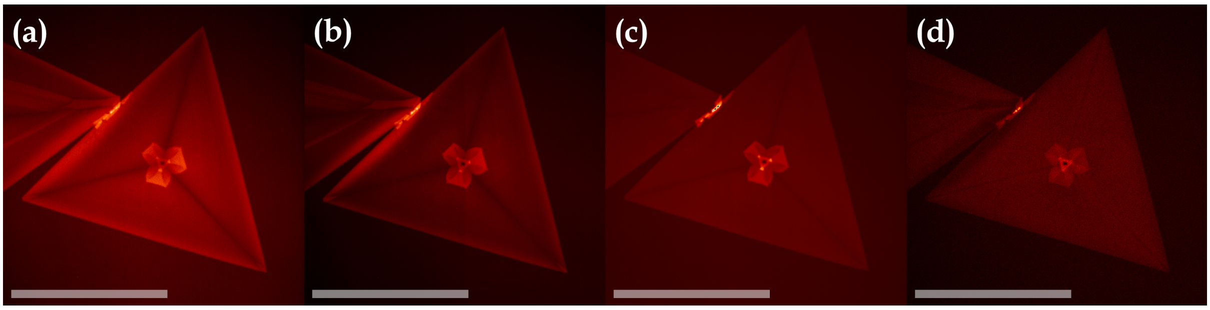

Figure 6.31: FWM images at **(a)** 610, **(b)** 626, **(c)** 650, and **(d)** 680 nm, in which we use a specific filter for each beam as reported in Table (5.1). Scale bars are 50 μm.

Figure (6.31) shows FWM images of another 2.0% at V–WS_2 flake. In this case, we see a regular triangle-shaped flake, but we do not see the resonance response of the FWM signal in the V-regions at 680 nm. Nevertheless, it is noticeable a bilayer or higher stacking formation close to the triangle barycenter. This region presents a shape similar to hexagonal WS_2 flakes, but it is resonant with energies closer to 650 nm rather than 680 nm as was previously observed.

Chapter 7

Conclusion and further prospects

We demonstrated that CVD-grown WS_2 flakes present a non-homogenous growth, and also a non-homogenous optical response. A defective region is noticeable for pristine samples in Fluorescent Images. Vibrational information indicates a higher density of dopant in reason of the redshift of the Raman modes of WS_2 for heavily-doped samples, thus resulting in redshifts in the energy of both E_{2g} and A_{1g} modes, which were not evident for pure and lightly-doped samples.

Photoluminescence results show the formation of an excitonic energy level for doped samples of energy 1.8–1.9 eV, which behaves sublinearly with respect to the incident power. Besides, photoluminescence spectra of the defective region exhibit an absolute quenching of the PL peak related to the WS_2 A exciton for heavly-doped WS_2. Spatially-resolved hyperspectral photoluminescence measurements also show a blueshift in the energy of the WS_2 exciton energy for doped samples.

Nonlinear optical techniques have been demonstrated as powerful tools for large-area analysis, once these techniques take a few seconds to be performed. Also, we successfully employed nonlinear optics for the identification of defects in doped semiconducting TMD samples via resonant FWM measurements. Our results are a starting point for future large-scale applications of nonlinear optical techniques to trace defects in 2D materials (or materials in general).

Complementing linear and nonlinear optical techniques, Scanning Probe Microscopy techniques also provided significant results for our studied samples. These measurements indicate a structural/chemical difference in the defect line for heavily-doped samples, which exhibited a formation of a material with higher dielectric constant in these defect regions as a result of substitutional defects, thus supporting our predictions.

In conclusion, we performed several techniques in pure and intentionally doped WS_2 samples with vanadium to build spatial profiles, trying to understand how defects are intentionally introduced via CVD synthesis. Our results point out that doping-related defects accumulate non-homogeneity, but with higher density at the bisection lines of the triangular-shaped flakes. Regarding CVD-grown, we state that improvements should be made to the CVD growth processes for thin materials in order to reduce or even eliminate the effects caused by the formation of the defect line, with the objective of the growth and use of these materials on a large scale in the near future.

The next step for developing this work is to explore in more detail the linear optical results to better understand the relation between the strain caused by the introduction of the dopant and the shifts observed in both Raman modes as well as the PL energies shifts. Other possible next step is the employment of Tip Enhanced techniques, Raman (TERS) and PL (TEPL), which is a space-resolved advanced Raman technique. In general, conventional Raman provides a spatial resolution of about 300 nm under optimal conditions. On the other hand, the tip-enhanced techniques' spatial resolution depends on the diameter of the tip used. Using proper tips, it may be possible to investigate further to know what exactly lies in these defect lines. This technique is available in our laboratory at UFMG, but our set-up requires a transparent substrate to be performed.

Bibliography

[1] Philip Richard Wallace. The band theory of graphite. *Physical review*, 71(9):622, 1947.

[2] RE Peierls. Bemerkungen über umwandlungstemperaturen. *Helv. Phys. Acta*, 7(2):81, 1934.

[3] Barry Boehm. A spiral model of software development and enhancement. *ACM SIGSOFT Software engineering notes*, 11(4):14–24, 1986.

[4] Edward P Randviir, Dale AC Brownson, and Craig E Banks. A decade of graphene research: production, applications and outlook. *Materials Today*, 17(9):426–432, 2014.

[5] Sergio Navalón, Wee-Jun Ong, and Xiaoguang Duan. Sustainable catalytic processes driven by graphene-based materials. *Processes*, 8(6):672, 2020.

[6] Leonid A Falkovsky. Optical properties of graphene. In *Journal of Physics: conference series*, volume 129, page 012004. IOP Publishing, 2008.

[7] AH Castro Neto, Francisco Guinea, Nuno MR Peres, Kostya S Novoselov, and Andre K Geim. The electronic properties of graphene. *Reviews of modern physics*, 81(1):109, 2009.

[8] Wonbong Choi, Nitin Choudhary, Gang Hee Han, Juhong Park, Deji Akinwande, and Young Hee Lee. Recent development of two-dimensional transition metal dichalcogenides and their applications. *Materials Today*, 20(3):116–130, 2017.

[9] Bárbara LT Rosa, Kazunori Fujisawa, Joyce CC Santos, Tianyi Zhang, Matheus JS Matos, Frederico B Sousa, Tiago C Barbosa, Lucas Lafeta, Sérgio LLM Ramos, Bruno R Carvalho, et al. Investigation of spatially localized defects in synthetic WS_2 monolayers. *Physical Review B*, 106(11):115301, 2022.

[10] Fu Zhang, Boyang Zheng, Amritanand Sebastian, David H Olson, Mingzu Liu, Kazunori Fujisawa, Yen Thi Hai Pham, Valery Ortiz Jimenez, Vijaysankar Kalappattil, Leixin Miao, et al. Monolayer vanadium-doped tungsten disulfide: a room-

temperature dilute magnetic semiconductor. *Advanced Science*, 7(24):2001174, 2020.

[11] Pulickel Ajayan, Philip Kim, and Kaustav Banerjee. van der waals materials. *Phys. Today*, 69(9):38, 2016.

[12] Jose A Carrasco, Pau Congost-Escoin, Mhamed Assebban, and Gonzalo Abellán. Antimonene: a tuneable post-graphene material for advanced applications in optoelectronics, catalysis, energy and biomedicine. *Chemical Society Reviews*, 2023.

[13] Jean-Noel Fuchs and Mark Oliver Goerbig. Introduction to the physical properties of graphene. *Lecture notes*, 10:11–12, 2008.

[14] Kostya S Novoselov, D Jiang, F Schedin, TJ Booth, VV Khotkevich, SV Morozov, and Andre K Geim. Two-dimensional atomic crystals. *Proceedings of the National Academy of Sciences*, 102(30):10451–10453, 2005.

[15] Manish Chhowalla, Hyeon Suk Shin, Goki Eda, Lain-Jong Li, Kian Ping Loh, and Hua Zhang. The chemistry of two-dimensional layered transition metal dichalcogenide nanosheets. *Nature chemistry*, 5(4):263–275, 2013.

[16] Bairen Zhu, Ke Xiao, Siyuan Yang, Kenji Watanabe, Takashi Taniguchi, and Xiaodong Cui. In-plane electric field induced orbital hybridization of excitonic states in monolayer WSe_2. *Phys. Rev. Lett. 131, 036901*, 2023.

[17] Damien Voiry, Aditya Mohite, and Manish Chhowalla. Phase engineering of transition metal dichalcogenides. *Chemical Society Reviews*, 44(9):2702–2712, 2015.

[18] Jenaina Ribeiro-Soares, RM Almeida, Eduardo B Barros, Paulo T Araujo, Mildred S Dresselhaus, Luiz G Cançado, and Ado Jorio. Group theory analysis of phonons in two-dimensional transition metal dichalcogenides. *Physical Review B*, 90(11):115438, 2014.

[19] Ryan Beams, Luiz Gustavo Cançado, Sergiy Krylyuk, Irina Kalish, Berç Kalanyan, Arunima K Singh, Kamal Choudhary, Alina Bruma, Patrick M Vora, Francesca Tavazza, et al. Characterization of few-layer 1t′ $MoTe_2$ by polarization-resolved second harmonic generation and raman scattering. *ACS nano*, 10(10):9626–9636, 2016.

[20] Huaihong Guo, Teng Yang, Mahito Yamamoto, Lin Zhou, Ryo Ishikawa, Keiji Ueno, Kazuhito Tsukagoshi, Zhidong Zhang, Mildred S Dresselhaus, and Riichiro Saito. Double resonance raman modes in monolayer and few-layer $MoTe_2$. *Physical Review B*, 91(20):205415, 2015.

[21] Magdalena Grzeszczyk, Katarzyna Gołasa, M Zinkiewicz, K Nogajewski, Maciej Roman Molas, Marek Potemski, Andrzej Wysmołek, and Adam Babiński. Raman scattering of few-layers $MoTe_2$. *2D Materials*, 3(2):025010, 2016.

[22] Ziqun Niu, Tianli Feng, Tao Li, Kejian Yang, Jia Zhao, Guiqiu Li, Dechun Li, Shengzhi Zhao, Wenchao Qiao, Hongwei Chu, et al. Layered metallic vanadium disulfide for doubly q-switched tm: Yap laser with eom: Experimental and theoretical investigations. *Nanomaterials*, 11(10):2605, 2021.

[23] Mongur Hossain, Juanxia Wu, Wen Wen, Haining Liu, Xinsheng Wang, and Liming Xie. Chemical vapor deposition of 2d vanadium disulfide and diselenide and raman characterization of the phase transitions. *Advanced Materials Interfaces*, 5(16):1800528, 2018.

[24] Kin Fai Mak, Changgu Lee, James Hone, Jie Shan, and Tony F Heinz. Atomically thinMoS_2: a new direct-gap semiconductor. *Physical review letters*, 105(13):136805, 2010.

[25] Humberto R Gutiérrez, Nestor Perea-López, Ana Laura Elías, Ayse Berkdemir, Bei Wang, Ruitao Lv, Florentino López-Urías, Vincent H Crespi, Humberto Terrones, and Mauricio Terrones. Extraordinary room-temperature photoluminescence in triangular WS_2 monolayers. *Nano letters*, 13(8):3447–3454, 2013.

[26] Alexey Chernikov, Timothy C Berkelbach, Heather M Hill, Albert Rigosi, Yilei Li, Burak Aslan, David R Reichman, Mark S Hybertsen, and Tony F Heinz. Exciton binding energy and nonhydrogenic rydberg series in monolayer WS_2. *Physical review letters*, 113(7):076802, 2014.

[27] Humberto Terrones, Florentino López-Urías, and Mauricio Terrones. Novel hetero-layered materials with tunable direct band gaps by sandwiching different metal disulfides and diselenides. *Scientific reports*, 3(1):1549, 2013.

[28] Steven H Simon. *The Oxford solid state basics*. OUP Oxford, 2013.

[29] Leyi Loh, Zhepeng Zhang, Michel Bosman, and Goki Eda. Substitutional doping in 2d transition metal dichalcogenides. *Nano Research*, 14(6):1668–1681, 2021.

[30] Rehan Younas, Guanyu Zhou, and Christopher L Hinkle. A perspective on the doping of transition metal dichalcogenides for ultra-scaled transistors: Challenges and opportunities. *Applied Physics Letters*, 122(16), 2023.

[31] Yasir Beeran Pottathara, Sabu Thomas, Nandakumar Kalarikkal, Yves Grohens, and Vanja Kokol. *Nanomaterials Synthesis: Design, Fabrication and Applications*. Elsevier, 2019.

[32] HW Zhu, CL Xu, DH Wu, BQ Wei, R Vajtai, and PM Ajayan. Direct synthesis of long single-walled carbon nanotube strands. *Science*, 296(5569):884–886, 2002.

[33] Xuesong Li, Weiwei Cai, Jinho An, Seyoung Kim, Junghyo Nah, Dongxing Yang, Richard Piner, Aruna Velamakanni, Inhwa Jung, Emanuel Tutuc, et al. Large-area synthesis of high-quality and uniform graphene films on copper foils. *science*, 324(5932):1312–1314, 2009.

[34] Dmitri Golberg, Yoshio Bando, CC Tang, and CY Zhi. Boron nitride nanotubes. *Advanced Materials*, 19(18):2413–2432, 2007.

[35] Li Song, Lijie Ci, Hao Lu, Pavel B Sorokin, Chuanhong Jin, Jie Ni, Alexander G Kvashnin, Dmitry G Kvashnin, Jun Lou, Boris I Yakobson, et al. Large scale growth and characterization of atomic hexagonal boron nitride layers. *Nano letters*, 10(8):3209–3215, 2010.

[36] Shaswat Barua, Xiangshuai Geng, and Biqiong Chen. Graphene-based nanomaterials for healthcare applications. In *Photonanotechnology for Therapeutics and Imaging*, pages 45–81. Elsevier, 2020.

[37] Avijit Kumar, Kaustuv Banerjee, and Peter Liljeroth. Molecular assembly on two-dimensional materials. *Nanotechnology*, 28(8):082001, 2017.

[38] Jin-Ho Lee, Soo-Jeong Park, and Jeong-Woo Choi. Electrical property of graphene and its application to electrochemical biosensing. *Nanomaterials*, 9(2):297, 2019.

[39] Zhuhua Xu, Yanfei Lv, Jingzhou Li, Feng Huang, Pengbo Nie, Siwei Zhang, Shichao Zhao, Shixi Zhao, and Guodan Wei. Cvd controlled growth of large-scale WS_2 monolayers. *RSC advances*, 9(51):29628–29635, 2019.

[40] Nitin Babu Shinde, Beo Deul Ryu, Chang-Hee Hong, Bellarmine Francis, S Chandramohan, and Senthil Kumar Eswaran. Growth behavior, nucleation control and excellent optical properties of atomically thin WS_2 thin films processed via gas-phase chemical vapor deposition. *Applied Surface Science*, 568:150908, 2021.

[41] Chao Li, Tomoya Kameyama, Tomoyuki Takahashi, Toshiro Kaneko, and Toshiaki Kato. Nucleation dynamics of single crystal WS_2 from droplet precursors uncovered by in-situ monitoring. *Scientific reports*, 9(1):12958, 2019.

[42] Gwang Hwi An, Seok Joon Yun, Young Hee Lee, and Hyun Seok Lee. Growth mechanism of alternating defect domains in hexagonal WS_2 via inhomogeneous w-precursor accumulation. *Small*, 16(43):2003326, 2020.

[43] Bruno Schuler, Jun-Ho Lee, Christoph Kastl, Katherine A Cochrane, Christopher T Chen, Sivan Refaely-Abramson, Shengjun Yuan, Edo van Veen, Rafael Roldán, Nicholas J Borys, et al. How substitutional point defects in two-dimensional WS_2 induce charge localization, spin–orbit splitting, and strain. *ACS nano*, 13(9):10520–10534, 2019.

[44] Shisheng Li, Jinhua Hong, Bo Gao, Yung-Chang Lin, Hong En Lim, Xueyi Lu, Jing Wu, Song Liu, Yoshitaka Tateyama, Yoshiki Sakuma, et al. Tunable doping of rhenium and vanadium into transition metal dichalcogenides for two-dimensional electronics. *Advanced Science*, 8(11):2004438, 2021.

[45] Chandrasekhara Venkata Raman. The colour of the sea. *Nature*, 108(2716):367–367, 1921.

[46] John David Jackson. Classical electrodynamics, 1999.

[47] YU Peter and Manuel Cardona. *Fundamentals of semiconductors: physics and materials properties*. Springer Science & Business Media, 2010.

[48] Neil W Ashcroft, N David Mermin, et al. Solid state physics, 1976.

[49] Luiz Gustavo de Oliveira Lopes Cançado. Raman spectroscopy of nanographites. 2006.

[50] Luiz Gustavo Pimenta Martins. High-pressure raman study of graphene: a spectroscopic evidence for the diamondol. 2015.

[51] Rafael N Gontijo, Geovani C Resende, Cristiano Fantini, and Bruno R Carvalho. Double resonance raman scattering process in 2d materials. *Journal of Materials Research*, 34(12):1976–1992, 2019.

[52] Bruno R Carvalho, Yuanxi Wang, Sandro Mignuzzi, Debdulal Roy, Mauricio Terrones, Cristiano Fantini, Vincent H Crespi, Leandro M Malard, and Marcos A Pimenta. Intervalley scattering by acoustic phonons in two-dimensional MoS_2 revealed by double-resonance raman spectroscopy. *Nature communications*, 8(1):1–8, 2017.

[53] Qiang Li, Jun Lu, Prince Gupta, and Min Qiu. Engineering optical absorption in graphene and other 2d materials: advances and applications. *Advanced Optical Materials*, 7(20):1900595, 2019.

[54] Kin Fai Mak and Jie Shan. Photonics and optoelectronics of 2d semiconductor transition metal dichalcogenides. *Nature Photonics*, 10(4):216–226, 2016.

[55] Ziliang Ye, Ting Cao, Kevin O'brien, Hanyu Zhu, Xiaobo Yin, Yuan Wang, Steven G Louie, and Xiang Zhang. Probing excitonic dark states in single-layer tungsten disulphide. *Nature*, 513(7517):214–218, 2014.

[56] Mikhail M Glazov, Eougenious L Ivchenko, Gang Wang, Thierry Amand, Xavier Marie, Bernhard Urbaszek, and BL Liu. Spin and valley dynamics of excitons in transition metal dichalcogenide monolayers. *physica status solidi (b)*, 252(11):2349–2362, 2015.

[57] Robert W Boyd. Order-of-magnitude estimates of the nonlinear optical susceptibility. *journal of modern optics*, 46(3):367–378, 1999.

[58] Nicolaas Bloembergen. Nonlinear optics: past, present, and future. *IEEE Journal of Selected Topics in Quantum Electronics*, 6(6):876–880, 2000.

[59] TH Maiman. Stimulated emission of radiation in ruby. *Nature*, 187:493–494, 1960.

[60] Ji-Xin Cheng and X Sunney Xie. Coherent anti-stokes raman scattering microscopy: instrumentation, theory, and applications, 2004.

[61] Lucas Lafeta, Aurea Corradi, Tianyi Zhang, Ethan Kahn, Ismail Bilgin, Bruno R Carvalho, Swastik Kar, Mauricio Terrones, and Leandro M Malard. Second-and third-order optical susceptibilities across excitons states in 2d monolayer transition metal dichalcogenides. *2D Materials*, 8(3):035010, 2021.

[62] Renan Cunha, Lucas Lafeta, Emerson A Fonseca, Alexandre Barbosa, Marco A Romano-Silva, Rafael Vieira, Ado Jorio, and Leandro M Malard. Nonlinear and vibrational microscopy for label-free characterization of amyloid-β plaques in alzheimer's disease model. *Analyst*, 146(9):2945–2954, 2021.

[63] KD Singer, Y Wu, and Case Western. Second harmonic generation (SHG) as a characterization technique and phenomenological probe for organic materials. *Handbook of Organic Materials for Optical and (Opto) electronic Devices—Properties and Applications*, pages 442–469, 2013.

[64] Victor L Mironov. *Fundamentalsof Scanning Probe Microscopy*. Russian academy of sciences institute for physics of microstructures, 2004.

[65] Ana Paula Moreira Barboza. Propriedades eletromecânicas de nanoestruturas por microscopia de varredura por sonda. 2012.

[66] Othmar Marti. Afm instrumentation and tips. *Handbook of micro/nanotribology*, pages 81–144, 1999.

[67] LN Kantorovich, AI Livshits, and M Stoneham. Electrostatic energy calculation for the interpretation of scanning probe microscopy experiments. *Journal of Physics: Condensed Matter*, 12(6):795, 2000.

[68] J Colchero, H Bielefeldt, A Ruf, M Hipp, O Marti, and J Mlynek. Scanning force and friction microscopy. *physica status solidi (a)*, 131(1):73–75, 1992.

[69] TLKZ Schmidt, K Lischka, and W Zulehner. Excitation-power dependence of the near-band-edge photoluminescence of semiconductors. *Physical Review B*, 45(16):8989, 1992.

[70] Ayse Berkdemir, Humberto R Gutiérrez, Andrés R Botello-Méndez, Néstor Perea-López, Ana Laura Elías, Chen-Ing Chia, Bei Wang, Vincent H Crespi, Florentino López-Urías, Jean-Christophe Charlier, et al. Identification of individual and few layers of WS_2 using raman spectroscopy. *Scientific reports*, 3(1):1755, 2013.

[71] AM Dadgar, D Scullion, K Kang, D Esposito, EH Yang, IP Herman, MA Pimenta, E-JG Santos, and AN Pasupathy. Strain engineering and raman spectroscopy of monolayer transition metal dichalcogenides. *Chemistry of Materials*, 30(15):5148–5155, 2018.

[72] Hye Yun Jeong, Youngjo Jin, Seok Joon Yun, Jiong Zhao, Jaeyoon Baik, Dong Hoon Keum, Hyun Seok Lee, and Young Hee Lee. Heterogeneous defect domains in single-crystalline hexagonal WS_2. *Advanced Materials*, 29(15):1605043, 2017.

[73] Bruno R Carvalho, Yuanxi Wang, Kazunori Fujisawa, Tianyi Zhang, Ethan Kahn, Ismail Bilgin, Pulickel M Ajayan, Ana M De Paula, Marcos A Pimenta, Swastik Kar, et al. Nonlinear dark-field imaging of one-dimensional defects in monolayer dichalcogenides. *Nano letters*, 20(1):284–291, 2019.